People's Democratic Republic of Algeria
Ministry of Higher Education and Scientific Research
Ferhat ABBAS University - Sétif 1

Setif 1 University - Ferhat ABBAS

THESIS

Presented in the Department of Physics

Faculty of Sciences

To obtain the degree of

DOCTORATE

FIELD: Sciences of Matter   **Option: Condensed Matter**

TITLE

Structural and Magneto-Optical properties of ultrathin films of Ni_n/Rh(001) and Non Linear Optical properties of chalcone derivative 4-[(1E)-3-(4-methoxyphenyl)-3-oxoprop-1-en-1-yl]phenyl 4-methylbenzene-1-sulfonate: Theoretical Study

By

BENSEBAA Mohamed

In the presence of the jury

HADDADI Khelifa	**Prof**	**Ferhat ABBAS University Sétif 1**	**President**
BOUKELKOUL Mebarek	**prof**	**Ferhat ABBAS University Sétif 1**	**Thesis Director**
BOUHEMADOU Abdelmadjid	**prof**	**Ferhat ABBAS University Sétif 1**	**Co-Director**
BAADJI Nadjib	**Prof**	**Mohamed BOUDIAF University M'sila**	**Thesis Examinor**
BOUKABCHA Nourdine	**MCA**	**Hassiba BENBOUALI University Chlef**	**Thesis Examinor**
REFFAS Mounir	**MCA**	**Ferhat ABBAS University Sétif 1**	**Thesis Examinor**
CHERGUI Abdelhamid	**Prof**	**Ferhat ABBAS University Sétif 1**	**Guest**

2023/2024

Acknowledgment

بسم الله الرحمن الرحيم

ما سلكنا البدايات إلا بتيسيره، وما بلغنا النهايات إلا بتوفيقه. وما حققنا الغايات إلا بفضله. الحمد لله الذي بنعمته تتم الصالحات.

First and foremost, I express my deepest gratitude to Allah for granting me the strength and perseverance to reach this momentous occasion of my graduation.

I am profoundly thankful to those who have been instrumental in this journey. My esteemed supervisor, whose invaluable guidance and support have been my guiding light, has imparted lessons that not only shaped this achievement but have also left a lasting impact on my life. I am equally grateful to my dear family, whose unwavering support, love, and encouragement have served as the foundation for all my endeavors. To my beloved wife, thank you for standing by me through thick and thin, for your understanding during the challenging times, and for being my greatest cheerleader; this achievement is as much yours as it is mine. I also extend my heartfelt appreciation to my dedicated teachers, who have been more than mentors, offering advice, knowledge, and friendship that have profoundly influenced my academic journey. Finally, I am deeply thankful to my friends, who have been more like brothers, for their companionship, encouragement, and the countless moments of joy and laughter we've shared. Your collective support has been invaluable, and I am truly blessed to have you all by my side on this journey.

Abstract

In the first part we employed first-principles calculations to analyze the structural, magnetic, and magneto-optical properties of ultrathin Ni films grown by pseudomorphic epitaxy on semi-infinite crystals of Rh in the [001] crystallographic direction. We adopted a relativistic method using the DFT theorem and local spin density approximation (LSDA). We calculated the electronic structure using the Spin-Polarized Relativistic (SPR) Linear Muffin-Tin Orbitals (LMTO) with the Atomic Sphere Approximation (ASA) approach. The crystalline structure is determined using a relaxation process that led to a body-centered tetragonal (BCT) structure. Magnetic calculations indicate that the inter-plane interaction is ferromagnetic, with a higher magnetic moment. The Kubo-Greenwood linear response is used to calculate the dispersion of the optical conductivity tensor based on the frequency of incoming electromagnetic radiation. Polar magneto-optical Kerr effect spectra are provided over a photon energy range of up to 10 eV. Interband transitions describe the microscopic origins of Kerr rotations.

The second part presents a theoretical study on the chalcone derivative, 4-[(1E)-3-(4-methoxyphenyl)-3-oxoprop-1-en-1-yl]phenyl 4-methylbenzene-1-sulfonate (4MPMS). Density functional theory is employed to perform calculations on geometry optimization, vibrational spectrum, 1H and 13C NMR chemical shifts, frontier molecular orbital energies and nonlinear optical characteristics using the B3LYP level with the 6-311++G(d,p) basis set. The polarizability (α), anisotropy of polarizability ($\Delta\alpha$), first and second order hyperpolarizability (β and γ) are studied in static and frequency-dependent (532 nm) state. The results showed that the frequency dependent nonlinear optical characteristics of 4MPMS, are higher than the static ones and the title molecule might be applicable for first and second order nonlinear optical materials along with a good consistency between the experimental and theoretical structure.

Résumé

Dans la première partie, nous avons utilisé des calculs de premiers principes pour analyser les propriétés structurelles, magnétiques et magnéto-optiques des films ultraminces de Ni obtenus par épitaxie pseudomorphique sur des cristaux semi-infinis de Rh dans la direction cristallographique [001]. Nous avons adopté une méthode relativiste utilisant le théorème DFT et l'approximation locale de la densité de spin (LSDA). Nous avons calculé la structure électronique en utilisant les orbitales linéaires de Muffin-Tin (LMTO) SPR (Spin-Polarized Relativistic) avec une approche ASA (Atomic Sphere Approximation). La structure cristalline a été déterminée à l'aide d'un processus de relaxation qui a conduit à une structure tétragonale centrée (BCT). Les calculs magnétiques indiquent que l'interaction inter-plan est ferromagnétique, avec un moment magnétique plus élevé que celui du massif. La réponse linéaire de Kubo-Greenwood est utilisée pour calculer la dispersion du tenseur de conductivité optique en fonction de la fréquence du rayonnement électromagnétique entrant. Les spectres de l'effet Kerr magnéto-optique polaire sont présentés sur une bande d'énergie photonique jusqu'à 10 eV. Les transitions interbandes expliquent les origines microscopiques des caractéristiques uniques des rotations de Kerr.

La deuxième partie présente une étude théorique sur le dérivé de Chalcone, 4-[(1E) -3-(4-méthoxyphényl) -3-oxoprop-1-en-1-yl] phényle 4-méthylbenzène-1-sulfonate (4MPMS). La théorie de la fonctionnelle de la densité est utilisée pour effectuer des calculs sur l'optimisation de la géométrie, le spectre vibratoire, les shifts chimiques des RMN 1H et 13C, les énergies des orbitales moléculaires frontières et les propriétés optiques non linéaires en utilisant le niveau B3LYP avec l'ensemble de base 6-311++G(d,p). La polarisabilité (α), l'anisotropie de la polarisabilité ($\Delta\alpha$), l'hyperpolarisabilité de premier et de second ordre (β et γ) ont été étudiées en état statique et en fonction de la fréquence (532 nm). Les résultats ont montré que les caractéristiques optiques non linéaires dépendant de la fréquence du 4MPMS sont plus élevées que les caractéristiques statiques et que la molécule pourrait être applicable aux matériaux optiques non linéaires du premier et du second ordre, avec une bonne similarité entre la structure expérimentale et la structure théorique.

ملخص

في الجزء الأول، قمنا باستخدام حسابات المبادئ الأولى لتحليل الخصائص البنيوية والمغناطيسية والمغناطيس ضوئية لألفالم الجد رقيقة المكونة من النيكل الموضوع فوق الروديوم في الاتجاه البلوري 001 لقد تم تبني مقاربة نسبية استعملت فيها نظرية DFT مع LSDA تم تحديد الهيكل البلوري باستخدام عملية استرخاء أدت إلى هيكل بلوري متمركز (BCT) تشير الحسابات المغناطيسية إلى أن التفاعل بين الطبقات هو مغناطيسي، مع قيمة مغناطيسية أعلى. تم استخدام الاستجابة الخطية لكوبو-غرينوود لحساب تشتت جسم الإمكانية البصرية استنادًا إلى تردد الإشعاع الكهرومغناطيسي الوارد. تم حساب طيف كير البصرية المغناطيسية القطبية على مدى طاقة الفوتون حتى 10 إلكترون فولت. تصف الانتقالات بين الفترات الفرقية الأصول الدقيقة للخصائص الفريدة لدورات كير.

الجزء الثاني يقدم دراسة نظرية حول مشتق الشالكون 4-[(1E) -3-(4-méthoxyphényl) -3-oxoprop-1-en-1-yl] , phényle 4-méthylbenzène-1-sulfonate (4MPMS) تم استخدام نظرية DFT لإجراء حسابات على تحسين الهندسة، والطيف الاهتزازي، وتحريك النواة الكيميائية للبروتونات والكربون (1H) و13C NMR، وطاقات المدار الجزيئي الأمامي، والخصائص البصرية غير الخطية باستخدام مستوى B3LYP مع مجموعة القاعدة 311-6 G(d,p) ++. تمت دراسة الاستجابية (α)، تغير استجابية(Δα) ، استجابية فائقة البصرية الأولى والثاني β و γ في الحالة الثابتة وتحت التردد (532 نانومتر). أظهرت النتائج أن خصائص البصرية غير الخطية التي تعتمد على التردد لـ MPMS4، أعلى من تلك الثابتة وأن الجزيء المدروس يمكن أن يكون من المواد التي تستعمل في التطيقات بصرية غير خطية من الدرجة الأولى والثانية كما أن البنية البلورية النظريية و المصنعة مخبريا متطابقان

Contents

General Introduction

Light and magnetism are two astonishing phenomena that have evolved significantly throughout history transitioning from a philosophical topic to a sophisticated scientific field with significant technical and theoretical impacts. Ancient civilizations, such as the Greeks and Chinese, studied natural magnets (lodestones) and questioned the secrets of light. However, the systematic investigation did not begin until the middle of the 15th century, when William Gilbert classified elements into magnetic and nonmagnetic materials, providing the framework for current magnetic theory. Meanwhile, Islamic scholars set the ground and cleared the path for the study of light. In the 19th century, Hans Christian Ørsted's discovery of electromagnetism along with Michael Faraday's research on magnetic fields and electricity showed a strong relationship between these two phenomena. James Clerk Maxwell's revolutionary equations established a unified framework for comprehending electricity, magnetism, and electromagnetic waves, anticipating the emergence of light as an electromagnetic phenomenon. In the 20th century, the discovery of quantum physics improved our knowledge of the microscopic origins of magnetism and light. The idea of spin was too significant it shed new light on the atomic behavior of magnetic materials. Today, optics and magnetism continue to push forward scientific research and technological advancement. From magnetic storage technologies like as hard drives and medical imaging procedures such as MRI (magnetic resonance imaging) to spintronics and magnetic nanoparticles which use electromagnetism and optical principles, these domains continue to be at the top of research.

Ultra-thin films, organic molecules, and organometallic complexes are all different and interconnected research domains with distinct features and uses. Ultra-thin films exhibit quantum unique properties, effects, and surface interactions, making them important for electronics, photonics, catalysis, and magnetic applications. Their magnetic and magneto-optical characteristics are used for data storage and sensing. Organic molecules on the other hand, with their many chemical functions, serve as building blocks for organic electronics, and medicines, while also displaying nonlinear optical properties to be applied in optical signal processing and imaging. Organometallic compounds, which combine organic and inorganic characteristics, are used in catalysis, sensing, and surface functionalization, with future applications in magneto-optics and nonlinear optics. Researchers continue to investigate its fundamental features and enhance applications in a variety of scientific and technological domains through theoretical modeling and experimental collaboration.

From a theoretical perspective, calculations represent an essential in field scientific research complementing experience, allowing experts to examine complicated systems, anticipate experimental outcomes, and gain a better understanding of fundamental phenomena. it uses mathematical models and computer tools to describe the behavior of physical systems ranging from subatomic particles to cosmic scale. Theoretical computations give insights into the fundamental principles driving the dynamics, interactions, and characteristics of complex systems, allowing researchers to push the boundaries of knowledge and develop novel technologies, using quantum mechanics principles such as DFT (density functional theory).

In this study, we have used two different calculation programs that both employ the DFT framework, the first known as the SPR-LMTO-ASA (Spin-Polarized Relativistic - Linear Muffin Tin Orbitals – Atomic Sphere Approximation) which is more specified in the calculation of magnetic and magneto-optical properties, performing under the LSDA (Local Spin Density approximation) that take into account spin and the exchange and correlation effects which represent essential parameters for magnetic properties, this software uses the self-consistent calculation process to calculate the optical conductivity tensor, it also makes it possible to determine the symmetry of the bands involved in interband transitions. It calculates structural properties using pseudomorphic epitaxial growth with the same lattice parameter in the plane of each film imposed by the substrate. The relaxation of the different systems is achieved through a process of optimizing the total energy of the systems studied as a function of the distance between the different atomic planes in each film, in two dimensional frame, square symmetry leads to a flat surface and allows perfect layer-by-layer growth and, consequently, there is no inter-mixing between substrate and the ultrathin film. The distances corresponding to the equilibrium are found after fitting the calculated values with suitable appropriate functions. The optimized structure is then used to study magnetic properties by calculating the magnetic moment and consequently determining the magnetic phase of each film. We perform our study of magneto-optical properties by calculating the magneto-optical Kerr effect spectra in the different ultrathin films via P-MOKE (Polar Magneto-Optical Kerr Effect) and determine the interband transitions responsible for the various peaks appearing in the P-MOKE spectra.

The second is the GAUSSIAN computational chemistry software, which is more accurate with its visualization tools (gaussview) and analysis features in calculating molecular parameters such as

geometries, energies, electronic state, and optical properties of elements using different theoretical approaches, including Hartree-Fock theory along with plenty of approximations such as Generalized Gradient Approximation (GGA) with different methods like Becke 3 Lee-Yang-Parr (B3LYP). This method is used to build the geometric structure then perform structural optimization at the ground state energy level combined with spectroscopic analysis including IR (Infra-Red) and NMR (Nuclear Magnetic Resonance) spectra, frontier molecular orbitals HOMO (High Ocuppied Molecular Orbitals) and LUMO (Low Unocuppied Molecular Orbitals), MEP (Molecular Electrostatic Potentiel) surface analysis and the NLO (Non Linear Optical) parameters such as polarizability, first-and second-order hyperpolarizability (α, β, and γ) in the static and dynamic state.

This dissertation is made up of five chapters, the first one covers all the theoretical formalism, the second chapter is devoted to the tools used for this work, the third chapter explores diverse types of materials, followed by a fourth chapter that discusses the properties of these materials, and a final chapter to present and discuss the obtained results.

Chapter 1
Theoretical Formalism

1.1   Introduction

In recent years science has developed enormously, it started by studying visible objects and now it has gone far to the atomic scale such as particles and electrons, and for each level, there are equations and formalisms that describe these systems.

As a result of classical mechanics limits in the 20th century, quantum mechanics was discovered as a branch of physics that is concerned with studying the atomic world and its properties that are defined by the status of electrons and their movement around its nucleus [1]. New principles have been defined such as wave functions and probability amplitudes that replaced the deterministic trajectories of classical mechanics.

Erwin Schrödinger one of the founders of this new branch in 1925 provided a mathematical description of how the quantum state of a physical system changes over time, which becomes the heart of quantum mechanics its general form is expressed as [2]:

$$\hat{H}\Psi = E\Psi \tag{1.1}$$

where H is the Hamiltonian operator and Ψ is a wave function that is represented by a set of solutions, or eigenstates of the Hamiltonian. Each of these solutions Ψ_n have an associated eigenvalue, and E_n is a real number that satisfies the eigenvalue equation. The detailed definition of the Hamiltonian depends on the studied physical system. There are several well-known examples like the particle in a box or a harmonic oscillator where the Hamiltonian have a simple form and the Schrödinger equation can be solved exactly. But these are simple systems.

Our interest is in complicated systems where multiple electrons interact with multiple nuclei and each particle is exposed to effects from other particles. In this case, a more complicated description of the Schrödinger equation is given [3].

$$\left[\frac{h^2}{2m} \sum_{i=1}^{N} \nabla_i^2 + \sum_{i=1}^{N} V(\boldsymbol{r}_i) + \sum_{i=1}^{N} \sum_{j<i} U(\boldsymbol{r}_i, \boldsymbol{r}_j) \right] \Psi = E\,\Psi \tag{1.2}$$

where the first term is the kinetic energy of the system, the second term is the Coulomb electron-electron interaction and the third term is the Coulomb electron-nuclei interaction.

The Equation (1.2) can't be resolved analyticaly, this challenge led scientists to think of ways that can help solving the Schrodinger equation or at least give approximated results. There are plenty of methods that give approximated solutions to the Schrödinger equation and each of these approximations is suitable for a well-known situation. The most common is perturbation theory, Hartree-Fock, the Thomas-Fermi, The Born-Oppenheimer approximation, and the Density Functional Theory (DFT) [4].

In this chapter, we will establish the theoretical framework within which this work is based on

1.2 Born Oppenheimer Approximation

Oppenheimer and his supervisor Max Born worked on simplifying the Hamiltonian by making assumptions that deal with the quantum mechanics problem. The standard example they worked with is a bunch of nuclei, each with position R_α mass M_α and charge $Z_\alpha e$, interacting with a bunch of electrons, each with position r_i, mass m, and charge $-e$ [4]. The example Hamiltonian is:

$$H = -\sum_j \frac{\hbar^2}{2M_j}\nabla_i^2 - \sum_j \frac{\hbar^2}{2M_j}\nabla_j^2 + V_{jj'} + V_{ii'} + V_{ij} \tag{1.3}$$

where

$$V_{jj'} = \frac{1}{4\pi\varepsilon_0}\sum_{jj',j>j'} \frac{Z_j Z_{j'} e^2}{R_{jj'}} \tag{1.4}$$

$$V_{ii'} = \frac{1}{4\pi\varepsilon_0}\sum_{ii',i>i'} \frac{e^2}{r_{ii'}} \tag{1.5}$$

and

$$V_{ij} = -\frac{1}{4\pi\varepsilon_0}\sum_{ij} \frac{Z_j e^2}{R_{ij}} \tag{1.6}$$

The first two terms in the equation **(1.3)** represent the kinetic energy of the nuclei and the electrons respectively. The remaining three terms specify the potential energy as a function of the interaction

between the particles. The equation **(1.4)** express the potential for the interaction of each pair of nuclei, this sum is composed of terms that are given by Coulomb's law for the repulsion between like-charge particles. Similarly, equation **(1.5)** corresponds to the electron-electron repulsion. Finally, Equation **(1.6)** is the potential for the attraction between a given electron (i) and a nucleus (j) [5].

According to The Born Oppenheimer Approximation, the above Hamiltonian can be simplified because of the mass difference between the nuclei and the electrons. Recall that the proton-to-electron mass deference is $[m_p/m_n = 1836]$, this means that the nuclei are slow compared to electrons, in exchange, the nuclei wave functions are much more localized than the electron wave functions. This motivated Born and Oppenheimer to fix the positions of the nuclei and look at the electron Hamiltonian, and only later solve for the nuclei dynamics. This is the essence of the Born-Oppenheimer assumption [4], that leads to separating the Hamiltonian into two parts.

$$\hat{H} = \hat{H}_{elec} + \hat{H}_{nucl} = -\sum_i \frac{\hbar^2}{2m_i}\nabla_i^2 + V_{ii'} + V_{ij} - \sum_j \frac{\hbar^2}{2M_j}\nabla_j^2 + V_{jj'} \qquad (1.7)$$

The separation of the Hamiltonian allows to separate the wave function into two parts as well

$$\Psi = \Psi_{elec} . \Psi_{nucl} \qquad (1.8)$$

The first three terms in equation **(1.7)** are referred to as the electronic part of the Hamiltonian, while the remaining two terms represent the nuclear Hamiltonian.

The Schrödinger equation for the general problem can then be written as

$$\hat{H}(\Psi_{elec} . \Psi_{nucl})$$
$$= -\sum_j \frac{\hbar^2}{2M_j}\nabla_j^2(\Psi_{elec} . \Psi_{nucl}) - \sum_i \frac{\hbar^2}{2m_i}\nabla_i^2 (\Psi_{elec} . \Psi_{nucl}) \qquad (1.9)$$
$$+ (V_{jj'} + V_{ii'} + V_{ij})(\Psi_{elec} . \Psi_{nucl}) = \mathcal{E}(\Psi_{elec} . \Psi_{nucl})$$

As the first term of equation **(1.9)** express the kinetic energy of the nuclei, it is assumed that the wave function for the electrons is not modified by the corresponding operator. In other words, the movement of the nuclei takes place within the so-called electron cloud that is developed by

the average positions of the ensemble of electrons, inversely in the second term of the equation, the operator over the electronic coordinates does not affect the nuclear wave function, as the nuclear positions are taken to be fixed [5].

Dividing equation **(1.9)** by Ψ_{nucl}

$$\frac{\Psi_{\text{elec}}}{\Psi_{\text{nucl}}} \sum_j \left(-\frac{\hbar^2}{2M_j} \nabla_j^2 \Psi_{\text{nucl}} \right) + \left[\sum_i \left(-\frac{\hbar^2}{2m_i} \nabla_i^2 + V_{ii'} + V_{ij} \right) \Psi_{\text{elec}} \right]$$
$$- (\mathcal{E} - V_{jj'}) \Psi_{\text{elec}} = 0 \tag{1.10}$$

simplified to

$$\sum_j \left(-\frac{\hbar^2}{2M_j} \nabla_j^2 \Psi_{\text{nucl}} \right) + V_{jj'} \Psi_{\text{nucl}} + (\varepsilon_{elec} - \mathcal{E}) \Psi_{\text{nucl}} = 0 \tag{1.11}$$

$$\sum_i \left(-\frac{\hbar^2}{2m_i} \nabla_i^2 + V_{ii'} + V_{ij} \right) \Psi_{\text{elec}} = \varepsilon_{elec} \Psi_{\text{elec}} \tag{1.12}$$

it becomes evident that the electronic energy enters the Hamiltonian for the nuclear motion as an effective potential function. Thus, if the "electronic problem", as given by Equation **(1.12)**, has been solved as a function of the nuclear geometry, the resulting energy contributes to the potential function that governs inter-nuclear displacements.

The argument presented in the preceding paragraph is perhaps easier to understand concerning a diatomic molecule. In this case, equation **(1.12)** is solved for each value of the (fixed) interatomic distance. The resulting electronic energy, as a function of this distance, is then substituted in equation **(1.11)** to yield the Schrodinger equation for the relative nuclear motion, as given by these last equations [5].

It should be emphasized that the Born-Oppenheimer approximation offer a well interpretation for molecular spectra of small molecules, even though it is still limited, and for that other approximations are required.

1.3 Hartree Approximation

Or what is known by the free electron approximation, it was established by Douglas Hartree in 1927, the electron-electron interaction (V_{e-e}) is modeled by assuming that each electron moves within a central field of force that is non-Coulomb in nature. In other words, simplifying the problem by breaking it down into a series of single-electron problems, and the term of electron-electron (V_{e-e}) interaction on a certain electron at position **r** should approximately be represented by an electrostatic potential that is generated by all other electrons on average at position **r** [6].

This allows us to replace the (V_{e-e}) term by:

$$V_{e-e}(\{\boldsymbol{r}_i\}) \approx \sum_{k=1}^{N} \mathcal{V}^{Hartree}(\boldsymbol{r}_k) \tag{1.13}$$

with

$$\mathcal{V}^{Hartree}(\boldsymbol{r}) = \frac{e^2}{4\pi\varepsilon_0} \int \frac{n(\boldsymbol{r}')}{|\boldsymbol{r} - \boldsymbol{r}'|} d^3\boldsymbol{r}' \tag{1.14}$$

The Hamiltonian decomposes into N single-particle and operators vary as a function of **r**, and each electron would be then described by an effective single-particle Schrödinger equation

$$H^e = \sum_{i=1}^{N} h(\boldsymbol{r}_i) = -\sum_i \frac{\hbar^2}{2m}\nabla_i^2 - \frac{1}{4\pi\varepsilon_0}\sum_i\sum_k \frac{Z_j e^2}{|r_i - R_k|} + \frac{1}{8\pi\varepsilon_0}\sum_i\sum_{j\neq i} \frac{e^2}{|r_i - r_j|} \tag{1.15}$$

The wave function that allows us to solve equation **(1.15)** is written as:

$$\Psi(\mathrm{R}, \mathrm{r}) = \Pi_{i=1}^{N}\varphi_i(R, r) \tag{1.16}$$

Formed only by single electron orbitals called Hartree product (HP). By using equation **(1.16)** on equation **(1.15)** we obtain

$$\left(-\frac{\hbar^2}{2m}\nabla_i^2 + \mathcal{V}_{eff}(\boldsymbol{r})\right)\varphi_i(R, r) = E_i\varphi_i(R, r) \tag{1.17}$$

where $\mathcal{V}_{eff}(\boldsymbol{r}) = \mathcal{V}_i^N + \mathcal{V}_{ij}(\boldsymbol{r})$

The $\mathcal{V}_i^N$ and $\mathcal{V}_{ij}(r)$ are the potential functions for the interaction between an electron and a nucleus and the potential function of the interaction between two electrons.

to estimate the effective energy $(\mathcal{V}_{eff})$, we used the mathematical approach method of variations

$$\langle H^e \rangle = \frac{\langle \Psi | H | \Psi \rangle}{\langle \Psi | \Psi \rangle} = \langle \Psi | H | \Psi \rangle \tag{1.18}$$

developing equation **(1.18)**

$$\langle \Psi | H | \Psi \rangle = \sum_i \langle \varphi_i \left\| \left[\frac{-\hbar^2}{2m} \nabla_i^2 - \mathcal{V}_i^N + \frac{1}{8\pi\varepsilon_0} \sum_{j \neq i} \langle \varphi_j \left| \frac{e^2}{|r_i - r_j|} \right| \varphi_j \rangle \right] \right\| \varphi_i \rangle \tag{1.19}$$

the resulting energy is

$$E_i = \langle \varphi_i \left\| \left[\frac{-\hbar^2}{2m} \nabla_i^2 - \mathcal{V}_i^N + \frac{1}{8\pi\varepsilon_0} \sum_{j \neq i} \langle \varphi_j \left| \frac{e^2}{|r_i - r_j|} \right| \varphi_j \rangle \right] \right\| \varphi_i \rangle \tag{1.20}$$

where the $\mathcal{V}_{eff}(r)$ or the Hartree potential is

$$\mathcal{V}_{eff}(r) = -\frac{1}{4\pi\varepsilon_0} \sum_k \frac{Z_j e^2}{|r_i - R_k|} + \frac{1}{8\pi\varepsilon_0} \sum_{j \neq i} \langle \varphi_j \left| \frac{e^2}{|r_i - r_j|} \right| \varphi_j \rangle \tag{1.21}$$

The Hartree approximation is considered to be a simple approach that gives a solution to the Schrödinger equation but it is limited for several reasons such as it is a non-relativistic theory, by ignoring the electromagnetic fields, neglects the electron-electron correlations as it treats each electron as if it moves independently in an average field created by all other electrons and it doesn't take into account the Pauli exclusion principle and for that the results of this approximation are inadequate, which was the reason that led to the Hartree-Fock approximation. [7-9]

1.4   Hartree-Fock Approximation

In 1930, Slater [10] and Fock [11] pointed out that Hartree didn't obey the wave function anti-symmetry principle nor considered the spin, for that they developed a method that describes the electronic wave function of a system in a better way, namely Hartree-Fock approach.

This method treats electrons as fermions where two electrons can not be located in the same quantum state following the Pauli exclusion principle, to ensure the anti-symmetry principle, the Slater determinant is used to give another definition of the wave function

$$\Psi(r_1, r_2 \ldots., r_N) = \frac{1}{\sqrt{N!}} \begin{vmatrix} \varphi_1(r_1) & \varphi_1(r_2) & \ldots & \varphi_1(r_N) \\ \varphi_2(r_1) & \varphi_2(r_2) & \ldots & \varphi_2(r_N) \\ \vdots & \vdots & & \vdots \\ \varphi_N(r_1) & \varphi_N(r_2) & \ldots & \varphi_N(r_N) \end{vmatrix} \tag{1.22}$$

$\frac{1}{\sqrt{N!}}$ is the wave function normalization constant.

The columns are single wave functions and the rows are electron coordinates, in line with our mathematics knowledge, the sign of Equation **(1.22)** will change when we exchange any two rows or columns, which guarantees the anti-symmetry principle. Besides that, it also ensures us that two different electrons won't occupy the same electron state owing to two equivalent rows or columns resulting in the value of determinant zero [9]

The energy result according to the new wave function **(1.22)** is calculated as follows:

$$\langle\Psi|H|\Psi\rangle = \sum_i \left[\left\langle \varphi_i \left| \left(\frac{-\hbar^2}{2m} \nabla_i^2 - \mathcal{V}_i^N + \frac{1}{2}\sum_{i\neq i}\langle\varphi_j(r_j)|\mathcal{V}_{ij}|\varphi_j(r_j)\rangle \right) \right| \varphi_j \right\rangle \right.$$
$$\left. - \frac{1}{2}\sum_{i\neq i}\langle\varphi_i(r_j)\varphi_j(r_i)|\mathcal{V}_{ij}|\varphi_i(r_j)\varphi_j(r_i)\rangle \right] \tag{1.23}$$

as shown in equation **(1.23)** we confirm the existence of two parts in the energy equation the first known part from the Hartree equation and the second part resulted from the consideration of the Pauli principle. The Hartree-Fock approximation is based on the same concept of Hartree that deals with multiple particle systems as a one-particle system in an effective potential created by other

particles. The inherent limitation of this approximation is the slater determinant that makes it hard to calculate and from a digital perspective it takes a long time to be calculated And for that, the necessity of another approximation is needed [11].

1.5   Thomas Fermi Approximation

Thomas [12] and Fermi [13], independently, introduced a semiclassical method to approximate the energy of an electronic system, where they proposed an expression for the total electronic energy, including contributions from kinetic, exchange, and correlation energies. These contributions were initially derived for a homogeneous electron gas, for which good approximations had already been made. The key idea was to extend these approximations to inhomogeneous systems by evaluating the energy densities locally:

$$E_\alpha(\rho) = \int \rho(\boldsymbol{r})\varepsilon_\alpha[\rho(\boldsymbol{r})]\, d\boldsymbol{r} \tag{1.24}$$

Where $\varepsilon_\alpha[\rho(\boldsymbol{r})]$ is the energy density of contribution α (kinetic, exchange, and correlation) calculated locally to the value assumed to be equivalent to the density at each point in space. This was the first time that the local density approximation (LDA) was proposed. We will explain this approximation in detail later on. For a homogeneous gas of electrons, where electron density is related to Fermi energy ε_F by the relation

$$\rho = \frac{1}{3\pi^2}\left(\frac{2m}{\hbar^2}\right)^{\frac{3}{2}} \varepsilon_F^{\frac{3}{2}} \tag{1.25}$$

while the kinetic energy is $T = \dfrac{3\rho\varepsilon_F}{5}$, leading to the kinetic energy density

$$t(\rho) = \frac{3}{5}\frac{\hbar^2}{2m}(3\pi^2)^{\frac{2}{3}}\rho^{\frac{2}{3}} \tag{1.26}$$

thus, the Thomas-Fermi kinetic energy:

$$T_{TF} = C_k \int \rho(\boldsymbol{r})^{\frac{5}{3}} d\boldsymbol{r} \tag{1.27}$$

with $C_k = \frac{3(3\pi^2)^{\frac{2}{3}}}{10} = 2.871$ Hartree and 1 Hartree $= 27.21$ eV, the exchange can be introduced, in the same context, using Slater's expression for a homogeneous electron gas. [14,15].

$$E_x(\rho) = C_x \int \rho(\boldsymbol{r})^{\frac{4}{3}} d\boldsymbol{r} \tag{1.28}$$

with $C_x = 3\left(\frac{(3/\pi)^{1/3}}{4}\right) = 0.739$ Hartree, The inclusion of exchange effects at this level leads to what is known as the Thomas-Fermi-Dirac (TFD) model. Correlation effects can be introduced using Wigner's approximation for a homogeneous electron gas[16]:

$$E_c(\rho) = -0.056 \int \frac{\rho(\boldsymbol{r})^{\frac{4}{3}}}{0.079 + \rho(\boldsymbol{r})^{\frac{1}{3}}} d\boldsymbol{r} \tag{1.29}$$

this approximation is based on the assumption of a homogeneous gas system, which makes it bad for inhomogeneous systems, and for that, a new approximation was required. As it is proven that the only electronic variable in these energy expressions (**1.27, 1.28, 1.29**) is the electron density ρ, in this context the name of density functional was introduced which was the start of a new approximation, the Density Functional Theory.

1.6   Density Functional Theory

In the 1960s, density functional theory (DFT) was developed as an alternative to the Hartree-Fock method with lower computational costs. This method determines the properties of a many-electron system by using the electron density instead of wave functions. This is traced back to the Thomas-Fermi model [17,18] in 1927, which assumed an approximately uniform distribution of electrons in an atom. However, this model still has errors in the exchange of energy and it neglects the electron correlation. The density functional theory was built from a theoretical foundation with the publication of the Hohenberg-Kohn theorems [19,20].

1.6.1   Hohenberg-Kohn Theorem

In 1964 Pierre Hohenberg and Walter Kohn proposed two main theorems that calculate the ground state electronic energy using the electronic density $\rho(r)$ [20].

Theorem 1: the external potential $\mathcal{V}_{ext}(\boldsymbol{r})$ and the obtained total energy E_{total} are functional of the electron density $\rho(r)$

$$E[\rho(r)] = F[\rho(r)] \int \rho(\boldsymbol{r})\mathcal{V}_{ext}(\boldsymbol{r})d\boldsymbol{r} \tag{1.30}$$

$\int \rho(\boldsymbol{r})\mathcal{V}_{ext}(\boldsymbol{r})d\boldsymbol{r}$ represent the nuclei-electron interaction and $F[\rho(r)]$ is a density functional

$$F[\rho(r)] = T[\rho(r)] + V_{e-e}[\rho(r)] = T[\rho(r)] + E_{Hartree}[\rho(r)] + E_{xc}[\rho(r)] \tag{1.31}$$

where $T[\rho(r)]$ represents kinetic energy and $V_{e-e}[\rho(r)]$ represents electron-electron energy that contains according to Hartree-Fock, the Hartree energy $E_{Hartree}[\rho(r)]$, the exchange and correlation energy $E_{xc}[\rho(r)]$ [21].

Theorem 2:   The ground state density in a system corresponds to the lowest energy possible for the system that can be expressed mathematically as follows:

$$E[\rho(r)] \geq E_{GS}[\rho_{GS}(r)] \tag{1.32}$$

$E[\rho(r)]$ represents the calculated energy by a random density $\rho(r)$, while $E_{GS}[\rho_{GS}(r)]$ represents the lowest energy level of the studied system that corresponds to the minimum energy possible or the ground stat density (GS) $\rho_{GS}(r)$ [19].

Even though this theorem provides a method for finding the ground state density and its corresponding energy, it provides no detailed formalism of $F[\rho(r)]$, nor an insight into how to solve the many-electron Schrödinger equation.

1.6.2   Kohn-Sham Equations

In 1965, Walter Kohn and Lu Jeu Sham established a method to determine the density ρ based on the Hartree-Fock idea and the one-electron Schrödinger equation, which was a self-consistent equation that takes into account the exchange and correlation effects [19-22].

$$\left(\frac{-\hbar^2}{2m}\nabla_i^2 - v_{eff}(r)\right)\varphi_i(r) = \varepsilon_i\varphi_i(r) \tag{1.33}$$

The $v_{eff}(r)$ is known as the Kohn-Sham potential which represents the effective external potential, $\varphi_i(r)$ is the Kohn-Sham orbital function, and the ε_i is the energy eigenvalue that correspond to the Kohn-Sham orbitals [19].

The electron density can be expressed with the following operator:

$$\rho(r) = \sum_{i=1}^{N}|\varphi_i(r)|^2 \tag{1.34}$$

the total energy is expressed as:

$$E[\rho(r)] = T[\rho(r)] + E_H[\rho(r)] + \int \mathcal{V}_{ext}(r)\rho(\boldsymbol{r})d\boldsymbol{r} + V_{xc}[\rho(r)] \tag{1.35}$$

in this expression **(1.35)**, $T[\rho(r)]$ is the kinetic energy of non-interactive electrons, $E_H[\rho(r)]$ is the Hartree potential that designs the interaction between electrons, $\mathcal{V}_{ext}(r)$ is external potential as previously defined and $V_{xc}[\rho(r)]$ is the exchange-correlation potential, expressed as:

$$V_{xc}[\rho(r)] = \frac{\delta E_{xc}(\rho)}{\delta\rho(r)} \tag{1.36}$$

the density of the ground state is given by a sum of all occupied orbitals (**1.34**)

$E_{xc}(\rho)$ is composed of the following terms: exchange, correlation, and Coulomb functional, that shows up while calculating the Schrödinger equation energies using the density operator.

The system total energy can be calculated using equation **(1.35)** however it is still impossible due to the unknown form of the $V_{xc}[\rho(r)]$. Which requires the search of an approximation for the exchange and correlation part [19-22].

1.7   Exchange and Correlation Functional

The development of Kohn, Sham and even the Hartree–Fock equations has highlighted the fact that the only remaining unknown part in this formalism is the exchange-correlation. Thus, to solve those two equations, various exchange-correlation functionals have been considered.

The effects generated by electron interactions fall into three categories: exchange, dynamic correlation, and non-dynamic correlation, where the exchange effect results from the antisymmetric of the total wave function concerning the exchange of electronic coordinates, it complies with Pauli's principle. This effect is not influenced by the electron's charge and is taken into account in Hartree-Fock theory because of the antisymmetric of the Slater determinant representing the wave function. The correlation effect refers to the correlation between electronic mobility resulting from inter-electronic coulombian repulsion in $\frac{1}{|r_i - r_j|}$. It mainly relates to correlation effects for core electrons, unlike the exchange effect, which is caused by the electron's charge, however, it is not affected by spin. This effect is neglected by the Hartree-Fock theory.

The third effect arises from the fact that electronic wave functions are formulated in terms of independent particles. This is the correction of self-interaction which leads to a calculation of the pair electron number. The exchange-correlation function must take into account, in addition to what has already been stated, the difference in kinetic energy between the non-interacting imaginary system and the real one. Thus, the calculation of the exchange-correlation energy and potential relies on several approximations [22].

1.7.1   Local Spin Density Approximation (LSDA)

In density functional theory, the Local spin Density Approximation (LSDA) is an uncomplicated approximation that may deliver an accurate exchange-correlation definition. This

approach was first brought out by Kohn and Sham [24], while the Thomas-Fermi model was the origin of this approach [17].

It is simply based on the assumption that the density $\rho(r)$ is considered to be homogeneous electron gas over all the space and that the exchange-correlation potential is a local quantity defined in a position r. The difference between the LSDA and the LDA approximation is that the LSDA take into consideration the concept of spin on the LDA approximation. As a result, the electronic density is split into two parts, The LSDA approximation's advantage is that it enables descriptions of systems placed within an external magnetic field and access to susceptibility [9-19].

$$\rho(r) = \rho\uparrow(r) + \rho\downarrow(r) = \rho(r_\uparrow, r_\downarrow)) \tag{1.37}$$

In other words, exchange-correlation energy with LSDA and LDA can be expressed as:

$$E_{xc}^{LSDA}(\rho(r)) = \int \rho(r)\,\varepsilon_{xc}(\rho(r_\uparrow, r_\downarrow))dr \tag{1.38}$$

$$E_{xc}^{LDA}(\rho(r)) = \int \rho(r)\,\varepsilon_{xc}(\rho(r))dr \tag{1.39}$$

where $\varepsilon_{xc}(\rho(r))$ represents the exchange-correlation energy of each particle. $E_{xc}(\rho)$ could be divided into two sections to put in simpler terms: the exchange E_x term and the correlation term E_c.

$$E_{xc} = E_x + E_c \tag{1.40}$$

E_x referred to as Dirac exchange, it is less complicated than E_c and it can be expressed by

$$E_x(\rho(r)) = -\frac{3}{4}\left(\frac{3}{\pi}\right)^{\frac{1}{3}}\int \rho(r)^{\frac{4}{3}}dr \tag{1.41}$$

Concerning E_c a precise value has been obtained by the use of Ceperly and Alder's Monte-Carlo quantum computations [26]. These values were then approximated by Perdew, Zunger [27], Vosko, Wilk, and Nusair (VWN) [28].

This approach, therefore describes molecules, geometries, and vibration frequencies well especially for systems that have more or less uniform densities such as bulk metals,[25] but is poor

at predicting bonding energies (more than 10%). It overestimates the bond energies and gives gaps that are too small for semiconductors and insulating compounds.

1.7.2   Generalized Gradient Approximation (GGA)

To compensate for the L(S)DA deficiency induced by the density heterogeneity assumption, a density gradient is introduced to the density expression to describe the E_x. This method improves molecular geometries and ground-state energy results and it expressed with spin as

$$E_{xc}^{GGA}(\rho(r)) = \int \rho(r)\, \varepsilon_{xc}(\rho(r_\uparrow, r_\downarrow, \nabla r_\uparrow, \nabla r_\downarrow))dr \qquad \textbf{(1.42)}$$

With calculation, plenty of gradient functions have been yielded by research groups such as the LYP by Lee, Yang, and Par [26], the Becke exchange functional B88 [27] the PW91 by Perdew and Wang [28], and the PBE by Perdew, Burke and Ernzerhof [29] which is regarded as the most suitable electronic structure calculation function approach, that has been applied throughout in most of the projects.

Although with GGA approximation we improved the underestimation of calculated values to a certain extent. However, GGA also exhibits other weaknesses, such as overestimating the lattice constant of the heaviest elements and underestimating the band gap. It also considers the trade-off between computational cost and accuracy.

1.8   Pseudo-Potentials

The pseudo-potential concept is based on the fact that the atoms that compose a crystal are surrounded by several electronic layers, the aim is to minimize the number of variables to be taken into account when solving the problem.

A simple way of simplifying the problem is to consider two groups of electrons, core electrons which are very little influenced by the external environment, and valence electrons, which are responsible for most of the physicochemical properties of materials. This approach greatly reduces the number of equations to be solved, since we minimize the number of electrons in our system. This overcomes the most localized results which require the largest number of plane waves, and therefore computation time.

In pseudo-potential, the norm must be conserved and the charge within the cut-off radius r_c is the same as in the standard. In other words, the charge within the cut-off radius r_c must be the same. The wave function must match the true valence wave function, and in addition, the pseudo-wave function norm must also be the same as the wave function of the total system and we can define it by[30]:

$$\int_0^{r_c} [R_l^{PP}(r)]^2 r^2 dr = \int_0^{r_c} [R_{n,l}(r)]^2 r^2 dr \qquad (1.43)$$

where $R_{n,l}(r)$ represents the radial part of the atomic orbital and $R_l^{PP}(r)$ is a pseudo wave function, both wave functions must satisfy these conditions:

$$R_l^{PP}(r) = R_{n,l}(r) \qquad\qquad r > r_c \qquad (1.44)$$

and the eigenvalues of $R_l^{PP}(r)$ and $R_{n,l}(r)$ are equal $\varepsilon_l^{PS} = \varepsilon_l$

The wave function form $R_l^{PP}(r)$ is chosen in order to cancel out the nodes and oscillations arising from the orthogonalization of wave functions [31] within the sphere radius r_c, the shape of the pseudo-potential is shown in **Figure I.1**
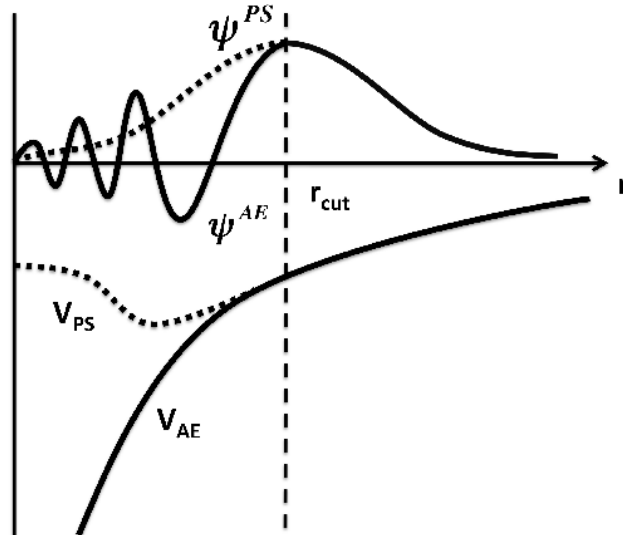
Figure I.1 Form of a pseudopotential and a pseudo wave function (solid line), with comparison to the exact potential and wave function (dashed line).

1.9   Self-Consistent Cycle for DFT

In determining the behavior of electrons in crystals through the solution of the Kohn-Sham equation, and to solve it we need to choose a basis for the wave functions, which can be taken as a linear combination of orbitals, called Kohn-Sham orbitals [2]

$$\psi_j(k,r) = \sum C_{ij}\,\phi_i(k,r) \tag{1.45}$$

where the $\phi_i(k,r)$ are the basis functions and the C_{ij} are the development coefficients.

Solving Kohn and Sham's equations means determining the coefficients for the C_{ij} occupied orbitals that minimize the total energy. This resolution is iterative, using what is known as the self-consistent cycle of iterations illustrated by the flow chart in **Figure I.2**. This is achieved by injecting the initial charge density ρ_{in} to diagonalize the secular equation:

$$(H - \varepsilon_i S) = 0 \tag{1.46}$$

where H represents the Hamiltonian matrix and S is the overlapping matrix.

Then the new charge density ρ_{out} is generated with the eigenvectors of this secular equation, using the total charge density, which can be obtained by summing over all occupied orbitals (**1.34**). If the calculations do not reach convergence the charge densities ρ_{out} and ρ_{in} get mixed as follows:

$$\rho_{in}^{i+1} = (1-\alpha)\rho_{in}^i + \alpha\rho_{out}^i \tag{1.47}$$

i represents the ith iteration and α is the mixing parameter. In this way, the iterative procedure continues until convergence is achieved, this operation is done through a calculation machine using specific programs.
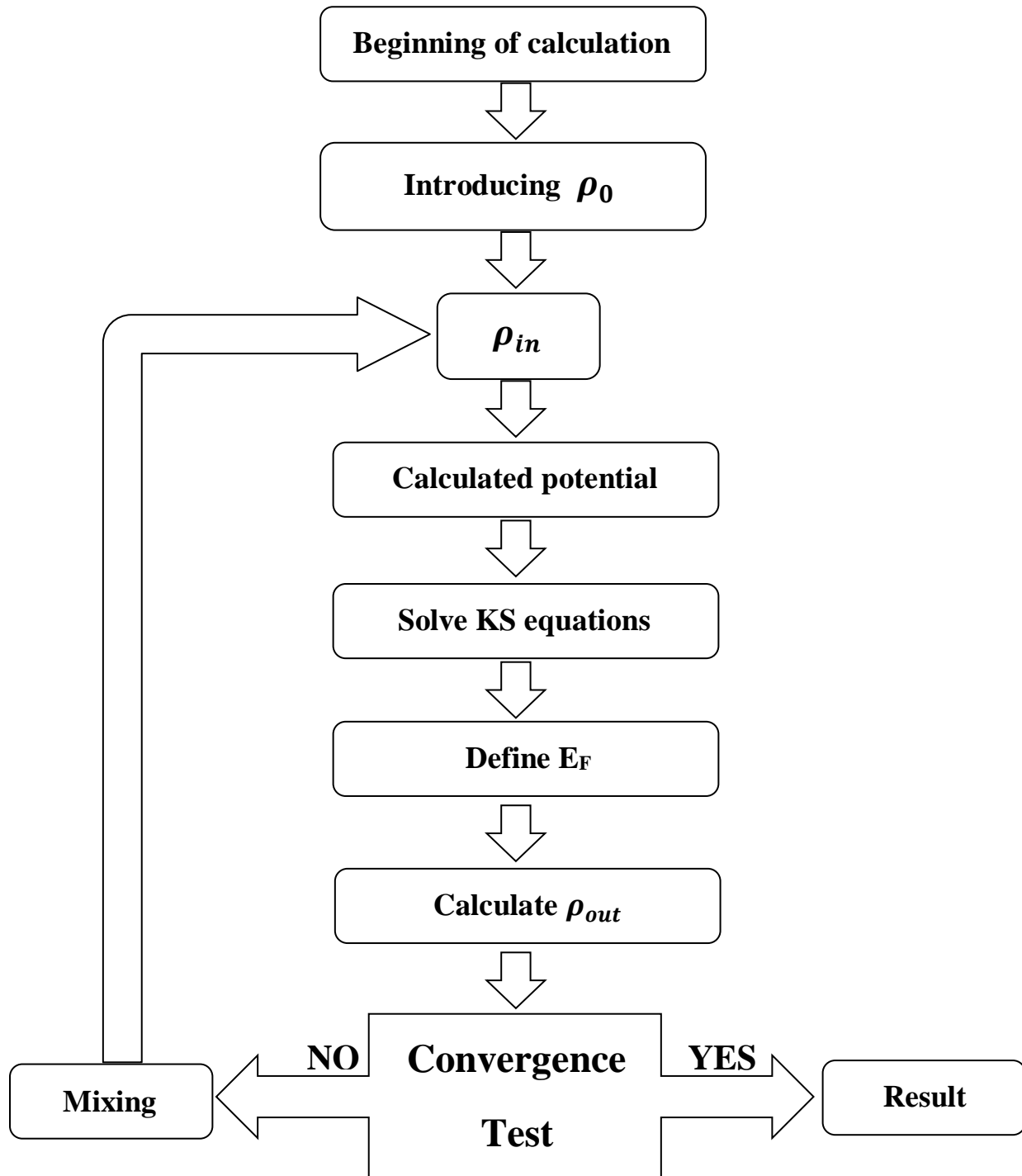
Figure I.2 Self-consistent cycle for density functional theory (DFT).

1.10   Conclusion

In this chapter, we went over the complicated world of quantum mechanics, exploring fundamental concepts like the Born-Oppenheimer and the Hartree-Fock approximations. These theories simplify the many-body Schrödinger equation and lay the foundation for understanding complex chemical and physical phenomena.

Moreover, we've introduced the groundbreaking of DFT and the Hohenberg-Kohn theorems, which have revolutionized the way we approach scientific research. DFT, in particular, has emerged as a reliable and accurate method, widely adopted by scientists, it has transformed theoretical research into a virtual coordination laboratory, enabling unprecedented scientific breakthroughs, one cannot overstate the significance of these advancements in computational science. They empower researchers to perform virtual experiments, predict real-world outcomes, and even explore conditions and characteristics that are beyond the reach of traditional experimental laboratories. Moreover, these advancements significantly reduce the cost and time involved in scientific research, making it more accessible and efficient. These theoretical frameworks have not just remained abstract concepts; they've translated into solid scientific discoveries and technological advancements.

1.11 References

1   Leighton, R. B., & Sands, M. (1965). The Feynman lectures on physics. Boston, MA, USA: Addison-Wesley.

2   Hage-Hassan, M. (2013). An elementary introduction to Quantum mechanic.

3   Sholl, D. S., & Steckel, J. A. (2022). Density functional theory: a practical introduction. John Wiley & Sons.

4   Tong, D. (2017). Applications of quantum mechanics. University of Cambridge Part II Mathematical Tripos.

5   Turrell, G. (2001). Mathematics for chemistry and physics. Elsevier.

6   Hartree, D. R. (1928, January). The wave mechanics of an atom with a non-Coulomb central field. Part I. Theory and methods. In Mathematical Proceedings of the Cambridge Philosophical Society (Vol. 24, No. 1, pp. 89-110). Cambridge university press.

7   HOLLINS, T. (2014). Local Exchange Potentials in Density Functional Theory (Doctoral dissertation, Durham University).

8   Meyer, H. D., Manthe, U., & Cederbaum, L. S. (1993). The multi-configuration Hartree approach. Numerical Grid Methods and Their Application to Schrödinger's Equation, 141-152.

9   Khireddine, A. (2022). Étude théorique des propriétés structurales et optiques des composés organométalliques (Doctoral dissertation).

10   Slater, J. C. (1930). Note on Hartree's method. Physical Review, 35(2), 210.

11   Fock, V. (1930). Approximation method for the solution of the quantum mechanical multibody problems. Z Angew Phys, 61, 126-148.

12   Thomas, L. H. (1927, January). The calculation of atomic fields. In Mathematical proceedings of the Cambridge philosophical society (Vol. 23, No. 5, pp. 542-548). Cambridge University Press.

13   Fermi, E. (1928). A statistical method for determining some properties of the atom and its application to the theory of the periodic system of elements. Journal of Physics , 48 (1-2), 73-79.

14   Dirac, P. A. (1930, July). Note on exchange phenomena in the Thomas atom. In Mathematical proceedings of the Cambridge philosophical society (Vol. 26, No. 3, pp. 376-385). Cambridge University Press.

15   Slater, J. C. (1951). A simplification of the Hartree-Fock method. Physical review, 81(3), 385.

16   Kharoubi, M. (2014). Effet Kerr magnéto-optique dans les multicouches de type Métal magnétique/Métal paramagnétique : FePt (Doctoral dissertation, Université de Sétif 1-Ferhat Abbas).

17   Thomas, L. H. (1927, January). The calculation of atomic fields. In Mathematical proceedings of the Cambridge philosophical society (Vol. 23, No. 5, pp. 542-548). Cambridge University Press.

18   Fermi, E. (1927). Statistical method to determine some properties of atoms. Rend. Accad. Naz. Lincei, 6(602-607), 5.

19   Huang, H. (2021). A density functional theory study into the mechanism and reactivity in heterogeneous system (Doctoral dissertation, Queen's University Belfast).

20   Hohenberg, P., & Kohn, W. (1964). Inhomogeneous electron gas. Physical review, 136(3B), B864.

21   Houcher, A. (2022). Etude des propriétés structurales et magnéto-optiques des films ultraminces déposés par épitaxie pseudomorphique (Doctoral dissertation).

22   Ouarda, B. (2017). Etude des propriétés magnétiques des multicouches métal/oxyde.

23   Baksi, M. (2019). Ab initio investigation of the nanotribological properties of the h-BN/h-BN and the h-BN/Au (111) interfaces (Master's thesis, Middle East Technical University).

24   Kohn, W., & Sham, L. J. (1965). Self-consistent equations including exchange and correlation effects. Physical review, 140(4A), A1133.

25   Hu, P., King, D. A., Crampin, S., Lee, M. H., & Payne, M. C. (1994). Gradient corrections in density functional theory calculations for surfaces: Co on Pd {110}. Chemical physics letters, 230(6), 501-506.

26   Lee, C., Yang, W., & Parr, R. G. (1988). Phys. Rev. B: Condens. Matter Mater. Phys.785-789

27   Becke, A. D. (1988). Density-functional exchange-energy approximation with correct asymptotic behavior. Physical review A, 38(6), 3098.

28   Perdew, J. P., & Wang, Y. (1992). Accurate and simple analytic representation of the electron-gas correlation energy. Physical review B, 45(23), 13244.

29   Perdew, J. P., Burke, K., & Ernzerhof, M. (1996). Generalized gradient approximation made simple. Physical review letters, 77(18), 3865.

30   Khettal, H. (2021). Etude théorique des propriétés catalytiques des surfaces d'alliage à base de métaux de transition: dissociation du méthane sur les surfaces W-Cu (100) et Ru-Cu (100) (Doctoral dissertation).

31   Payne, M. C., Teter, M. P., Allan, D. C., Arias, T. A., & Joannopoulos, A. J. (1992). Iterative minimization techniques for ab initio total-energy calculations: molecular dynamics and conjugate gradients. Reviews of modern physics, 64(4), 1045.

Chapter 2

Calculation Framework

2.1 Introduction

The impact of DFT and related theories is felt across various fields and studies, from materials science to nanotechnology, and they continue to drive innovation. However, the existence of these methods as a pure mathematical form is not enough to perform calculation or data analysis, so the next step is to translate it into an executable program, without affecting their main role which is solving the many-body Schrödinger equation.

Since the beginning of the 1970s, the computer began to be used in solving this equation in elementary quantum systems, the implementation of DFT into software is a multifaceted process that involves transforming the underlying mathematical formulations into practical and numerical computations. To simplify it, the continuous spatial domain is partitioned by dividing it into a grid or mesh. Thus, a new method was created to study the different properties of systems, that got classified into three main principles:

- Empirical methods for which calculations require experimental results.
- Semi-empirical methods for which calculations require both experimental and theoretical calculations
- Ab-initio methods, for which calculations require only fundamental data.

This last principle (ab-initio) went through a development phase to minimize the errors and became an adopted principle in research under the name of the first principle, during the upgrading phase, three groups were developed using the first principle basis [1]

- The Fixed-base methods in which the wave function is expressed in a well-known orbitals basis (Gaussian, plane waves, atomic orbitals, etc.). This class includes the strong-bond method and the orthogonalized plane waves (OPW) method, these methods are better adapted to the "s-p" conduction bands of simple metals [2].
- Cellular methods where space is divided into spheres centered on each atomic site, and separated by an interstitial region, and the solution of the Schrödinger equation inside the sphere is connected to the intersection region. The augmented plane wave method APW (Augmented Plane Waves) [3], and the KKR method

(Korringa, Khon and Rostoker) [4] are the well-known methods in this group that could be applied to a variety of materials.

- Linearized methods which are designed by Andersen [5] to overcome the limitations of previous methods combining their advantages, it includes the Linearized Augmented Plane Waves (LAPW) method and the LMTO method that was used in this work, whose main features will be described in detail.[6].

The above-mentioned methods work on solving the Schrödinger equation:

$$[-\nabla^2 + V(r)]\varphi_j(k) = E_j(k)\varphi_j(k,r) \tag{2.1}$$

This chapter aims to present the calculation methods used in this study by obtaining the Schrodinger equation solution which means finding the wave function, that allows predicting the physical and chemical properties of the studied system, to determine the effect of transition metal geometries, electronic parameters, magnetic moment, and optical, magneto-optical, and non-linear optical properties.

2.2   Linear Muffin-Tin Orbitals (LMTO)

One of the models used in this work is the LMTO model of Andersen (1975),[5] the code was written by Ove Jepsen from the Max Planck Institute in Stuttgart. The LMTO is a linear method that is based on the concept that the potential in an atomic system is spherically isotropic on the inside, constant on the outside with a certain radius (R_{MT}), and centered at the atomic sites or what is known as the Muffin-tin approximation, [3].

$$V(\boldsymbol{r}) = \begin{cases} V(|\boldsymbol{r}|), & \text{if } |\boldsymbol{r}| \leq R_{MT} \\ C, & \text{if } |\boldsymbol{r}| > R_{MT} \end{cases} \tag{2.2}$$

2.2.1   Atomic Sphere Approximation

The hardware performance at that time was much lower therefore some additional approximations were added and consequently several changes got introduced to enhance the obtained results. By introducing the Atomic Sphere Approximation originated from the Wigner-Seitz (WS) method of 1933, which consists of performing the calculations over WS spheres with a radius S_{ws} and a volume equal to the WS primary cell volume Ω of the associated atoms, this approach tends to make the sphere bigger [3].

For a crystal containing a single atom per primary lattice, the radius S of WS is therefore defined by $\Omega = \left(\frac{4\pi}{3}\right) S^3$

the solution of the Schrödinger equation (**2.1**) is given by the expression:

$$\varphi_L(E, r) = u_l(E, r) i^l Y_L(\hat{r}) \tag{2.3}$$

where $Y_L(\hat{r})$ is a real spherical harmonic, L is short for lm, i^l is inserted according to the phase agreement of Condon and Shortle [7], and φ_L is the solution of the radial function of the energy E and the potential $v_r(r)$, as well as the wave function for a valence electron in a crystal written as:

$$\psi_k(E, r) = \sum_L C_L(k) \sum_R e^{-ik.R} \theta(r - R) \varphi_L(E, r - R) \tag{2.4}$$

where R is the lattice vector, $C_L(k)$ are coefficients obtained for a given energy E and wave vector K, so that the function $\psi_k(E, r)$, and its derivative are continuous from one cell to another, where $\theta(r - R)$ is a function equal to unity inside the cell located at the origin and null outside [8]. Equation **2.4** is the solution of the Schrödinger equation for two conditions, the $C_L(k)$ is determined through an identified energy E and wave vector **k**, the $\psi_k(E, r)$ derivatives are continuous functions from between WS atomic spheres that have similar volumes with frontier conditions specified in a logarithmic derivative defined by:

$$D_l(E) = \frac{s u_l'(E, s)}{u_l(E, s)} \tag{2.5}$$

"s" is the radius of the atomic sphere defined by the condition

$$s = \left(\frac{3\Omega_0}{4\pi}\right)^{\frac{1}{3}} \tag{2.6}$$

Ω_0 is the Wigner-Seitz cell volume

2.2.2   LMTO-ASA Method

The Muffin-Tin orbitals approximation in their non-relativistic **A-44** or relativistic   **A-65** (Appendix A)forms are used as the basis set in the variational process, which leads to solving the following equation:

$$det\left|\langle \chi_{l'}^k(r-R)|H - E|\chi_l^k(r-R)\rangle\right| = 0 \tag{2.7}$$

The calculations to solve this equation are really difficult and long, for this reason we will use the energy-independent Muffin-Tin orbitals to facilitate calculations

2.2.2.1   Basis Functions

Due to the spherical symmetry of the potential within the atomic sphere, the basis functions are written as a product of the radial solution using spherical harmonics. In the LMTO-ASA method, the radial wave function is described as a Taylor series development at a point E_v, taking into consideration the linear terms only.

Let's Consider $\Phi_v(r)$ as an exact solution of a radial equation, for an energy E_v and $\dot{\Phi}_v(r)$ as its derivative concerning the energy, i.e. [9].

$$\Phi_v(r) = u_l(E_v, r) \;\; ; \;\; \dot{\Phi}_v(r) = \left.\frac{\partial u_l(E, r)}{\partial E}\right|_{E=E_v} \tag{2.8}$$

On the inside of the muffin-tin sphere, we create an approximate radial solution $\Phi\,(D, r)$ of the Schrödinger equation through the following relation [9]:

$$\Phi(D,r) = \Phi_v(r) + \omega(D)\dot\Phi_v(r) \tag{2.9}$$

with

$$\omega(D) = -\frac{\Phi_v(s)D - D_v}{\Phi_v(s)D - D_{\dot v}} \tag{2.10}$$

$$D_v = S\frac{\Phi'_v(s)}{\Phi_v(s)} \tag{2.11}$$

$$D_{\dot v} = S\frac{\dot\Phi'_v(s)}{\dot\Phi_v(s)} \tag{2.12}$$

this symbol ($'$) refers to $\frac{\partial}{\partial r}$, and the value of the function (**2.9**) at the edge of the sphere is:

$$\Phi(D,s) = \Phi(D) = \Phi_v\left(\frac{D_v - D_{\dot v}}{D - D_{\dot v}}\right) \tag{2.13}$$

In the basis functions set:

$$\Phi_L(D,r) = i^l Y_L(\hat r)\Phi_l(D,r) \tag{2.14}$$

the matrix components of both the Hamiltonian and the recovery have the form:

$$\langle\Phi_{L'}(D')|H - E_v|\Phi_L(D)\rangle = \delta_{LL'}\omega_l(D) \tag{2.15}$$

$$\langle\Phi_{L'}(D')|\Phi_L(D)\rangle = \delta_{LL'}(+1\langle\dot\Phi_{vl}^2\rangle\omega_l(D)) \tag{2.16}$$

At this point, we have only considered a single atomic sphere, while to describe the crystal, all the other spheres must be taken into account. Their influence on the energy spectrum is defined as a combination of potential parameters: $D_v, s\Phi_{vl}^2$, $s\Phi_v$, $s\dot\Phi_v$ and $\langle\dot\Phi_{vl}^2\rangle$.

The first three parameters depend considerably on the chosen energy E. In fact, it is convenient to use $\omega(D_1), s\Phi^2(D_1)$ and $\frac{\Phi(D_1)}{\Phi(D_2)}$ where $D_1 = -l - 1$ and $D_2 = l$ and for that the equations (**2.09, 2.10, 2.11, 2.12**) are written as follow:

$$\Phi_l(D,r) = \frac{\omega_l(D) - \omega_l(-l-1)}{\omega_l(l) - \omega_l(-l-1)}\Phi_l(l,r) + \frac{\omega_l(D) - \omega_l(l)}{\omega_l(-l-1) - \omega_l(l)}\Phi_l(-l-1,r) \quad \textbf{(2.17)}$$

$$\frac{\omega_l(D) - \omega_l(-l-1)}{\omega_l(D) - \omega_l(l)} = \frac{\Phi_l(s,-l-1)}{\Phi_l(s,l)}\frac{D+l+1}{D-l} \qquad \textbf{(2.18)}$$

$$\Phi_l(s,D) = \frac{(2l-1)\Phi_l(s,-l-1)\Phi_l(s,l)}{(D+l+1)\Phi_l(s,-l-1) - (D-l)\Phi_l(s,l)} \qquad \textbf{(2.19)}$$

therefore, in Anderson's approximation [5], the muffin-tin orbital is written as:

$$\chi_L^k(r,D) \approx \frac{\omega_l(l) - \omega_l(D)}{\omega_l(l) - \omega_l(-l-1)}\chi_L^k(r) = \alpha_L(D)\chi_L^k(r) \qquad \textbf{(2.20)}$$

the muffin-tin orbital $\chi_L^k(r)$ is independent of energy and can be written as:

$$\chi_L^k(r) = \Phi_L(r,-l-1) - \Phi_l(s,-l-1) \times \sum_{L'} S_{LL'}^k \frac{\Phi_{L'}(r,l')}{2(2l'+1)\Phi_l(s,l')} \qquad \textbf{(2.21)}$$

$S_{LL'}^k$ is a structural factor.

In **A-49**, the second term is the sum of all contributions of the other atoms in the crystal.

The muffin-tin orbital representation as a product of $\alpha_L(D)$ through an energy-independent orbital is very useful, as it causes no change in the energy spectrum, but it does affect the wave function normalization within the sphere.

2.2.3   Spin-Polarized Relativist (SPR)-LMTO-ASA
2.2.3.1   Dirac Equation for a Spin-Dependent Potential

There are many relativistic effects, which are caused by the simultaneous presence of spin polarization and spin-orbit coupling, such as the Kerr effect. By mean the investigation of a

polarized spin system, compared to the non-relativistic one, leads to a set of Kohn-Sham-Dirac equations that describe the ground state of a relativistic multi-electron system.

This approach leads to the theory of the common density functional, in which current density J^{μ} is the key quantity instead of the electron density described in the DFT framework.

The Hamiltonian for this approach has the form:

$$H = \alpha \left[\frac{c}{i}\nabla + A_H(J^{\mu}) + A_{xc}(J^{\mu})\right] + \frac{1}{2}(\beta - I) + V_H + V_{xc} \qquad (2.22)$$

where α and β are both Dirac matrices, H, and xc designate the Hartree, exchange, and correlation forces in the vector potential A and scalar potential V respectively.

Due to the complexity of the above Hamiltonian, a new approach has been suggested [10] in which the existence of an effective magnetic field is assumed for exchange and correlation. The corresponding Hamiltonian is:

$$H = \frac{c}{i}\nabla + \frac{1}{2}(\beta - I) + V(r) \qquad (2.23)$$

where

$$V(r) = V_H(r) + V_{xc}(r) + V_{spin}(r) = V^0(r) + V_{spin}(r) \qquad (2.24)$$

$V_{xc}(r)$ represents the spin part of the exchange and correlation potential, while $V_{spin}(r)$ is defined by:

$$V_{spin}(r) = \beta\sigma[B_{ext} + B_{xc}] = \beta\sigma B_{eff} \qquad (2.25)$$

with

$$B_{ext} = \frac{\delta}{\delta m} E_{xc}[n, m] \tag{2.26}$$

$$B_{xc} = \frac{\delta}{\delta n} E_{xc}[n, m] \tag{2.27}$$

n and m are the electron density and spin magnetization density respectively, B_{ext} is the external magnetic field and σ is the 4×4 Pauli matrix.

2.2.3.2   Relativistic LMTO Method

As we discussed in the relativistic muffin-tin approximation subsection this method is a more general application of Anderson's technique in calculating the band structure in the relativistic case. By solving the Dirac equation starting from equation **A-49** and its solutions that become [5]:

$$\phi_\Lambda(r, E) = \begin{pmatrix} g_k(r, E)\chi_k^\mu(\hat{r}) \\ if_k(r, E)\chi_{-k}^\mu(\hat{r}) \end{pmatrix} \tag{2.28}$$

Λ notation stands for relativistic quantum numbers (k, μ), with the radial functions $g_k(r, E)$, $f_k(r, E)$ and the spin angular functions $\chi_k^\mu(\hat{r})$ that defined as

$$\chi_k^\mu(\hat{r}) = \sum_{m_s=\pm\frac{1}{2}} C(l\frac{1}{2}j; \mu - m_s, m_s) Y_l^{\mu - m_s}(\hat{r})\chi_{m_s} \tag{2.29}$$

and the normalized $\phi_\Lambda(r, E)$ inside the sphere of radius (s) leads to the following formula [11]:

$$(H - E)\phi_\Lambda(r, E) = 0 \tag{2.30}$$

$$(H - E)\dot{\phi}_\Lambda(r, E) = \phi_\Lambda(r, E) \tag{2.31}$$

$$\langle \phi_\Lambda(r,E)|\phi_\Lambda(r,E)\rangle = 1 \tag{2.32}$$

$$\langle \phi_\Lambda(r,E)|\dot{\phi}_\Lambda(r,E)\rangle = 1 \tag{2.33}$$

to determine the solutions of the equations (inside the sphere) from the solutions outside the sphere, we introduce the logarithmic derivative $\phi_{\nu\Lambda}(r)$ and $\dot{\phi}_{\nu\Lambda}(r)$ as follows

$$D_{\dot{\nu}k} = s\frac{c\dot{f}_{\nu k}(s)}{\dot{g}_{\nu k}(s)} - k - 1 \tag{2.34}$$

the symbol ν indicates that the energy is defined by an E_ν.

The basis functions $\Phi_\Lambda(r,D)$ for r ≤ s with a logarithmic derivative D for r = s, are obtained through the coordination of $\phi_{\nu\Lambda}(r)$ and $\dot{\phi}_{\nu\Lambda}(r)$ by analogy with the non-relativistic case through the following relationship

$$\Phi_\nu(r,D) = \phi_{\nu\Lambda}(r) + \omega_k(D)\dot{\phi}_{\nu\Lambda}(r) \tag{2.35}$$

the $\omega_k(D)$ coefficient is defined by:

$$\omega_k(D) = -\frac{g_{\nu k}(s)D - D_{\nu k}}{\dot{g}_{\nu k}(s)D - D_{\dot{\nu}k}} \tag{2.36}$$

it ensures the continuity and differentiability of $\Phi_\nu(r,D)$ at r = s (the sphere edge).

In the ASA approximation, the potential inside the interstitial region is chosen so that $E - V(r) = 0$ to avoid diverging solutions $n_\Lambda(r)$ and $j_\Lambda(r)$, that represents the relativistic Newman and Bessel functions respectively.

The muffin tin orbital $\chi_\Lambda(r - R)$ is defined as a centered function in the R lattice site, it is determined if the descending solution $n_\Lambda(r)(r - R)$ is increased in the sphere centered at R by $\Phi_\Lambda(-l - 1, r - R)$ and through a linear combination of the functions $\Phi_{\Lambda'}(l', r - R')$ in the other spheres centered at R' so that the $\chi_\Lambda(r - R)$ orbital is continuous at all points.

To create all the crystals, we use the Bloch theorem through the sum to get

$$\chi_\Lambda^k(r) = \sum_R e^{ik.R} \, \chi_\Lambda(r-R)$$ (2.37)

it can be written as:

$$\chi_\Lambda^k(r) = \frac{\Phi_\Lambda(-l-1,r)}{\sqrt{\frac{s}{2g_k(-l-1)}}} - \sum_{\Lambda'} \frac{\Phi_{\Lambda'}(l',r)}{2(2l'+1)\sqrt{\frac{s}{2g_{k'}(l')}}} \sigma_{\Lambda\Lambda'}^k$$ (2.38)

where $g_k = \Phi_\Lambda(s,D)$, and $\sigma_{\Lambda\Lambda'}^k$ is the relativistic structural factor given by the relation:

$$\sigma_{\Lambda\Lambda'}^k = \sum_{m_s=\pm\frac{1}{2}} C(l'\tfrac{1}{2}j'\,;\,\mu'-m_s,m_s) \times S_{l'\mu'-m_s,l\mu-m_s}^k C(l\tfrac{1}{2}j\,;\,\mu-m_s,m_s)$$ (2.39)

with $S_{l'\mu'-m_s,l\mu-m_s}^k$ is the non-relativistic canonic structural factor,

Using the Bloch sum of the muffin-tin orbitals in the application of the principle we end up with the following eigenvalue problem

$$\chi_\Lambda^k(r) = \sum_\Lambda \left(H_{\Lambda\Lambda'}^k - E^{jk}O_{\Lambda\Lambda'}^k\right)\alpha_\Lambda^{jk} = 0$$ (2.40)

with

$$\langle \phi_{\Lambda'}(r,D')|(H-E)|\phi_\Lambda(r,D)\rangle = \omega_k(D)\delta_{\Lambda\Lambda'}$$ (2.41)

$$\langle \phi_{\Lambda'}(r,D')|\phi_\Lambda(r,D)\rangle = \left[1 + \omega_k(D')\omega_k(D)\langle\dot\phi_{vk}^2\rangle\right]\delta_{\Lambda\Lambda'}$$ (2.42)

The matrix elements of the $H_{\Lambda\Lambda'}^k$ and the overlay $O_{\Lambda\Lambda'}^k$ Hamiltonian in equation (**2.42**) are expressed by the structural factor matrix and the potential parameters $\omega_k(-)$, $\frac{\Phi(-)}{\Phi(+)}$ and $\langle\dot\phi_{vk}^2\rangle$ with $+$ and $-$ represent $+l$ and $-l-1$

Explicit expressions for $H_{\Lambda\Lambda'}^k$ and $O_{\Lambda\Lambda'}^k$ can be derived from the non-relativistic formula by making the following substitutions

$$L = (l, m) \rightarrow \Lambda = (k, \mu)$$

$$\Phi_l(D) \rightarrow g_k(D)$$

2.2.3.3   SPR-LMTO Method

The SPR-LMTO-ASA (Relativistic Spin-Polarized LMTO) method is designed to calculate the spin-polarized systems. Ferromagnetic systems exhibit structural properties of this character, hence the necessity of using this method to study the system of this work. Generally, an accurate solution to the band structure problem in the relativistic framework that considers spin polarization has been obtained apart from the perturbation method. Due to that, we considered the relativistic muffin-tin orbitals using the Eigen-solutions with a spin-dependent potential of the one-particle Dirac equation.

It has been proven by Feder et al. [12], Strange et al. [13], and Cortona et al. [9] that the spin-dependent potential in the Dirac equation leads to an unlimited number of paired equations of the radial function. To avoid this situation, it has been illustrated that the coupling between the radial functions can be ignored except those with $\Delta l = 0$ and $\Delta \mu = 0$ [12], so the Dirac equation is written as:

$$\phi_i(r, E) = \phi_{\Lambda i}(r, E))\phi_{\overline{\Lambda} i}(r, E) \tag{2.43}$$

$\Lambda = (k, \mu)$, $\overline{\Lambda} = (-k - 1, \mu)$ and i represent the independent solutions of equation (**2.24**).

By Normalizing the function $\phi_i(r, E)$ within the Sphere of radius s, along with its derivative concerning energy $\dot{\phi}_i(r, E)$ solve the following equations:

$$(\text{H} - \text{E})\phi_i(r, E) = 0 \tag{2.44}$$

$$(H - E)\dot{\phi}_i(r, E) = \phi_i(r, E) \tag{2.45}$$

$$\langle \phi_i(r, E)|\phi_i(r, E)\rangle = 1 \tag{2.46}$$

$$\langle \phi_i(r, E) | \dot{\phi}_i(r, E) \rangle = 1 \qquad \textbf{(2.47)}$$

The formation of a relativistic SPR-LMTO orbital using the LMTO method leads to a complicated Hamiltonian and overlapping matrix, and the solution is to add solutions to the interstitial area $n_\Lambda(r)$ inside the central sphere using the $\phi_\Lambda(-l-1, r)$ function and in the remaining spheres by a linear combination of functions $\phi_{\Lambda'}(+l', r)$.

The equations of the SPR-LMTO method are completely similar to the equations for the unpolarized spin case. Using the potential parameters $\alpha_{i\Lambda}(D)$ and $\beta_{i\Lambda}(D)$ the matrices elements and the overlap matrices are given by:

$$\langle \phi_{\Lambda'}(D') | \phi_\Lambda(D) \rangle$$

$$= \sum_{i,i'} \begin{bmatrix} \alpha_{i'\Lambda'}(D')\alpha_{i\Lambda}(D)\langle \phi_{i'}|\phi_i\rangle + \alpha_{i'\Lambda'}(D')\beta_{i\Lambda}(D)\langle \phi_{i'}|\dot{\phi}_i\rangle \\ +\beta_{i'\Lambda'}(D')\alpha_{i\Lambda}(D)\langle \dot{\phi}_{i'}|\phi_i\rangle + \beta_{i'\Lambda'}(D')\beta_{i\Lambda}(D)\langle \dot{\phi}_{i'}|\dot{\phi}_i\rangle \end{bmatrix} \qquad \textbf{(2.48)}$$

$$\langle \phi_{\Lambda'}(D') | (H-E) | \phi_\Lambda(D) \rangle$$

$$= \sum_{i,i'} [\alpha_{i'\Lambda'}(D')\beta_{i\Lambda}(D)\langle \phi_{i'}|\phi_i\rangle + \beta_{i'\Lambda'}(D')\beta_{i\Lambda}(D)\langle \dot{\phi}_{i'}|\phi_i\rangle] \qquad \textbf{(2.49)}$$

Within the framework of the SPR-LMTO method, the estimation of the matrix elements corresponding to the values of operators must be expressed in terms of the solutions of the single-particle Dirac equation $\phi_i(r, E)$ (**2.44**) and their energy derivatives $\dot{\phi}_i(r, E)$, instead of using the Bloch sum of the orbitals $\chi_\Lambda^k(r)$ which has the same (**2.41**) equation form. Thus, the Bloch wave function is written as:

$$\Psi^{jk}(r) = \sum_L [A_i^{jk}\phi_i(r) + B_i^{jk}\dot{\phi}_i(r)] \qquad \textbf{(2.50)}$$

the coefficients A_i and B_i must be defined in terms of the eigenvectors α_Λ^{jk} that occur in the development of the wave function as a function of $\chi_L^k(r)$ which mean [14,15].

$$\Psi^{jk}(r) = \sum_L C_L^k \, \chi_L^k(r) \tag{2.51}$$

Finally, it is worth mentioning that the ASA approximation can be taken into account if we use the associated correction terms as part of the RLMTO method.

2.2.4   Band Structure Calculations

The wave functions of a crystal are defined as a linear combination of Bloch's basis functions.

$$\Psi^{jk}(r) = \sum_L C_L^k \, \chi_L^k(r) \tag{2.52}$$

The energy corresponding to its wave functions is obtained from the variational principle

$$E(k) = \frac{\langle \Psi_L^k | H - E | \Psi_L^k \rangle}{\langle \Psi_L^k | \Psi_L^k \rangle} \tag{2.53}$$

leading to the following secular equation:

$$det \left| \langle \Psi_L^k | H | \Psi_L^k \rangle - E \langle \Psi_L^k | \Psi_L^k \rangle \right| = 0 \tag{2.54}$$

the functions $\chi_L^k(r)$ are written in a way to highlight the direct use of the potential parameters in the numerical calculation of the Hamiltonian matrix overlapping elements.

2.2.5   Convergence and Stability

To reach the necessary coherence, an iterative process is done and consists of developing the input potential $V_{n+1}(r)$ at the $(n+1)^{th}$ iteration from the output density $\rho_n^{out}(r)$ of the $(n)^{th}$ iteration. Theoretically, convergence is achieved when the potential $V_{n+1}(r)$ yields a density $\rho_{n+1}^{out}(r) = \rho_n^{in}(r)$

with

$$\rho_{n+1}^{in}(r) = \alpha_n \rho_n^{in}(r) + (1 + \alpha_n)\rho_n^{out}(r) \qquad (2.55)$$

α_n is the mixing factor, it ranges from zero to one, depending on the problem and the accuracy, which is taken 10^{-6} for our work.

2.3   GAUSSIAN Program

Gaussian is a computational chemistry program for general use on any size and type of molecular systems, originally developed in 1970 by John Pople and his research group at Carnegie Mellon University, who later received the Nobel Prize in Chemistry for his contributions. This program is based on solving the Schrödinger equation with different theoretical models (Hartree-Fock, DFT…) using the Gaussian-type orbitals to represent the behavior of electrons in molecules. which permit the studying and describing molecular structures, energies, vibration frequencies, spectroscopic (NMR, IR, UV, etc.), electronic properties, thermodynamic parameters, optical properties, and much more advanced calculations for a wide range of systems (condensed phases, surfaces, gas-surfaces, and molecules …) through the determination of the optimal form (equilibrium geometry), total energy, and vibration frequencies (harmonic frequencies) for structures at the lowest points of a potential surface. The total energy is what the system would have if the atomic cores remained stationary at these low positions. The vibration rates help calculating a correction (zero-point correction) that determines the lowest energy state of the molecule [16].

2.3.1   Computational Methods

The Gaussian program contains a hierarchy of procedures corresponding to different approximation methods. In the last few years, methods based on Density Functional Theory have gained slowly gaining popularity. The best DFT methods achieve significantly greater accuracy than the Hartree-Fock theory at only a modest increase in cost, they do so by including some of

the effects of electron correlation, much less expensively than traditional correlated methods. DFT methods compute electron correlation via general functionals of the electron density, which splits the electronic energy into components: the kinetic energy, the electron-nuclear interaction, the Coulomb repulsion, and an exchange-correlation term accounting for the remainder of the electron-electron interaction which are computed separately. Various functionals have been defined, which are usually characterized by how they handle the exchange and correlation parts like the treatment of Vosko, Wilk, and Nusair (VWN) or the Non-local functional proposed by Becke, the LYP functional of Lee, Yang, and Parr or the combination of this two with B-LYP method and its hybrid functionals B3LYP that was developed in the late '80s, B3 referred to Becke's 3-parameter exchange and correlation function, which uses three parameters to combine exact Hartree-Fock exchange-correlation, and LYP is Lee Yang and Parr's correlation function, which recovers dynamic electron correlation. B3LYP is popular for many reasons, it was one of the first DFT methods that represented a significant improvement over Hartree-Fock.

 B3LYP is generally faster than most Post-Hartree-Fock techniques and generally gives good agreement with the experimental data, it is also robust enough for a DFT method. At a more fundamental level, it is not as strongly parameterized as other hybrid functionals, having only 3 while some have up to 26 [17].

2.3.2   Basis Sets

A basis set is a mathematical representation of electronic orbitals of a system that is applied for theoretical calculations, which then combine to approximate the whole electronic wave function. In other words, basis sets may be identified by the approximation types for electronic orbitals they use, and by that, it means placing constraints on the positions of electrons in orbits. The larger basis sets and the more accurate calculations are, simultaneously requiring more computational resources [16].

Gaussian provides a large selection of predefined basis sets and the first basis sets are the minimal basis sets that use fixed size atomic type orbitals or what is known as the Slater Type Orbitals (STO)

$$\Psi = \alpha_1 \phi_1 + \alpha_2 \phi_2 + \alpha_3 \phi_3 + \cdots \alpha_k \phi_k \tag{2.56}$$

with k is the basis set size, ϕ_n is the basis functions and α_n is the normalization constant, it was first established by J.C. Slater, That has been used as basis functions.

$$BF = N \times e^{(-\alpha r)}. \tag{2.57}$$

where N is the normalization constant α is the orbital exponent and r is the radius STOs are described by the function depending on spherical coordinates

$$\phi_1(\alpha, n, l, m; r, \theta, \phi) = N r^{n-1} \times e^{(-\alpha r)} Y_{l,m}. \tag{2.58}$$

the r, θ and ϕ are spherical coordinates, $Y_{l,m}$ is the angular momentum part n, l, and m are quantum numbers.

This basis function is used only for diatomic molecules or hydrogen-like molecules and non-polarized molecules, which considred to be simpler systems, However, for more complex systems, especially those involving heavier molecules, STOs can be less accurate due to the difficulty in efficiently performing multi-center integrals[18,19]. After that, a new type of atomic orbital called "Gaussian-type orbitals" (GTOs) emerged, known as the 3G, being easy to work with but less accurate individually. However, by combining multiple GTOs in specific ways, scientists did achieve accuracy similar to STOs while retaining computational efficiency. This paved the way for a more practical approach to studying atomic behavior. This basis function is defined with[20]

$$GTO(3G) = c_1 e^{(-\beta_1 r^2)} + c_2 e^{(-\beta_2 r^2)} + c_3 e^{(-\beta_3 r^2)} \tag{2.59}$$

c and β values are fixed and can be found differently, for a Cartesian Gaussian centered on atom, it can be represented as:

$$G_{i,j,k} = N x_a^i y_a^j z_a^k e^{(-\alpha r_a^2)} \tag{2.60}$$

where i, j, and k are nonnegative integers, α is a positive orbital exponent, x_a, y_a and z_a are cartesian coordinates with the origin at a, and N is the cartesian Gaussian normalization constant. This constant is expressed as [20]:

$$N = \left(\frac{2\alpha}{\pi}\right)^{\frac{3}{4}} \left[\frac{(8\alpha)^{i+j+k} i!\,j!\,k!}{(2i)!\,(2j)!\,(2k)!}\right]^{\frac{1}{2}} \tag{2.61}$$

The numerical approximations (basis sets and grids) are developed to meet the required convergent limits. The 6-31G known as Double and Triple zeta basis sets was developed by Pople et al. [21]. As the first basis sets that uses angular momentum to the orbitals that got upgraded polarized split valance 6-311G++(d,p) as a polarized basis set for heavy atoms to become a most used basis set for medium-sized systems [22], which are based on Møller and Plesset [23] perturbation method.

Plenty of other approaches that came after that were based on these two basis functions such as the one introduced by E.J Baerends known as Approximate molecular orbitals (AMOL) uses slater-type functions that ensure more harmonious development [24]. The **Density Functional Molecular Orbital** or what is known as DMol3 by B. Delley in 1990 [25], it provides flexible mathematically determined basis sets.

2.4   Conclusion

This chapter introduces the used programs in this work, by solving the Kohn-Sham equation iteratively through self-consistent field (SCF) calculations, often starting with an initial guess for the electron density. These iterations continue until self-consistency is achieved. Additionally, DFT software provides a choice of exchange-correlation functions, including popular ones like LDA and GGA, each with its approximations and advantages. Pseudopotentials are optionally used to simplify the representation of core electrons, making calculations more efficient, to handle large systems and expedite calculations, parallel computing techniques are commonly employed. The results are presented in user-friendly interfaces that allow researchers to input system specifications, select methods, and configure parameters. Comprehensive documentation, including manuals and tutorials, supports users in setting up and running calculations.

2.5   References

1   Ovchinnikov, S. G., & Val'kov, V. V. (2004). Hubbard operators in the theory of strongly correlated electrons. World Scientific.

2   Herring, C. (1940). A new method for calculating wave functions in crystals. Physical Review, 57(12), 1169.

3   Korringa, J. (1947). On the calculation of the energy of a Bloch wave in a metal. Physica, 13(6-7), 392-400.

4   Slater, J. C. (1937). Wave functions in a periodic potential. Physical Review, 51(10), 846.

5   Andersen, O. K. (1975). Linear methods in band theory. Physical Review B, 12(8), 3060.

6   Crockford, D. J. (1990). LMTO studies of transition metals: Non-collinear magnetism and axial pressures. University of Bath (United Kingdom).

7   Condon, E. U., & Shortley, G. H. (1935). The theory of atomic spectra. Cambridge University Press.

8   Andersen, O. K., & Woolley, R. G. (1973). Muffin-tin orbitals and molecular calculations: General formalism. Molecular Physics, 26(4), 905-927.

9   Cortona, P., Doniach, S., & Sommers, C. (1985). Relativistic extension of the spin-polarized local-density-functional theory: Study of the electronic and magnetic properties of the rare-earth ions. Physical Review A, 31(5), 2842

10   Rose, M. E., & Holladay, W. G. (1961). Relativistic electron theory

11   MacDonald, A. H., & Vosko, S. H. (1979). A relativistic density functional formalism. Journal of Physics C: Solid State Physics, 12(15), 2977.

12   Feder, R., Rosicky, F., & Ackermann, B. (1983). Relativistic multiple scattering theory of electrons by ferromagnets. Zeitschrift für Physik B Condensed Matter, 52(1), 31-36.

13   Strange, P., Staunton, J., & Gyorffy, B. L. (1984). Relativistic spin-polarised scattering theory-solution of the single-site problem. Journal of Physics C: Solid State Physics, 17(19), 3355.

14   Koenig, C. (1982). Self-consistent band structure of paramagnetic, ferromagnetic and antiferromagnetic ordered FeRh. Journal of Physics F: Metal Physics, 12(6), 1123..

15   Kotani, T. (1994). Exact exchange-potential band-structure calculations by the LMTO-ASA method: MgO and CaO. Physical Review B, 50(20), 14816.

16   Foresman, J. B., & Frisch, A. E. (2015). Exploring chemistry with electronic structure methods, 3rd edn. Wallingford, CT, USA: Gaussian.

17   Khireddine, A. (2022). Étude théorique des propriétés structurales et optiques des composés organométalliques (Doctoral dissertation).

18   Forster, A., & Visscher, L. (2021). GW100: A slater-type orbital perspective. Journal of chemical theory and computation, 17(8), 5080-5097

19   Zhu, W., & Trickey, S. B. (2017). Accurate and balanced anisotropic Gaussian type orbital basis sets for atoms in strong magnetic fields. The Journal of Chemical Physics, 147(24).

20   Genheden, S., Reymer, A., Saenz-Méndez, P., & Eriksson, L. A. (2017). Computational chemistry and molecular modelling basics.

21   Hehre, W. J. (1976). Ab initio molecular orbital theory. Accounts of Chemical Research, 9(11), 399-406.

22   Frisch, M. J., Pople, J. A., & Binkley, J. S. (1984). Self-consistent molecular orbital methods 25. Supplementary functions for Gaussian basis sets. The Journal of chemical physics, 80(7), 3265-3269.

23   Møller, C., & Plesset, M. S. (1934). Note on an approximation treatment for many-electron systems. Physical review, 46(7), 618.

24   Salahub, D. R., Castro, M., & Proynov, E. I. (1994). Density Functional Theory, Its Gaussian Implementation and Applications to Complex Systems. Relativistic and Electron Correlation Effects in Molecules and Solids, 411-445.

25   Delley, B. (1990). An all-electron numerical method for solving the local density functional for polyatomic molecules. The Journal of chemical physics, 92(1), 508-517.

Chapter 3
Exploring Divers Types of Materials

3.1   Introduction

The useful matter is the accurate description of materials as Christopher Hall defined it, where it covers a vast area of elements such as steel, concrete rubber, plastics, wood and others. Over time scientists understood the relationship between the structural elements of materials and their properties which led to a new branch known as Materials science that specialized in studying and creating materials with specific properties. This field is constantly developing, driven by the pursuit of unique and adaptable materials with enhanced performance that have diverse applications.[1]

Organic materials, derived from carbon-based compounds provide exceptional adaptability lightweight structures, and a flexible nature that exhibits a diverse range of properties to become essential components in everyday items, from packaging materials to electronic devices. At the same time, transition metals occupy an important position in the periodic table, carrying a variety of unique characteristics, such as excellent conductivity, magnetism and catalytic activity, their significance is illustrated through the general use in industrial processes, electrical devices, and catalysis. Combining these two components has produced a new category known as organo-metallic composites, this hybridization combined organic materials mechanical flexibility with transition metals exceptional characteristics.[2]

In this chapter, we will explore the properties and applications of these types of materials: organic, transition metals, and oregano-metallic along with the studied materials in this work

3.2   Transition Metals

Metals play a very important role in everyday life (Iron, Copper, Zinc, etc.), they occupy an important part of the periodic table, and widely used in manufacturing superconductors, the construction of alloys, etc. The electric, mechanic, and magnetic properties of these materials make them ideal for various applications such as fuel batteries and detectors.

Transition elements are those whose atomic state has a partially filled d subshell, for transition metals or f subshells for lanthanides, and actinides according to the l'IUPAC (International Union of Pure and Applied Chemistry) [3].

Transition metals are all metals that conduct electricity. They generally have high density, melting, and vaporization temperatures, except for those in Group 12, which have low melting

points like mercury liquid above -38.8°C, and Copernicium which may even be gaseous at room temperature [4].

This description refers to elements sharing a common set of properties, like all metals are good conductors of electricity, solid under normal temperature and pressure conditions, with a high density and melting temperature, they usually have remarkable catalytic properties in their atomic and ionic forms. Due to the low energy differences between their different oxidation states, these elements can form a wide variety of ionic species in a wide range of oxidation states, giving rise to variously colored complexes due to the different electronic transitions within the incomplete d subshells, they are also likely to form numerous paramagnetic compounds.

There are two types of transition metal:

- *Noble Metals*, whose first ionization energy is lower than that of hydrogen, this means they are difficult to oxidize and do not often react with other elements. In addition, they are often rare, and expensive like gold, silver, platinum, etc.
- *Non-noble Metals* are the opposite and their first ionization energy is higher than that of hydrogen. They oxidize in the open air more easily than noble metals like iron, copper, Nickel, etc.

The rule of Klechkowski explains the electronic configuration that progressively fills an electronic subshell following a saturated orbital group for most chemical elements; the remaining elements are found precisely among the transition metals. This classifies the transition metals in three series or elements, and these elements establish bonds via their valence electrons in the s and d orbitals.

Series 1	**Sc**	**Ti**	**V**	**Cr**	**Mn**	**Fe**	**Co**	**Ni**	**Cu**	**Zn**	Z=21 to 30
Series 2	**Y**	**Zr**	**Nb**	**Mo**	**Tc**	**Ru**	**Rh**	**Pd**	**Ag**	**Cd**	Z=39 to 48
Series 3	**Lu**	**Hf**	**Ta**	**W**	**Re**	**Os**	**Ir**	**Pt**	**Au**	**Hg**	Z=57, 72 to 80

3.2.1   Electronic Properties

Transition elements can be defined as elements with an unfulfilled *d* layer in one of their oxidation states. There are 5*d* orbitals, so 10 elements per row (3*d*, 4*d*, 5*d*). The electronic configuration of the ground state is shown in the three tables below, for each transition element, as well as the oxidation degree that refers to the loss (+) or the gain (-) of electrons according to the associated number.

3.2.1.1 *3d* Elements

Elements	Symbol and Atomic Number	Electronic configuration	Oxidation Degree
Scandium	Sc 21	[Ar] $3d^1 4s^2$	+3
Titanium	Ti 22	[Ar] $3d^2\ 4s^2$	+2, +3, +4
Vanadium	V 23	[Ar] $3d^3\ 4s^2$	+2, +3, +4, +5
Chromium	Cr 24	[Ar] $3d^5\ 4s^1$	From +2 to +6
Magnesium	Mn 25	[Ar] $3d^5\ 4s^2$	From +2 to +7
Iron	Fe 26	[Ar] $3d^6\ 4s^2$	From +2 to +6
Cobalt	Co 27	[Ar] $3d^7\ 4s^2$	+2, +3, +4, +5
Nickel	Ni 28	[Ar] $3d^8\ 4s^2$	+2, +3, +4
Copper	Cu 29	[Ar] $3d^{10}\ 4s^1$	+2, +3
Zinc	Zn 30	[Ar] $3d^{10}\ 4s^2$	+2

3.2.1.2   4d Elements

Elements	Symbol & Atomic Number	Electronic configuration	Oxidation Degree
Yttrium	Y 39	[kr] $4d^1 5s^2$	+3
Zirconium	Zr 40	[kr] $4d^2\ 5s^2$	+2, +3, +4
Niobium	Nb 41	[kr] $4d^4\ 5s^1$	+2, +3, +4, +5
Molybdenum	Mo 42	[kr] $4d^5\ 5s^1$	+2, +3, +4, +5, +6
Technetium	Tc 43	[kr] $4d^5\ 5s^2$	From +2 to +7
Ruthenium	Ru 44	[kr] $4d^7\ 5s^1$	From +2 to +8
Rhodium	Rh 45	[kr] $4d^8\ 5s^1$	+2, +3, +4, +5, +6
Palladium	Pd 46	[kr] $4d^{10}$	0, +2, +4
Silver	Ag 47	[kr] $4d^{10}\ 5s^1$	+2, +3
Cadmium	Cd 48	[kr] $4d^{10}\ 5s^2$	+2

3.2.1.3   5d Elements

Elements	Symbol & Atomic Number	Electronic configuration	Oxidation Degree
Lanthanum	La 57	[Xe] $5d^1 6s^2$	+3
Hafnium	Hf 72	[Xe] $5d^2\ 6s^2$	+2, +3, +4
Tantalum	Ta 73	[Xe] $5d^3\ 6s^2$	+2, +3, +4, +5
Tungsten	W 74	[Xe] $5d^4\ 6s^2$	+2, +3, +4, +5, +6
Rhenium	Re 75	[Xe] $5d^5\ 6s^2$	From +2 to +7
Osmium	Os 76	[Xe] $5d^6\ 5s^2$	From +2 to +8
Iridium	Ir 77	[Xe] $5d^7\ 6s^2$	+2, +3, +4, +5, +6

Platinum	Pt	78	[Xe] $5d^9$ $6s^1$	0, +2, +4, +5, +6
Gold	Au	79	[Xe] $5d^{10}$ $6s^1$	+2, +3, +5
Mercury	Hg	80	[Xe] $5d^{10}$ $6s^2$	+1, +2

In bulk environments and in specific cases, metals behave strangely in the electronic filling order where electrons from the s orbitals move to the d orbital and that is Because the 3d and 4s (or 4d and 5s) orbitals are almost in the same energy level, and it is interpreted as a stabilization process for the molecules for example, the most common electronic configurations are $3d^n4s^2$, $4d^n5s^2$, and $5d^n6s^2$, but stabilized configurations by exchange interaction (the ground state is the maximum spin state) occur for chromium by $3d^54s^1$, copper $3d^{10}4s^1$, and gold $5d^{10}6s^1$. This is often translated as a half-filled or fully-filled energy level with high stability. But there are many more "exceptions" in $5s^1$ in the second line. In general, d orbitals are accessible and contribute to the establishment of "coordination bonds", ligand energy field is extremely important for the reactivity and properties of transition elements. The right quantum numbers to describe the ground state of transition elements are L and S, however the spin-orbit coupling increases with Z [5].
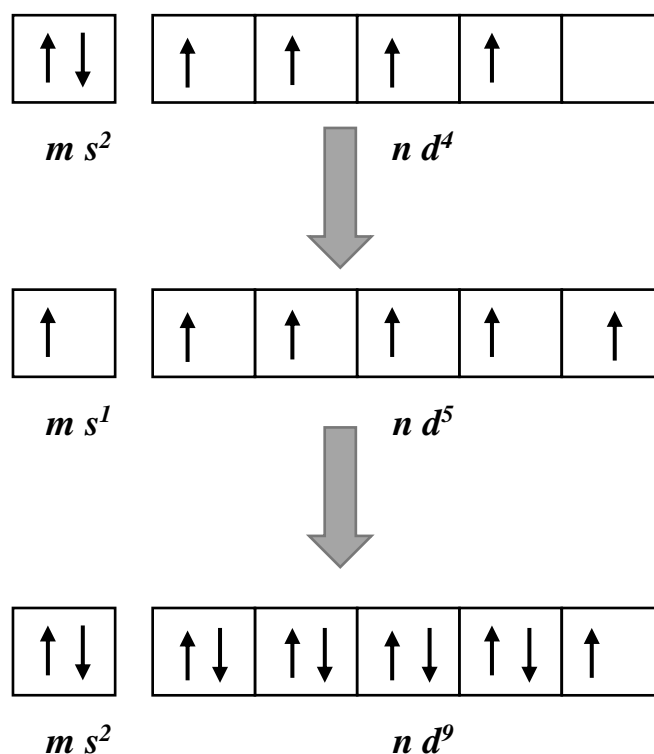
And

In most common situations metals are linked to each other with metallic bonds through valence electrons, which travel around ionic atoms in an "electronic cloud" as defined by the free electron model. There are several theories to explain this behavior, the most important is band theory, that explains certain behaviors in metal conductivity. Atoms tends to form bonds with each other, creating molecular orbitals, these bonds are all the same, but they must have different energies, in this way an infinite number of molecular orbitals with similar energies are formed. On the energy diagram, we notice a progression of closely spaced energy levels in the form of a band, this indicates that only a small amount of energy is required to move electrons from one orbital to another, ensuring good electric and heat conductivity. Bands can overlap and the energy levels between these bands is not uniformly separated, in other words, the number of energy levels in a band region is high at the center and decreases to the edges of the band, while it is null between the bands.

Other complexes that are formed using transition metals along with other types of molecules (ligands) form what is known as coordination complexes through electronic exchange between them creating coordination bonds, based on the nature of these bonds, ligands can be classified into three types. The X-type ligands donate one electron to the metal and take another to form a covalent bond changing the valence electron number of the metal by one. There are mono-functional X ligands such as hydrogen and halogens, the L-type ligands that have an even number of electrons and donate two electrons at a time to the metal. Finally, the Z-type ligands represented by acids that accept the donation of a pair of metal electrons modifying the valence number with two units.[6].

3.2.2 Physical Properties

The structure of all transition metals is a highly coordinated structure like compact hexagonal (CH), face-centered cubic (FCC), or center cubic (CC). Metal atoms tend to behave like tiny marbles, stacked as densely as possible. C.F.C and C.H have a maximum compacity of 74%, however, in some cases, the metal bond exhibits a certain directionality and atoms stack up in a more open structure the C.C with a compacity of 68%, which ensures a tremendous hardness (+9 on the Mohs scale). Their dense structure gives transition metals additional properties, such as electrical conductivity, with metals being good conductors and some becoming superconductors at very low temperatures (generating high magnetic fields) and the melting temperature that is the highest compared to other types of materials (T_F=3400 C°). Melting temperature is related to the bonding force of atoms (metallic bonds), and for transition

metals most partially filled "d" orbitals, in the same class of the periodic table, atomic radi decrease as atomic number increases, this is because the orbitals are increasingly filled with electrons, and therefore closer to the nucleus which requires a high energy to separate those atoms [7].
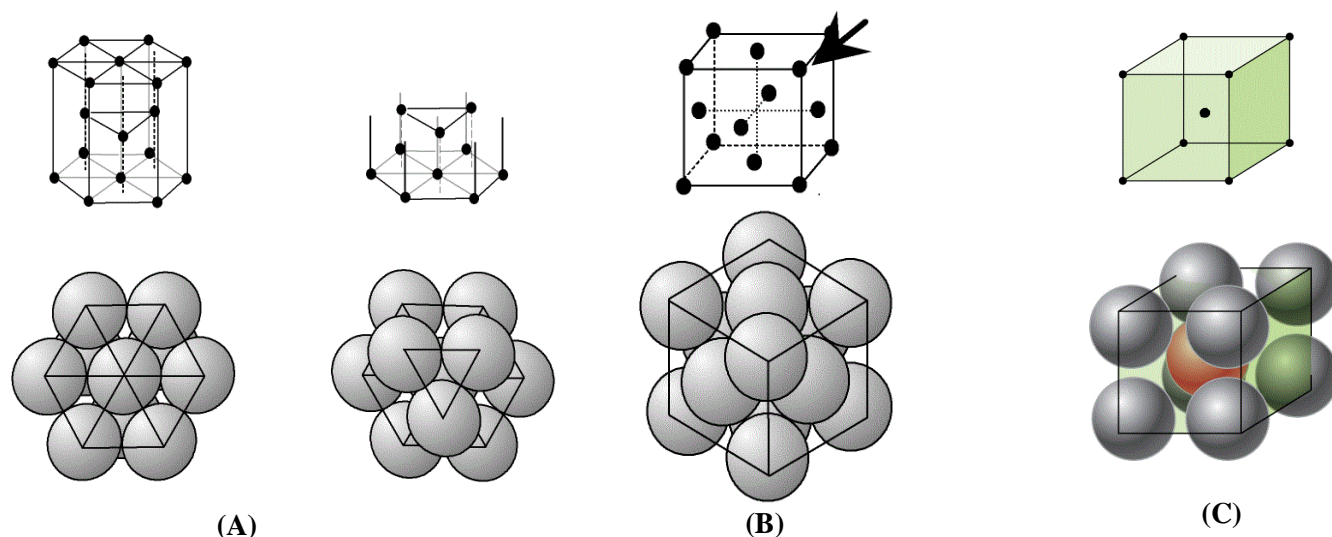

<div align="center">(A)   (B)   (C)</div>

Figure III.1 Different dense crystallographic structures (A) compact hexagonal C.H., (B) face-centered cubic FCC, (C) centered cubic CC.

3.3   Organic Compounds

This term refers to substances found in living organisms and involves molecules containing carbon atoms, which have the ability to form up to four strong bonds with other elements or other carbon atoms, to form a long chain or rings or an enormous variety of compounds from the simple methane that contains one carbon atom to incredible complexes with hundreds of carbon atoms, lately modern chemistry could create and develop new organic compounds that are not from living organisms such as medicines dyes polymers, etc. [8].

Organic compounds can be classified into two categories: polymers which are macro-molecules formed by the repetition of a basic component named the monomer in a process called polymerization, it can be natural like DNA, and proteins, or manufactured like plastics or polyester. The second category is molecular materials that are formed by individual molecules, and can be classified into different subgroups based on their functional groups and structures, like hydrocarbons that only formed by carbon and hydrogen, alcohols that contain hydroxyl

group (OH), ketones and aldehydes that have a carbonyl group (CO), carboxylic acids that include a carboxyl group (COOH) and amines that contain Nitrogen bonded to carbon atoms [8].

Organic compounds are characterized by their low melting temperature and weak density due to their fragile type of bonds, the high reactivity rate as a result of the diverse functional groups that allow them to participate in various chemical reactions, solubility in organic solvents such as alcohol or benzene and a good insulator [8]

3.3.1   Organic Compounds Properties

The electronic configuration of carbon (C) is $He[2s^2\, 2p^2]$, means that only two of the four valance electrons in the *p* orbital can form chemical bonds based on Klechkowski's rule, however experience confirmed the carbon's ability to form up to four bonds and, in most cases a covalent bond is formed by the overlapping of two atomic orbitals, which resulting in a shared pair of electrons that are attracted to the nuclei of both atoms forming the bond according to the valence bond theory and molecular orbital theory. There are two types of covalent bonds depending on the orbital that overlapped, the Sigma (σ) bonds that are formed when the s orbitals of two atoms overlap, while the Pi (π) bonds are formed when the p orbitals of two atoms overlap.

Bond hybridization proposes that an electron from the *s* orbital could be shifted to the empty *p* orbital box forming four single valance electrons, the number of *p* orbitals involved in the hybridization process, helps define the hybrid orbitals formed and the properties of the studied molecule. There are three common types of hybridization *sp, sp^2*, and *sp^3* and each type corresponds to a specific molecular geometry [9].
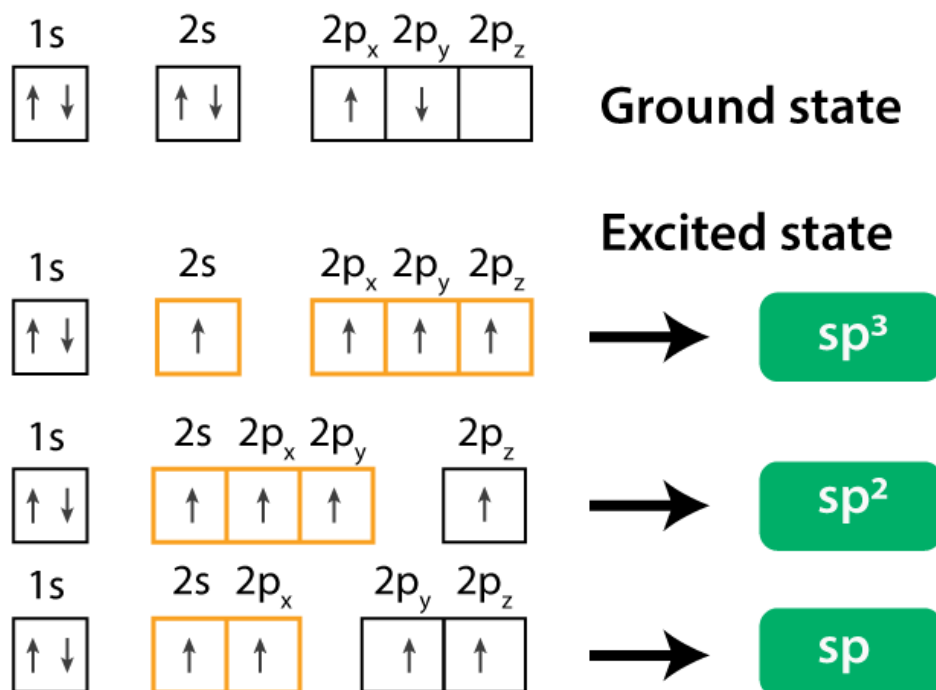
Figure III.2 Hybridization types of valance orbitals in a carbon atom.

The *sp* establishes triple short bonds an *sp* **σ** bond along with two **π** bonds sharing six electrons as it is shown in figure III.3:
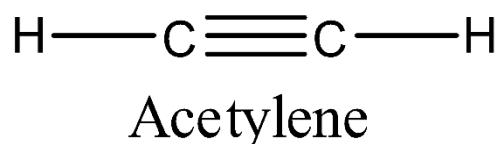

Figure III.3 acetylene molecule

sp² creates **σ** bonds using three electrons while the fourth non-hybridized electron is used to create a delocalized **π** bond as it is presented in Figure III.4
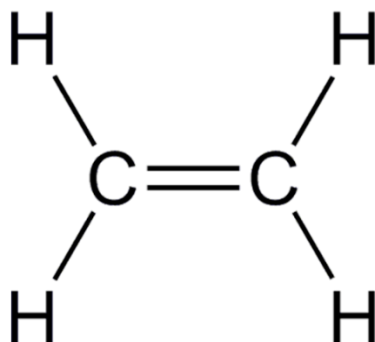

Figure III.4 Ethylene molecule

sp^3 form an equal number of σ bonds to form a tetrahedral structure as it is shown in Figure III.5
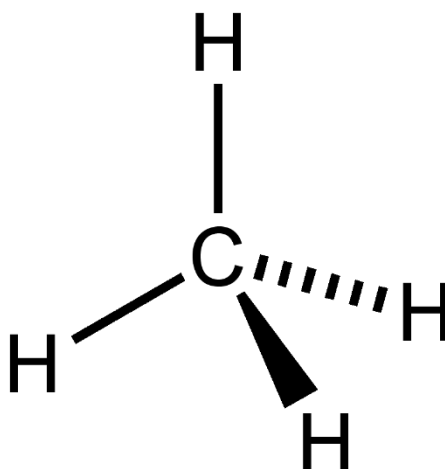

Figure III.5 Methane molecule

Organic molecules often have polar covalent bonds, as a result of unsymmetrical electron sharing caused by differences in the electronegativity of atoms, this polarity is measured by its dipole moment, **μ**, this electron (charge) distribution or polarity in a molecule could be represented visually through an electrostatic potential map that uses a color system to indicate the electron-rich and electron-poor regions in a molecule

The delocalized **π**-electron system is the characteristic that gives organic compound its conductivity which allows the transport of electrons between atoms through the overlapping of the p_z wave functions with those of neighboring atoms, in what is known as the resonance. For example the benzene molecule could be represented in several ways as shown in Figure III.6
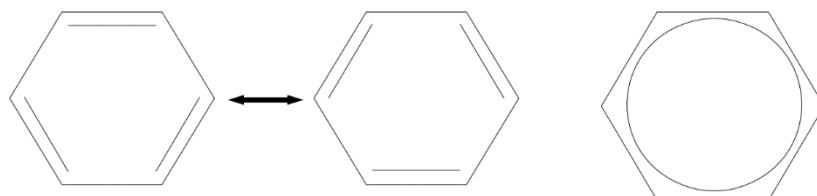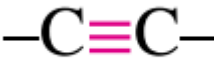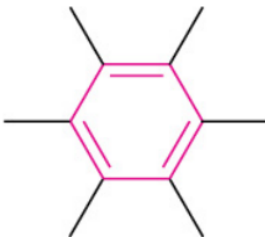
Figure III.6 Different ways of drawing the benzene structure

The benzene molecule varies between two stable structures changing the position of the single and the double bonds that are resumed by a circle to illustrate schematically the delocalization of electrons in the molecule.

3.3.2   Classification of Organic Compounds

Chemical Abstracts, a journal that classifies and indexes the chemical literature, reports about 195 million recognized organic molecules, where each molecule has unique physical characteristics such as melting and boiling points, as well as unique chemical reactions. Scientists introduced a method to organize all those molecules in a way that facilitates its study, through a classification of organic molecules into families based on their structural features, to make it a couple of organic chemical families that have similar chemical behavior, that is known as functional groups. **Table III.1** gives an example of some common function groups.

Name	Structure
Alkene (double bond)	
Alkyne (triple bond)	$-C\equiv C-$
Arene (aromatic ring)	
Halide	 (X=F, Cl, Br, I)
Alcohol	
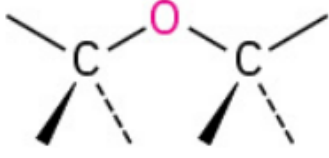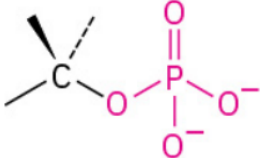
Ether	
Monophosphate	

Table III.1 Structure of Some Common Functional Groups

3.4 Chalcone

Chalcones are organic natural or synthetic compounds belonging to the bicyclic flavonoid family, were named by scientists Kostanecki and Tambor in 1899, it is found in plants such as angelica, Glycyrrhiza, Humulus, and Scutellaria. Recent studies have concentrated on it potential biological activity and capacity, to function as intermediates in the production of various heterocyclic systems, the structural skeleton of chalcones, particularly 1,3-diarylprop-2-en-1-ones, consists of two aromatic rings joined by an open chain of three-carbon unit, with an unsaturated carbonyl system [10,11], it is a flexible molecule that could be found in two different structures Z(cis) and E(trans) as it is presented in Figure III.7, however, this last one is a more stable thermodynamically and require the lowest energy of formation, while the carbonyl group and B-ring exhibit substantial steric effects, making the compound unstable.

There are several processes involved in synthesizing chalcone by condensation, the first step involves removing a proton (deprotonation1) from the α-carbon of acetophenone, which creates an enolate ion, the enolate functions as a nucleophile, attacking the carbonyl group of aromatic aldehydes to produce alkoxide anion, that takes a proton from water, resulting in β-hydroxy ketone, this last deprotonates the α-carbon of the β-hydroxy ketone, creating another alkoxide connected to an alkene. Finally, a dehydration process occurs (Deprotonation 2 and Elimination) **Figure III.8** resumes these steps.[11]

(*E*)-isomer   **(*Z*)-isomer**
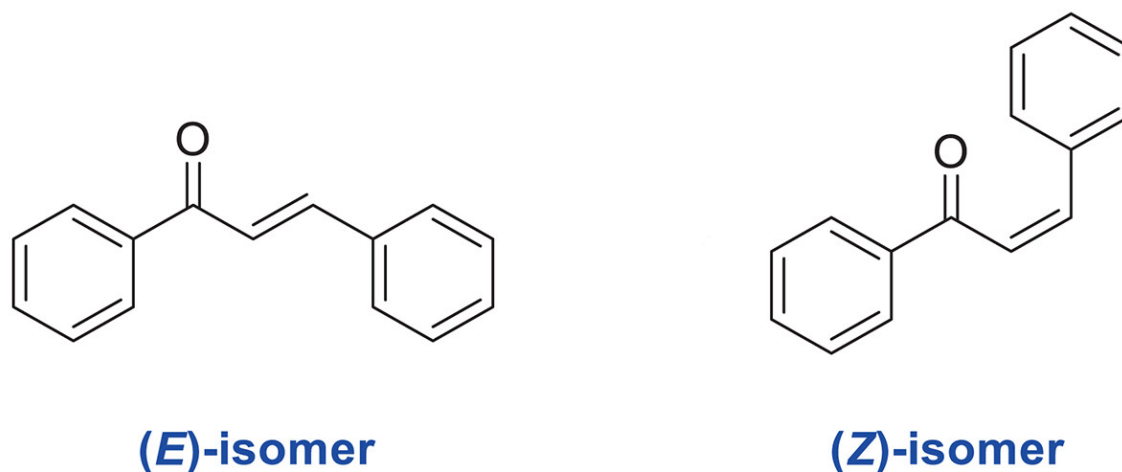
Figure III.7: the two chemical structures of chalcone
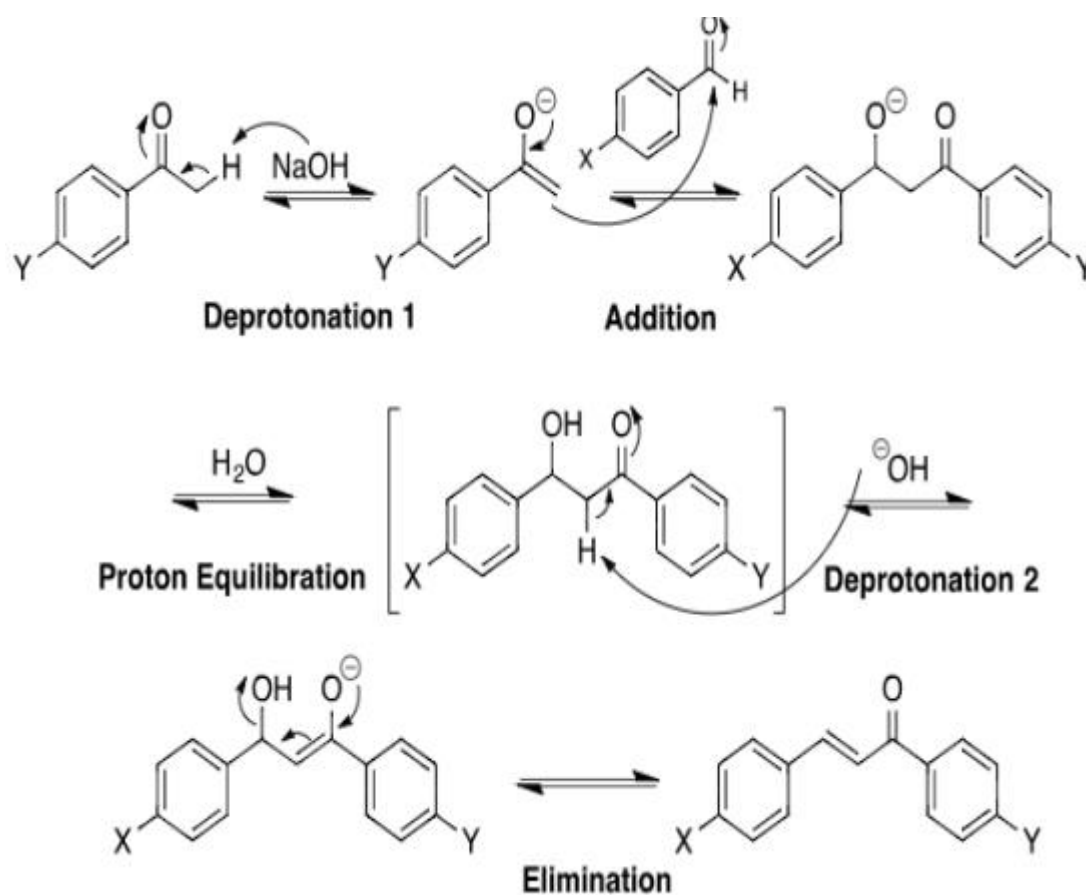
Figure III.8 Chalcone synthesis mechanism via aldol condensation with a base catalyst

3.5   Organometallic Compounds

Organometallic compounds bridge the fields of organic chemistry and inorganic chemistry, as they exhibit the characteristics of both types. These compounds are those elements that are formed by metal atoms connected to an organic material, in which the central metal atoms are directly bonded to an organic group or molecule through a Metal-Carbone bond, that could be ionic or covalent bound delocalizes between the organic groups and a metal atom, which gives it a rich variety of coordination modes, including σ and π bonds formed by the organic ligands that ensure the material reactivity, on the other hand the metallic atom provide the material with remarcable stability against high temperatures, strong acids or bases, along with magnetic properties. These properties made the organometallic compounds exceptional catalysts and gave it the ability to be applied in various fields in chemistry and medicine [12].

Organometallic compounds are divided into different types, and the simple ones are those with a metal-carbon bond that is typically similar regarding the compound derivative, they could be classified into symmetrical compounds, where the metal atom is surrounded by similar function groups or atoms, like [Hg $(C_2H_5)_2$] Diethylmercury as presented in Figure III.9, and asymmetrical like the ethyl mercury as presented in Figure III.10
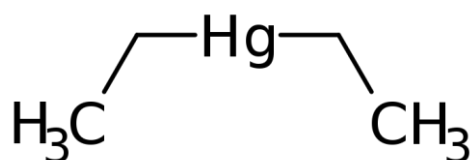
Figure III.9 Diethylmercury molecule
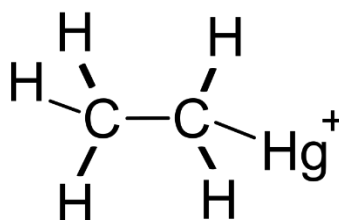
Figure III.10 Ethyl mercury molecule

The second type is the mixed organometallic compounds, where the metal atom is bounded to more than one organic or inorganic constituent, like 2 different metallic atoms connected to one organic functional group, like Ethyl magnesium bromide as shown in Figure III.10
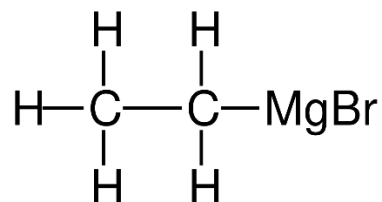
Figure III.11 Ethyl mercury molecule

On this basis organometallic compounds are classified according to the type of metal-carbon bond, into Ionic-bonded organometallic compounds including the alkali metals, alkaline earth metals, lanthanides, and actinides mainly form ionic compounds, these are generally colorless compounds that are highly reactive, solid, non-volatile and insoluble in organic solvents. For example: $Ph_3C^-Na^+$, Cp_2Ca, Cs^+Me^-, Na^+Cp^-.[12]

The second is covalently bonded organometallic compounds, which in turn are classified into σ bonded organometallic compounds, where the organic ligand's carbon atom forms a two-electron covalent connection with the metal shared between two atomic centers. Most elements have electronegativity values greater than one. Like the $Ni(CO_4)$ as presented in Figure III.12 and the π bonded organometallic compounds where alkenes, alkynes, and other carbon groups have electrons in π-orbitals, when these orbitals overlap with the unoccupied orbitals of the metal atoms, this last gets bounded to many carbon atoms rather than just one as shown in Figure III.13
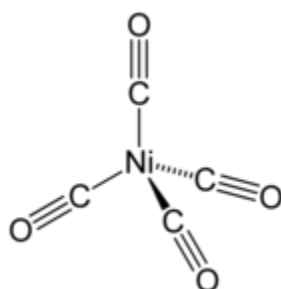
Figure III.12 Tetra carbonyl nickel molecule
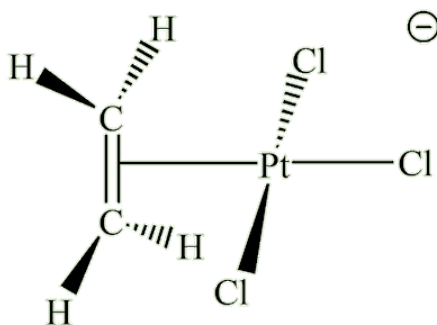
Figure III.13 Zeise's salt molecule

3.6   Conclusion

In conclusion, we explored the diverse types of materials that cover transition metals, organic compounds, and organometallic derivatives, and now it evident that knowing their complicated connections and exploiting their interaction, creates a chances for innovation that serves as the foundation and the aspiration for our research, offering insights into designing advanced materials with tailored properties for applications in fields such as medicine, energy, and materials engineering.

3.7   References

1   Hall, C. (2014). Materials: a very short introduction (Vol. 405). Oxford University Press, USA.

2   Callister Jr, W. D., & Rethwisch, D. G. (2020). Fundamentals of materials science and engineering: an integrated approach. John Wiley & Sons.

3   Book, G. (2014). Compendium of chemical terminology. International Union of Pure and Applied Chemistry, 528.

4   Slater, J. C. (1963). Quantum Theory of Molecules and Solids: Insulators, semiconductors, and metals (Vol. 3). McGraw-Hill.

5   Amarouche, T. (2012). Proprietés maggnétiques et électroniques spintronique des matériaux magnétiques (Doctoral dissertation, Tizi Ouzou).

6   Boukelkoul, M. (2018). Propriétés magnéto-optiques des couches ultraminces et des slabs à base de métaux de transition (Doctoral dissertation).

7   Houcher, A. (2022). Etude des propriétés structurales et magnéto-optiques des films ultraminces déposés par épitaxie pseudomorphique (Doctoral dissertation).

8   McMurry, J. (2016). Organic chemistry. Cengage Learning.

9   Stella, M. (2010). Study of organic semiconductors for device applications. Universitat de Barcelona.

10   Al Hammouri, S. (2019). Synthesis and Biological Evaluation of Chalcones, Isoxazole and Pyrazole Derivatives Attached with Adamantyl Substituent.

11   Chang, K. L. (2015). The Complete Mechanism of Chalcone Formation. University of California, San Diego.

12   Khireddine, A. (2022). Étude théorique des propriétés structurales et optiques des composés organométalliques (Doctoral dissertation)

Chapter 4

Comprehensive Properties of Materials

4.1 Introduction

Material properties play a crucial role in classifying and determining their applications and elements selections, it is an essential aspect that defines the behavior and characteristics of different substances, it also represents unique features for each element. On the other hand, the materials science is developing based on understanding how various materials behave, this information is essential for building new technologies and enhancing existing ones for a variety of industries. To maximize the potential of a material, scientists must first understand its internal structure, which represents one of the most essential aspects that researchers study, including magnetism, how magnetism impacts light (magneto-optics), and how light interacts with the material in a non-linear fashion. These features are not only intriguing to investigate but also necessary for developing real-world applications.

Material characteristics serve as a basis for creating and developing materials to satisfy specific requirements, the study of structural characteristics gives insights into the arrangement of atoms and molecules inside the material, laying the groundwork for predicting its mechanical, thermal, and electrical properties. Meanwhile, magnetic characteristics reveal the interesting realm of materials that respond to external magnetic fields, revealing potential in data storage, sensing, and energy conversion, on the other hand magneto-optical properties, lies at the interface of magnetism and optics, adding an interesting new dimension to materials study. Understanding how materials interact with light in the presence of magnetic fields has enabled new applications in information technology and telecommunications, furthermore, the study of nonlinear optical characteristics exposes the ability of materials to respond to intense light, opening the way for advances in laser technology, optical signal processing, and imaging.

This chapter seeks to explore the most important properties used in this work by understanding the complexity of structural arrangements, magnetic responses, and optical behaviors.

4.2 Magnetic Properties

The history of magnetism began a long time ago with a certain material called magnetite "magnet stone". at that time, the only way to observe magnetic phenomena was to make magnetite magnets, until the invention of the first electromagnet. In 1825, Hans Christian Oersted observed

that a magnetic needle was deflected by an electric current passing through a conducting wire, this discovery, which links electricity and magnetism, was the basis of the electromagnetism theory. With the birth of quantum mechanics in the 1920s, physicists were able to show theoretically and experimentally that the electron behaves like a tiny magnet, it exhibits what is known as a "magnetic moment" or "spin", which is traditionally represented by an arrow indicating the orientation of this magnetic field [1].

In the 1970s, Albert Fert studied the way electrons move, and diffuses in a magnetized layer according to the orientation of their own "magnetization" or spin, he showed that the resistance encountered by an electron crossing a magnetized layer depends on the direction of its spin, relative to that of the layer's magnetization, the electrons of an electric current passing through a magnetized layer can be divided into two parts, magnetized layer: those whose spin is in the same direction as the magnetization of the layer, or "parallel spin", and those whose magnetization is in the opposite direction, or "antiparallel spin". Hence, we therefore observe two independent electrical currents flowing through the magnetic layer [1].

Magnetic materials are highly important in technology, their application generally appears in devices for power generation, information, telecommunications, data reading, and storage, as well as applications and information carriers, i.e. audio and video recording [1].

4.2.1 Magnetism in Materials

Faraday proved that any substance is magnetizable, but the effect is only appreciable in an intense magnetic field, by placing metal bars of different substances in a non-uniform magnetic field, some are attracted to regions of intense field, orienting themselves parallel to the field lines as a soft iron bar would, others are repelled towards regions where the magnetic field is weak, and orient themselves perpendicular to the field lines like silver or gold and they are known as diamagnetic elements. Substances that are comparable to iron are called ferromagnetic (iron, cobalt, nickel, and a large number of their alloys, especially steels), and some of their compounds, as well as certain combinations of non-ferromagnetic elements, substances that experience actions of the same nature as iron, but much less intense are called paramagnetic elements (aluminum, chromium, platinum... and certain compounds of ferromagnetic elements (e.g. 68% iron 32% nickel alloy).

In general, when a solid is immersed in a magnetic field, it has no noticeable effect on the structure of the solid or properties, except for a few magnetic substances, for which the magnetic field in the nearby sample can be multiplied by a factor of a hundred or even a thousand, each of the atoms in this solid that are in contact with a magnetic field, behaves like a small magnet characterized by a magnetic moment, which is of electronic origin [2].

4.2.1.1 Mono-electronic Atom Magnetic Moment

In classical electromagnetism, a magnetic dipole is associated with a circlar conductor of surface S in which a current of intensity i flows, and the magnetic moment is

$$\vec{\mu} = i\,\vec{S}$$

with

$$\vec{S} = S.\vec{n}$$
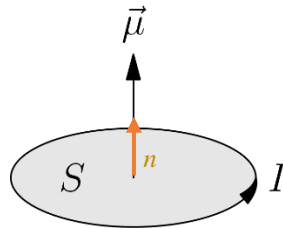
Figure IV.1 Simple Representation of a Magnetic Moment generation

The advantage of this description is that it remains correct in the quantum theory of magnetism, indeed, a magnetic dipole can be associated with an orbital-type current, due to the rotation of an electron around the nucleus of the atom to which it belongs (Figure IV.2)
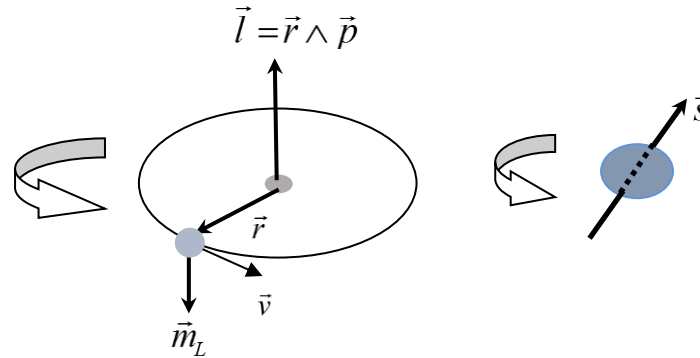
Figure IV.2 victor description of the Orbital angular momentum $\vec{l}$, orbital magnetic moment $\overrightarrow{m_L}$ and spin angular momentum $\vec{s}$ for a single-electron atom

Let's consider an electron, of mass m_e, describing a circular motion of radius r. the orbital magnetic moment of the electron $\overrightarrow{m_L}$ is proportional to its angular momentum $\vec{l}$ by:

$$\overrightarrow{m_L} = -\frac{g_L \mu_B}{\hbar} \vec{l} \tag{4.1}$$

g_L is the Landé factor ($g_L = 1$), $\mu_B = \frac{|e|}{2m_e}\hbar = 9.27 \times 10^{-24} Am^2$ Bohr's magneton and $\hbar$ is Planck's constant. But there is also a magnetic spin moment for certain particles (electrons, neutrons, protons, etc.), which is an essential quantum property, a particle of this type behaves like a tiny magnetic moment, which cannot be associated to a current, nevertheless, we can imagine that this magnetic moment is linked to the rotation of the particle around it self, although this image is incorrect.

The spin magnetic moment of the electron $\overrightarrow{m_s}$ is proportional to its spin angular momentum $\vec{s}$.

$$\overrightarrow{m_s} = -\frac{g_s \mu_B}{\hbar} \vec{S} \tag{4.2}$$

$g_s = 2$

The total contribution of an electron to the magnetic moment of an atom $\overrightarrow{m_J}$ is the sum of two effects: that of its orbital moment and that of its spin therefore the magnetization of an area is the result of the orbital magnetic moments and electron spin contribution.

$$\vec{m_j} = \vec{m_l} + \vec{m_s} = -(\vec{l} + 2\vec{s})\mu_B \tag{4.3}$$

4.2.1.2 Poly-electronic atom Magnetic Moment

The resultant angular momentum of a poly-electron atom is obtained by combining the orbital, spin angular orbital, and spin angular momentum of the individual electrons, we apply the method of *LS* coupling, or Russel-Saunders coupling, which assumes that the coupling of orbital movement with its spin is weak, and that, the individual orbital moments of the electrons $\vec{l_1}, \vec{l_2}, \vec{l_3}$ … interact strongly, leading to the total orbital moment while the spin angular momentum $\vec{s_1}, \vec{s_2}, \vec{s_3}$ interacts strongly to produce a resultant angular momentum.

$$\vec{L} = \sum_i \vec{l_i}$$

$$\vec{S} = \sum_i \vec{s_i} \tag{4.4}$$

The atom's total angular momentum is given by: $\vec{J} = \vec{L} + \vec{S}$

As for the magnetic moment resulting from the free atom, i.e. not affected either by external or internal, it is equal to the resultant of the orbital magnetic moment $-\vec{L}\mu_B$ and the spin magnetic moment $-\vec{S}\mu_B$. It is expressed in terms of the resulting angular momentum as:

$$\vec{M_J} = -g_L\vec{J}\mu_B = -(\vec{L} + 2\vec{S})\mu_B \tag{4.5}$$

the Landé factor associated with the atom is given by:

$$g_L = 1 + \frac{J(J+1) + S(S+1) - L(L+1)}{2J(J+1)} \tag{4.6}$$

the gyromagnetic coefficient γ is used to determine the relative importance of orbital and spin contributions to the magnetic moment of atoms in the substance under consideration

$$\gamma = \frac{\overrightarrow{M_J}}{\vec{L}} = -g_L \frac{e\hbar}{2m_e} \tag{4.7}$$

4.2.2 Magnetic Classification of Materials

Materials are classified into four types according to their behavior in the presence of a magnetic field, this reaction is measured by induction, which is the quantity of magnetic flux per unit area, the equation linking induction to the magnetic field is given below.

In vacuum, the magnetic induction field $\vec{B}$ and magnetic excitation field $\vec{H}$ vectors are collinear and linked by the relation $\vec{B} = \mu_0 \vec{H}$ Where μ_0 is the magnetic permittivity of vacuum ($\mu_0 = 4\pi . 10^{-7}$ T.m/A in IS)

In any isotropic magnetic medium, these vectors remain in line, however, the proportionality coefficient depends on the material. We define the magnetization vector $\vec{M}$, which indicates the influence of the environment, as the excitation field and magnetization overlap to express the induction field

$$\vec{B} = \mu_0 (\vec{H} + \vec{M}) \tag{4.8}$$

However, magnetization is proportional to the excitation field, which means:

$$\vec{M} = \chi_m \vec{H} \tag{4.9}$$

Where χ_m is the magnetic susceptibility of the material. the result is a new expression linking $\vec{B}$ and $\vec{H}$

$$\vec{B} = \mu_0 \vec{H} + \mu_0 \chi_m \vec{H} = \mu_0 (1 + \chi_m) \vec{H}$$

$$\vec{B} = \mu_r \mu_0 \vec{H} = \mu \vec{H} \tag{4.10}$$

With $\mu = \mu_r \mu_0 = (1 + \chi_m)\mu_0$

The application of an external magnetic field translates into a new energy term, that alters the material's primitive state of energy equilibrium to create a new configuration, certain domains are increased at the expense of their surrounding domains to the disadvantage of their nearest ones, due to wall displacements Figure IV.2. The application of an external magnetic field leads to equation (**4.9**) and can be either linear or non-linear Figure IV.3

Diamagnetism

Paramagnetisme

Ferromagnetisme

$\vec{H}$

At rest

Under an applied magnetic field
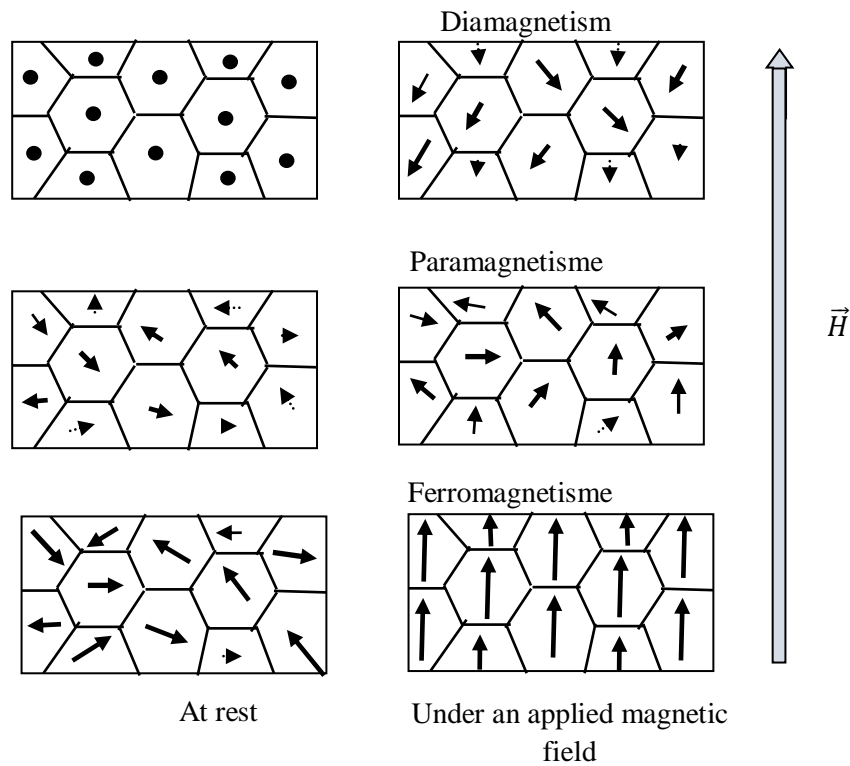
Figure IV.2 Orientation of magnetization at rest and under an external field

M

H and M in the same direction

Ferromagnetic

Ferrimagnetic

Paramagnetic

H

Diamagnetic

H and M in opposite directions
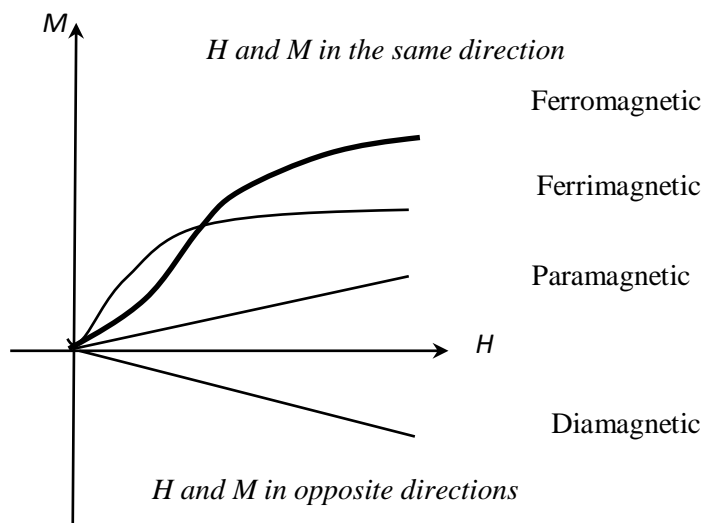
Figure IV.3 Evolution of the magnetization of the main magnetic materials in response to the application of an external field

Materials can be classified according to their magnetic behavior, i.e. their magnetic susceptibility χ_m, into four main types.

- Diamagnetic materials
- Paramagnetic materials
- Ferromagnetic materials
- Ferrimagnetic materials

Characteristic susceptibility values for these types of materials with some examples of representative materials are shown in Table IV.1

Type of material	Susceptibility magnetic	Examples
Diamagnetic	-1×10^{-5}	Cu, Au
Paramagnetic	10^{-5} to 10^{-3}	Al, Pt
Ferromagnetic	50 to 10000	Fe, Ni, Co
Ferrimagnetic	3000	FeO, MnO, ZnO

Table IV.1: Susceptibility values for different types of material

4.2.2.1 Diamagnetism

Diamagnetism is a fundamental (intrinsic) property of matter (a consequence of Lenz's law). but it is generally very weak, the origin of diamagnetism is the non-cooperative behavior of electrons when exposed to an applied magnetic field. Diamagnetic materials consist of atoms that do not have permanent magnetic moments (all the electron orbitals are filled and all the electrons

are paired). However, when the material is exposed to a magnetic field, an induced magnetization opposes the direction of the magnetic field, so the susceptibility is negative if we plot M=f (H) and the evolution of magnetic susceptibility as a function of temperature, diamagnetic materials are characterized by a negative susceptibility, which is independent of temperature, it is worth mentioning that when the field is zero, magnetization is null.

These materials are usually characterized by a relative magnetic permeability $\mu_r < 1$ and susceptibility values vary between 10^{-5} and 10^{-6}
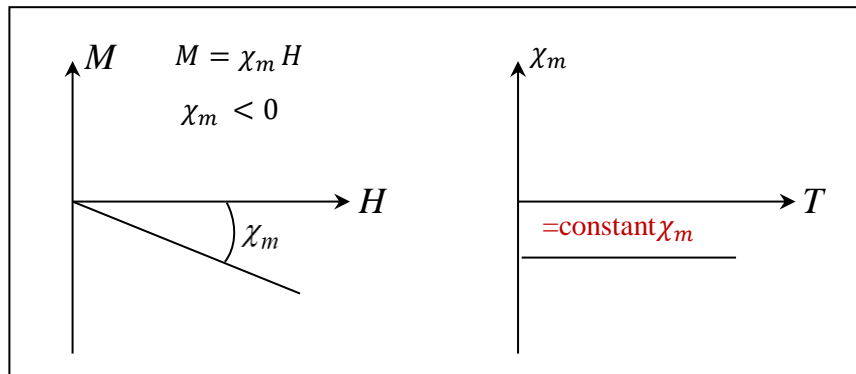
Figure IV.4 Magnetization M as a function of applied magnetic field H for a diamagnetic material and evolution of susceptibility as a function of temperature T

4.2.2.2 Paramagnetism

The paramagnetic material has free magnetic moments that do not interact with each other, and can be randomly oriented in any direction under the action of thermal energy, Figure IV-5(a) to achieve zero resultant magnetization, through the application of a magnetic field all the magnetic moments will align themselves with the direction of the field, thus magnetization is inversely proportional to temperature, Figure IV5(b) [1-3]. At absolute zero temperature, the susceptibility of magnetic materials is very high (positive) and decreases with temperature. Figure IV-5 (c) according to Curie law

$$\chi_m = \frac{C}{T} \tag{4.11}$$

Where (C) is the Curie constant given by the relation $C = \frac{N\mu^2}{k_b}$, N is the number of magnetic moments, μ is an individual magnetic moment, and k_b is Boltzmann's constant equal to 1.3807 x10^{-23}*J/K*. Paramagnetism is explained by Langevin using Curie's law: $M = C\frac{B}{T}$ where M is magnetization, B is induction (in Tesla) and T is absolute temperature (in Kelvins). Among paramagnetic materials, we find Tungsten, Magnesium Sodium, and Rhodium.
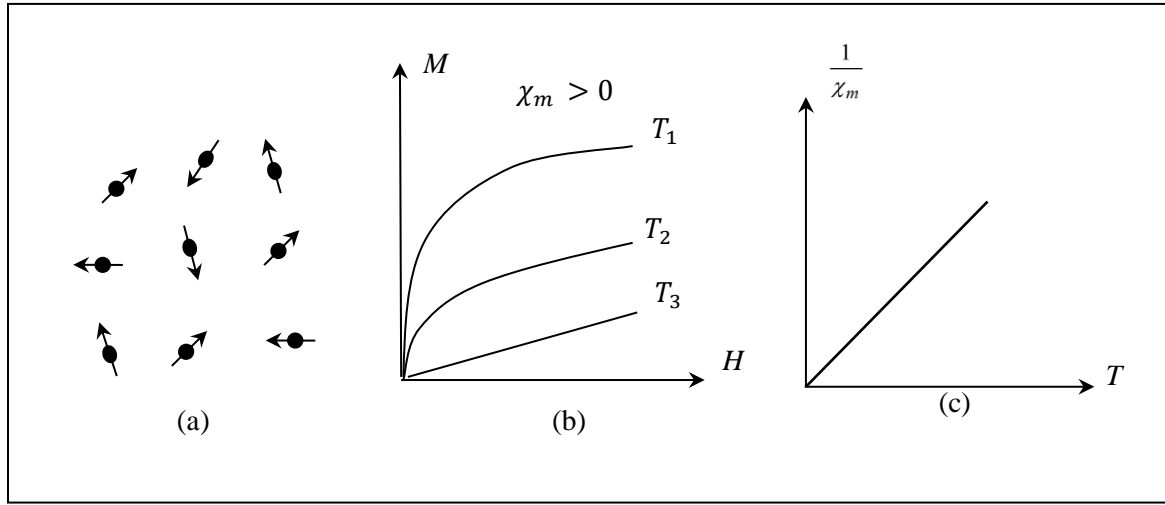
Figure IV.5: (a) Random orientation of magnetic moments in the absence of a magnetic field H (b) Magnetization curve of a paramagnetic body with temperature T as parameter (T1 < T2<T3). (c) The linear variation of the susceptibility inverse for a paramagnetic material as a function of temperature.

4.2.2.3 Ferromagnetism

In a ferromagnetic substance, interactions between neighboring atoms are referred to as positive exchange interactions, favoring the alignment of magnetic moments in localized regions called Weiss domains. In the absence of an external magnetic field, a spontaneous Ms magnetization occurs in each of these domains, which are randomly oriented so that the overall magnetization of the sample remains zero, applying an external field alters the distribution of domains, resulting in a variation in magnetization that is reflected in the first magnetization curve, when the material is magnetized for the first time. At the macroscopic level, a ferromagnetic

material is a substance that generally acquires a strong magnetization under the action of a field. Ferromagnetic materials include iron, cobalt, and nickel exhibit very high susceptibility at temperatures below their Curie temperature. However, at high temperatures, above the Curie temperature, susceptibility will be similar to that of a paramagnetic material due to thermal agitation; this is the Curie-Weiss law (Figure IV-6 (c)).
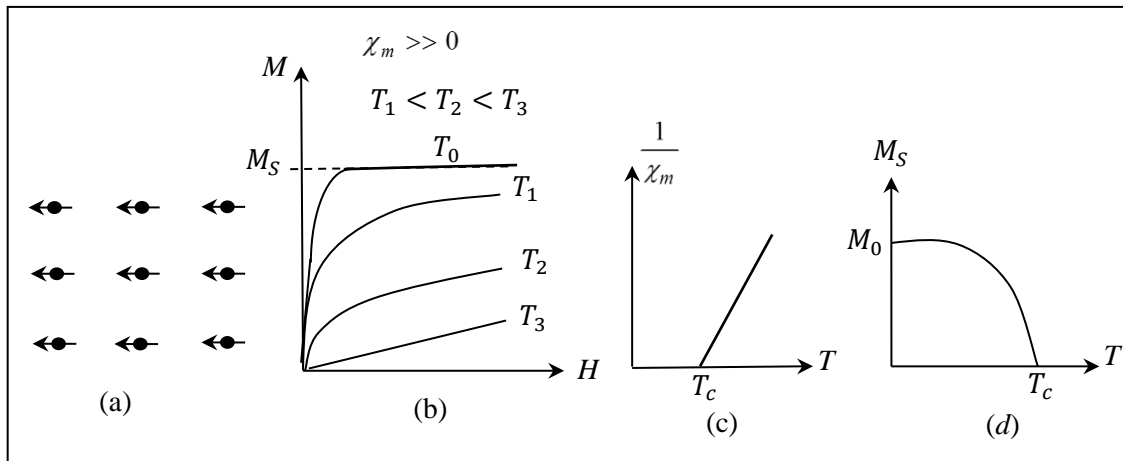
Figure IV-6: Ferromagnetism: (a) spin-lattice, (b) magnetization field variation with temperature, (c) thermal variation of inverse susceptibility, (d) thermal variation of spontaneous magnetization.

4.2.2.4 Ferrimagnetism

A ferrimagnetic material has two sub-lattices with different magnetizations, the spin moments of the atoms can be opposite and the resulting moment can be positive, or negative (Figure IV.7(a)). For ferrimagnetic substances, the magnetic moments are paralleled in opposite directions and with different intensities [1]. If the magnetic moments of a substance are antiparallel in a particular domain of the material and have different magnitudes, the total magnetic moment is not null, the substance is then called ferrimagnetic. There may be:

- An equal number of crystalline sub-lattices in opposite directions, but the magnetic alignment of one sub-unit may be stronger than the other. This is the case with magnetite, titan magnetite, and iron oxides or iron and titanium.

- The number of crystalline sub-lattices in one direction is greater than the number in the other direction.

The macroscopic properties of a ferrimagnetic material are similar to those of a ferromagnetic material. Figure IV-7 (b), (c). Among these ferrimagnetic materials, the ferrites exhibit very high resistivity in the range of 10^5 and 10^6 Ω.m, and it is used for microwave applications.
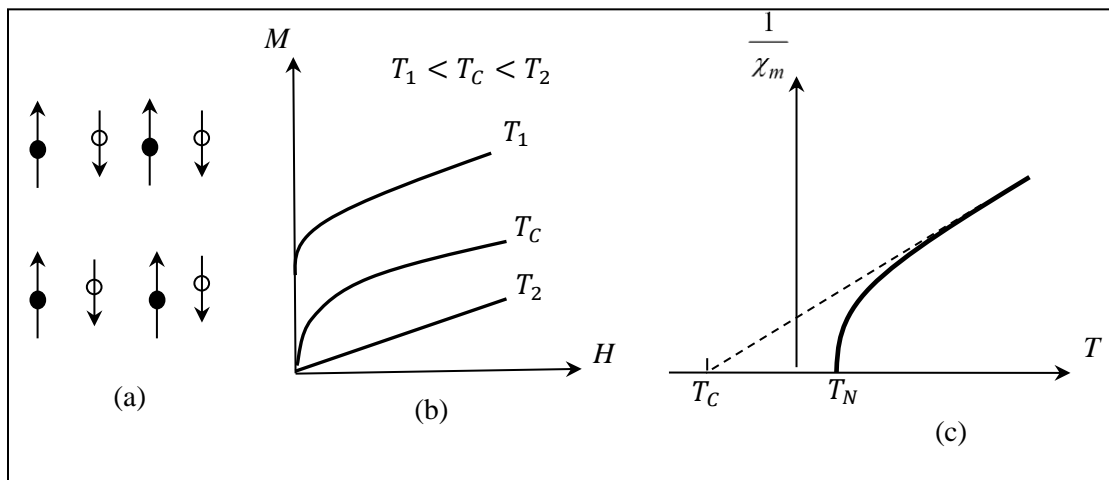
Figure IV-7 Ferrimagnetism: (a) spin-lattice, (b) variation under and external magnetization field, (c) thermal variation of susceptibility,

4.2.2.5 Antiferromagnetism

Antiferromagnetism was discovered by physicist Louis Néel in 1932, antiferromagnetic materials, have magnetic moments that interact with each other, but these substances generally consist of two magnetic lattices in which magnetic moments are coupled antiparallel [4]. The magnetizations of the two lattices compensate each other, thus these materials have no macroscopic magnetization. they also have zero remanences, and no hysteresis, but a weak, positive susceptibility that varies in a particular way with temperature, as illustrated in Figure IV.8.

In general, antiferromagnetism is the behavior of susceptibility below a critical temperature, the Néel temperature (T_N) [5]. and above it, susceptibility follows the Curie-Weiss law

$$\chi_m = \frac{C}{T_N + T_C} \tag{4.12}$$

where C is Curie's constant, T_N is Néel's temperature and T_C is Curie's temperature.

Manganese oxide MnO is an example of an antiferromagnetic ionic solid, in this material, each Mn^{2+} ion has a linear magnetic moment and O^{2-} has no moment, antiferromagnetism occurs at temperatures below the Néel temperature (T_N). Above this temperature, they become paramagnetic Figure IV.9.
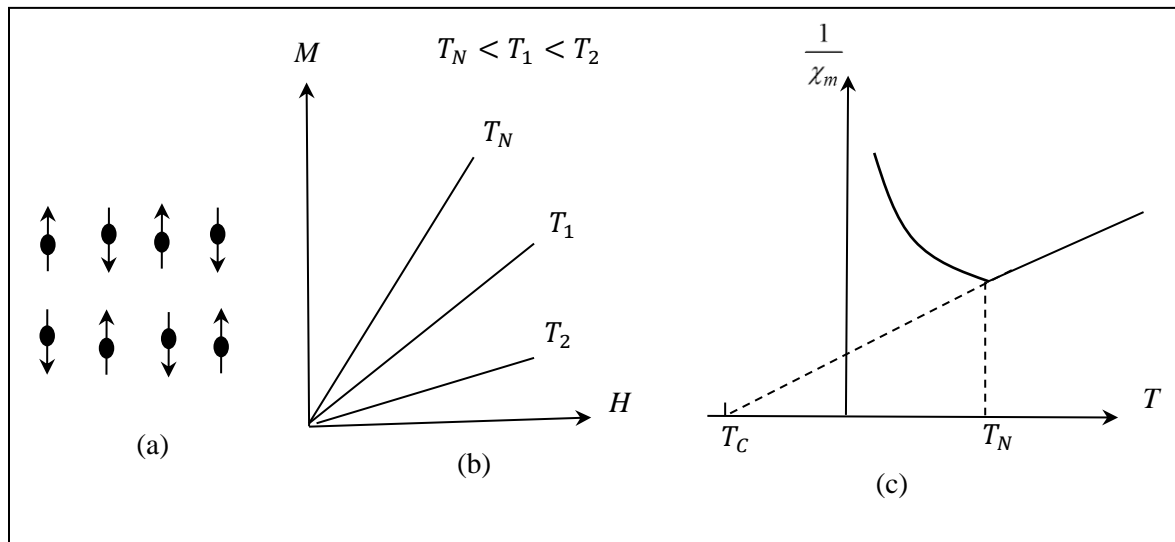
Figure IV.8. (a) Schematic representation of the two sub-lattices of an antiparallel-coupled antiferromagnetic material. (b) variation of magnetization as a function of temperature and (c) variation of $\frac{1}{\chi_m}$ as a function of temperature [5].
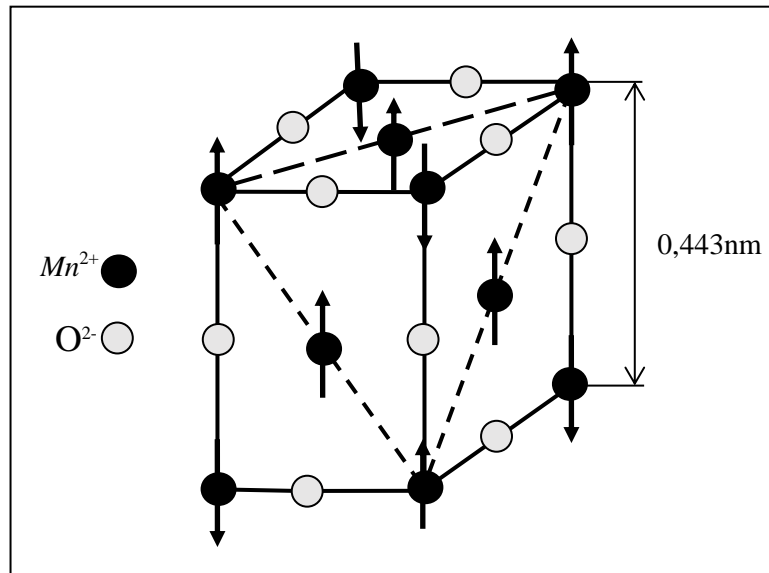
Figure IV-9: MnO Antiferromagnetic structure.

4.2.2.6 Hysteresis Cycle

The magnetization graph $M = f(H)$ or $B = f(H)$, also known as the magnetic hysteresis cycle, represents the response of a ferromagnetic material to an applied magnetic field H [1]. The hysteresis cycle can be used to define certain magnetic properties of the material, such as the remanent magnetization M_r, the saturation magnetization M_s, and the coercive field H_c Figure IV.10. The coercive field H_c is the field required to restore the remanence magnetization to zero; in other words, it is the field that must be applied to reverse the magnetization, when H_c is very low, materials are said to be soft; if H_c is sufficiently high, they are said to be hard [2]. The remanent magnetization M_r is the magnetization remaining once the applied magnetic field has been removed, it is the natural quantity expressing the fact that a ferromagnetic body can be spontaneously magnetized even in the absence of an external field. M_s saturation magnetization corresponds to magnetization where all magnetic moments are aligned, the area of a hysteresis

cycle gives us an average measure of the lost energy amount through heat to reverse the magnetization of a ferromagnetic material [1].

Magnetization of Saturation Ms: is the maximum magnetization value that can be reached. This value is reached when all the magnetic moments in our material are oriented parallel to the excitation field [1].

Remanent Magnetization Mr: is the value of the magnetization that remains when the value of the excitation field has been reset to zero (the material has been previously saturated) [2].

Coercive Field Hc: corresponds to the point in the cycle at which magnetization cancels out, and quantifies the "softness" at which the material magnetizes or demagnetizes. Materials that magnetize easily and have a coercive field of less than 1000 A/m are generally classified as soft materials, and iron with an Hc field less than 100 A/m can be taken as a reference.
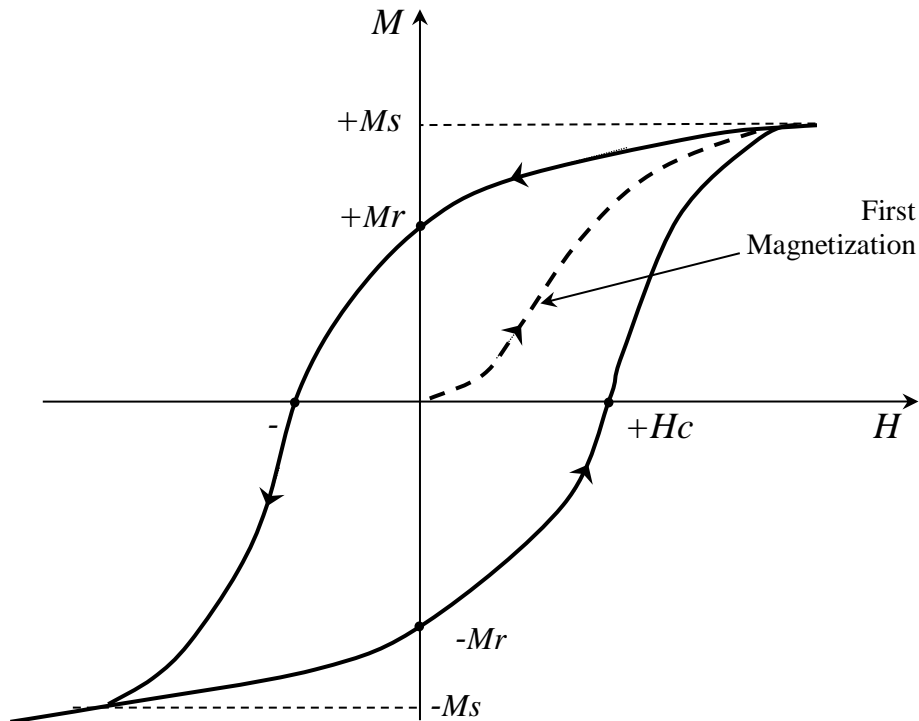
Figure IV.10: Hysteresis cycle: variation in magnetization as a function of an external applied field H in a ferromagnetic material [6].

4.3   Structural Properties

4.3.1 Surface and Interface

A surface is a zone separating two phases, which may be made up of the same body, or two different bodies. However, we sometimes differentiate between surfaces separating a condensed phase (liquid or solid) from its vapor, and interfaces, which may be located between two condensed phases, or between a condensed phase and a vapor.

4.3.1.1 Surface Anisotropy

Surface atoms have less symmetry than atoms within the material. Their influence on particle energy can depend on the orientation of magnetization, this gives rise to surface anisotropy, which can also be dependent on impurities adsorbed to the surface, the magnitude of the surface contribution to magnetic anisotropy energy increases with decreasing material size, becoming significant only for materials smaller than 10 nm [7].

4.3.1.2 Surface Effects

The number of first neighbours for an atom located at the surface is lower than in the case of bulk material, this results in a local reorganization of the electron density, associated with a reduction in the width of the d-bands in the proximity of the surface [8], this contraction of d-bands can be associated with the appearance of surface states, these effects can alter the density of states at the Fermi level, as well as the magnetic moment of surface atoms. Table IV.2 compares the volume and surface magnetic moments of some 3d magnetic transition metals. From this table, we can see that the value of the magnetic moment is lower for dense surfaces ((110) for iron, (111) for cobalt and nickel), than for "less compact" surfaces (100). Loose layers have higher magnetic moments than solid metals.

The magnetic moment approaches the value obtained for the free atom as dimensionality and coordination are reduced. Thus, as we move from the bulk material to the surface (001), then to the linear chain, moving on to the isolated atom, the magnetic moment takes on the values:

- 2,15 => 2,98 => 3,3 => 4,0 μ_B/atom for iron,
- 0,56 => 0,68 => 1,1 => 2,0 μ_B/atom for nickel.

- **Table IV.2**: Volume and surface magnetic moments (µB/atom) of 3d transition metals [8].

Magnetic Moment per Element (in μ_B)	Cr (bcc)	Fe (bcc)	Co (hex)	Ni (fcc)
Surface (100)	2,49	2,98	1,95	0,68
Surface (110)		2,65		
Surface (111)			1,82	0,63
Volume	0,59	2,15	1,76	0,56

4.3.1.3 Interface Effects

Interfaces also affect magnetic properties. These interface-induced effects on the magnetism of ultrathin films can have three different origins:

Editing the lattice parameter: A variation in the material's lattice parameters can be caused by material deformations. In general, a contraction of the lattice leads to a widening of the d-bands and therefore to a decrease in magnetic moment, contrarely, lattice expansion tends to increase magnetic moments in the deposited layer. [8].

Stabilization of exotic crystallographic phases: A small change in the lattice parameter of elements is enough to transform its magnetic phase, for example iron (normally CC), epitaxially grown on Cu (100), its structure becomes that of the substrate, and the magnetic properties change from those of Fe (CC) to Fe (CFC) is and the ferromagnetic state into an antiferromagnetic one, these significant changes in electronic structure are due to small distortions in the crystal arrangement.

Interface hybridization: the hybridization effects between the two materials are unpredictable, for instance calculations show that an iron atomic plane is ferromagnetic with a moment close to 3 µB/atom, and when it is deposited on a tungsten(W) substrate (001), strong hybridization with W leads this plane to become antiferromagnetic, with a moment of 0.93 µB/atom. If a second atomic

plane is deposited, the iron layer becomes ferromagnetic again, and therefore the interface hybridization must be taken into account. [8].

4.3.2 Dipolar Moment

The dipole moment (μ) is an essential tool for studying intermolecular interactions, as it reflects the molecular charge distribution, and can therefore be a descriptor of charge movement through the molecule, high charge mobility in the system is explained by the high values of the dipole moment, which are a good factor that predict NLO properties.

4.3.3 Reactivity Indicators

Several indices characterize the material reactivity, the most widely used ones are the electronic chemical potential (μ) and global hardness (η), which can be calculated using the orbital boundary energies HOMO and LUMO orbital energies (ε_H and ε_L respectively).

The chemical electron potential (μ) is the tendency of an atom or molecule not to let its electrons escape and is given by the following equation

$$\mu = \frac{1}{2}(\varepsilon_H + \varepsilon_L) \tag{4.13}$$

The hardness (η) expresses the resistance of a system to change its number of electrons given by equation **4.14** while softness is just the inverse of hardness (S=1/ η)

$$\eta = (\varepsilon_H - \varepsilon_L) \tag{4.14}$$

4.3.4 Thermodynamic Properties

Thermodynamic parameters such as zero-point vibrational energy, Gibbs free energy (G), entropy (S), and enthalpy (H) play an important role in characterizing molecular systems, providing a foundation for predicting and interpreting the behavior of molecules in various conditions and environments. These parameters are calculated by the following equations

$$G = H - TS$$

$$\Delta S = \frac{q_{rev}}{T} \tag{4.15}$$

$$H = U + PV$$

where H is the enthalpy, T is the absolute temperature, q_{rev} is the heat absorbed or released for a reversible process. U is the internal energy, P is the pressure, and V is the volume.

4.4 Magneto-Optical Properties

The interaction between the light wave and a magnetic field in material science has been studied since the 19th century. In 1846, M. Faraday observed that when a linearly polarized beam passes through a medium subjected to a magnetic field $B_{//}$ parallel to the direction of light propagation (subsequently referred to as the longitudinal field), its polarization rotates by an angle θ_F [9]. Since then, this effect has been known as the Faraday effect.

The influence of a magnetic field perpendicular to the direction of light propagation (which we call a transversal field) was discovered later, in 1901 by J. Kerr and in 1902 by Q. Majorana [10]. A linearly polarized wave passing through a material medium subjected to a transverse magnetic field B⊥, sees its polarization become elliptical, this phenomenon has been studied in detail by A. Cotton and H. Mouton. [11]

4.4.1 Definition

The magneto-optic effect corresponds to a modification in the propagation of an electromagnetic wave in a material, an electromagnetic wave is composed of a magnetic wave and an electric wave in phase and with a perpendicular polarization vector, the electromagnetic wave has a very wide frequency distribution, including all light frequencies. The magneto-optic effect corresponds to the change in polarization of this electromagnetic wave when it comes into contact with a material placed in a quasi-static magnetic field, there are different magneto-optical effects, depending on the orientation of the magnetic field to the propagation vector of the light, the

polarization of the light and the measurement method used, whether transmission or reflection. A distinction is made between first-order magneto-optical effects, proportional to odd terms of the magnetic field, and second-order effects, proportional to even terms of the magnetic field.

4.4.2 Light Polarization

Polarization phenomena are those related to the vector character of the two light wave characteristics, namely the electric field $\vec{E}$ and the magnetic field $\vec{B}$, since the changes in $\vec{E}$ and $\vec{B}$ are related over time, it therefore, need only to describe the behavior of the electric field $\vec{E}$. The plane formed by the wave vector $\vec{k} = k\vec{u}_z$ with $k = \frac{2\pi}{\lambda} = \frac{\omega}{c}$ and the electric field $\vec{E}$ is called the plane of polarization, defined by

$$\vec{E} \begin{cases} E_{Px}\cos(\omega t - kz + \varphi_x) \\ E_{Py}\cos(\omega t - kz + \varphi_y) \\ 0 \end{cases} \tag{4.16}$$

φ_x, φ_y are vibration phases while E_{Px}, E_{Py} represent vibration amplitudes

On the other hand, the direction of polarization is the direction taken by $\vec{E}$, and the wave's state of polarization can be observed from the axis of propagation. In this example, Oz The direction taken by the electric field $\vec{E}$ in the plane perpendicular to the Oz axis, i.e. the Oxy plane, is called the polarization direction of the light wave. Specifically, we study the vector edge motion $\vec{E}$ at random point P, it will vary in sinusoidal form with time, we denote $(\vec{u}_x, \vec{u}_y, \vec{u}_z)$ the unit vectors in the Ox, Oy, and Oz directions, and there for Three types of polarization can be identified: elliptical (the most general case), circular, and rectilinear
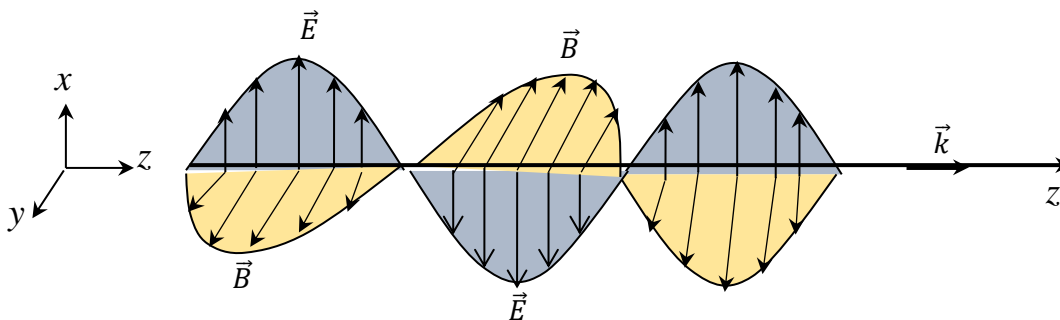
Figure.IV.11. A light wave with orthogonal $\vec{E}$ and $\vec{B}$ fields. The vector k indicates the propagation axe

4.4.2.1 Elliptical Polarization

Considering (x, y), the coordinates of the point P located at the edge of the vector $\vec{E}$ a wave plane x at date t as presented in Figure IV.12
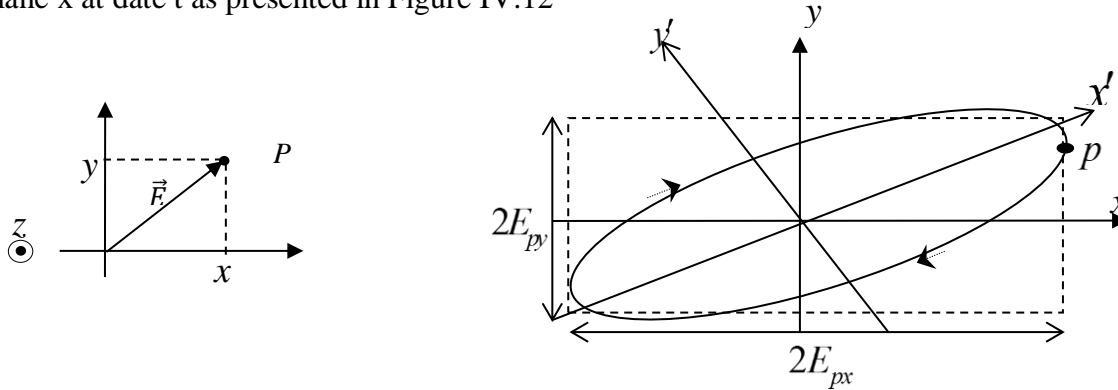
Figure IV.12 Electromagnetic wave polarization presentation

For quantities E_{Px}, E_{Py}, and φ with no singular values, P representation by vector $\vec{E}$ describes, in the wave plane (Oxy), an ellipse within $2E_{Px}$ and $2E_{Py}$ rectangle sides, and with $\varphi \neq k\pi$ and $k \in z$

Ellipse equation with inclined axes not aligned with Ox and Oy is written as

$$\left(\frac{E_x(z,t)}{E_{Px}}\right)^2 - 2\frac{E_x(z,t)}{E_{Px}}\frac{E_y(z,t)}{E_{Py}}cos\varphi + \left(\frac{E_y(z,t)}{E_{Py}}\right)^2 = sin^2\varphi \qquad \textbf{(4.17)}$$

Whenever $\varphi = \pm\frac{\pi}{2}$ or $\varphi = \pm\frac{3\pi}{2}$ equation **4.14** becomes

$$\left(\frac{E_x(z,t)}{E_{Px}}\right)^2 + \left(\frac{E_y(z,t)}{E_{Py}}\right)^2 = 1 \qquad \textbf{(4.18)}$$

(4.18) is an ellipse equation for axes Ox and Oy, lengths $2E_{Px}$ and $2E_{Py}$. It represents the most general case. It is obtained for the following values of φ :

$\varphi \in \,]0, \pi[$ the wave is left-polarized and the helicity is said to be positive
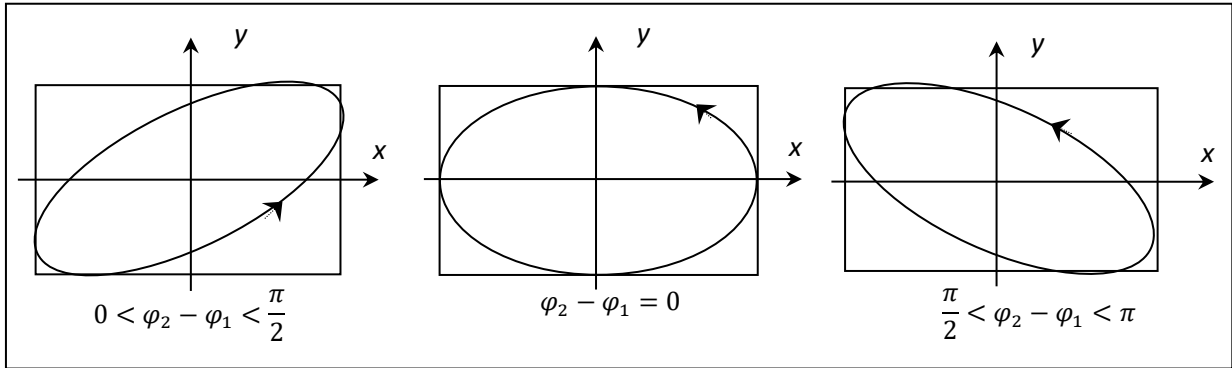
Figure IV.13 Left elliptical polarized wave

$\varphi \in \,]\pi, 2\pi[$, the wave is right-polarized and the helicity is negative
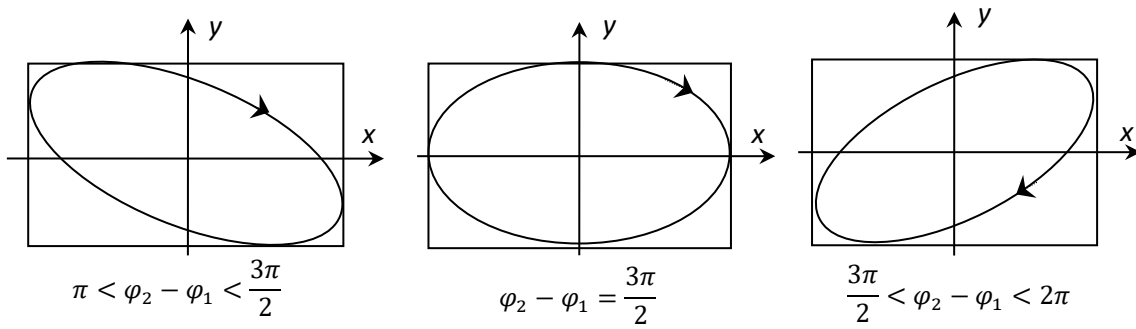
Figure IV.14 right elliptical polarized wave

4.4.2.2 Circular Polarization

Whenever $\varphi = \pm\dfrac{\pi}{2}$ or $\varphi = \pm\dfrac{3\pi}{2}$ and $E_{Px} = E_{Py} = E_P$ equation **4.17** is written as:

$$(E_x(z,t))^2 + \left(E_y(z,t)\right)^2 = E_P{}^2 \tag{4.19}$$

That represents a circle equation with E_P radius

positive helicity   **negative helicity**

(a) $\varphi = +\dfrac{\pi}{2}$ (b) $\varphi = -\dfrac{\pi}{2}$
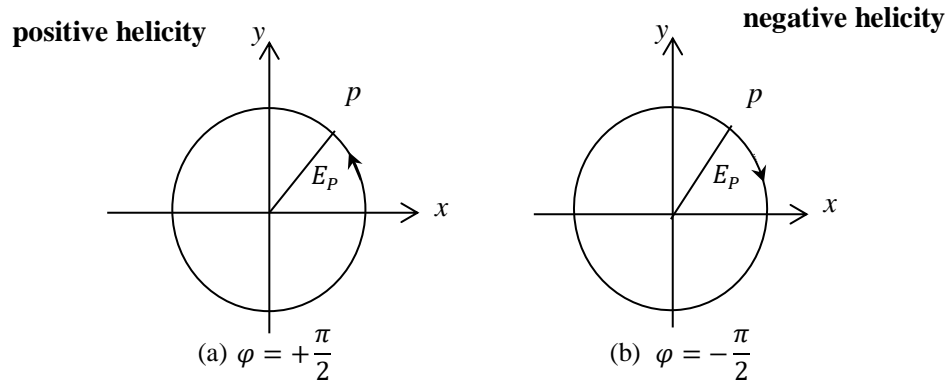
Figure IV.15 Circular polarized wave: (a) left, (b) right

4.4.2.3   Linear Polarization

If $\varphi = 0$ or π equation **4.17** is written

$$\frac{E_y(z,t)}{E_x(z,t)} = \pm \frac{E_{Py}}{E_{Px}} = cst \qquad\qquad \textbf{(4.20)}$$

The two components are either in phase φ=π or in an opposite phase φ=π and the electric field remains in a fixed direction in space, the polarization is said to be linear. The structure of a linear-polarized sinusoidal traveling plane wave is then very simple, as the E and B fields maintain a fixed direction in space during propagation.

(a) $\varphi = 0$ (b) $\varphi = \pi$
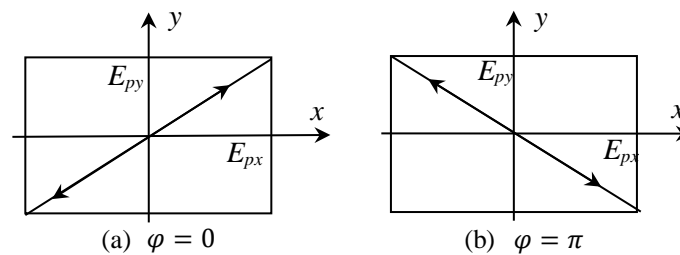
Figure IV.16 Linearly polarized wave (a) in phase, (b) in phase opposition.

4.4.3   Magneto-optical Kerr Effect (MOKE)

4.4.3.1 Definition

The magneto-optical Kerr effect (MOKE) is an experimental technique for studying the magnetic properties of a medium through optical techniques, the Kerr effect is based on measuring the effects produced by the reflection of a polarized beam on a magnetic material,   this involves either a change in beam polarization (rotation or ellipticity) or a change in light intensity. In ferromagnetic materials, magneto-optical effects are dominated by spin-orbit effects, which couple the electron spin moment to the spatial components of the wave function [12], optical dipole transitions are carried out by the spin direction, which produces a linear magnetic contribution (Faraday or Kerr effects, magnetic circular dichroism) to the diagonal element of the optical conductivity tensor [1].

This property, known as the magneto-optic Kerr effect, is demonstrated in the reflection of polarized light from a magnetic material as a small rotation (10-5 rad) of magnetization according to the polarization axis and corresponding optical phase shift (ellipticity). Previous experiments have established the value of the Kerr effect as a useful sensor of the magnetic properties of thin films. [13-15]

 In a thin ferromagnetic film deposited on a reflective substrate, it is possible to analyze the polarization state of the light reflected by the device, in this configuration, light enters the material on a round trip. Let's consider a plane wave that is linearly polarized, here, the "magnetic field" vector will be used to characterize its state of polarization, the latter can be seen as the decomposition of two circularly right and left polarized waves Figure IV.16. The component whose "angular velocity" vector is in the same direction as the virtual electric currents (or magnetic moments), that is responsible for the magnetization M of the material will "rotate" faster than the other. We can see that linear polarization experiences a rotation when a   magnetization is developed parallel to the direction of light propagation.

Let's Consider $\vec{E}_i$ the incident light wave $\vec{E}_L$, circular component (left) and $\vec{E}_R$ circular component (right)
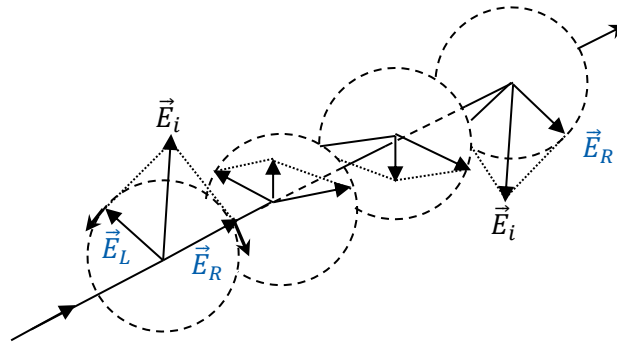
Figure IV.17 Schematic diagram of the Kerr effect.

4.4.3.2 Kerr Effect Geometries

The magneto-optical interaction resulting from the reflection of a linearly polarized electromagnetic wave on a magnetized material, is referred to as the magneto-optical Kerr effect. This effect was discovered by J. Kerr in 1876 [16, 17], when a linearly polarized light is directed onto and reflected by a magnetic sample, there are several geometric configurations of the Kerr effect, depending on the orientation of the electric field $\vec{E}$ and the magnetization of the material $\vec{M}$, Generally speaking there are three of them: polar, longitudinal and transversal.
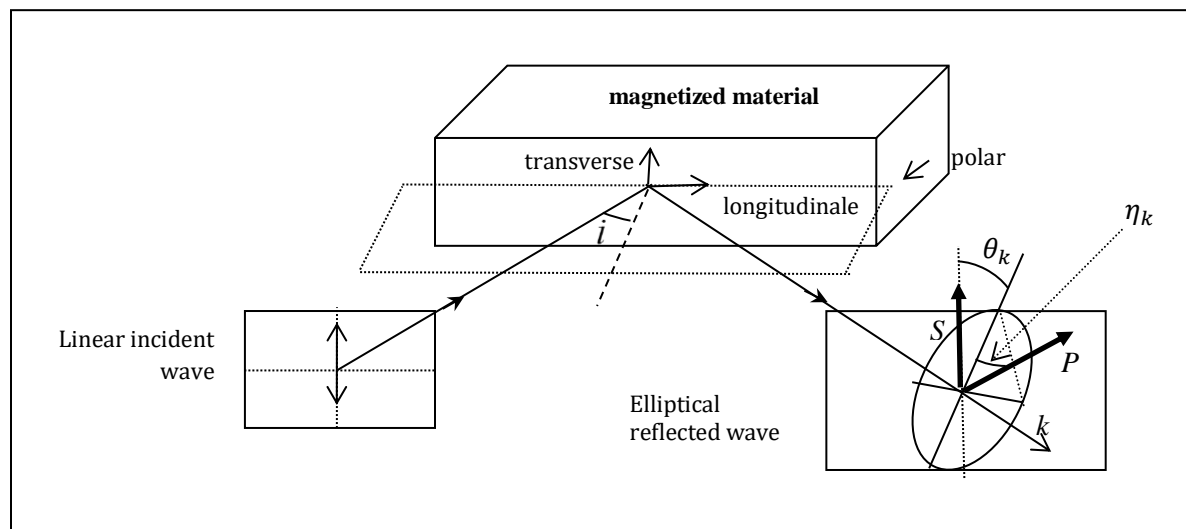
Figure IV.18 Diagram of the Kerr magneto-optic effect: transformation of a linear wave into an elliptical wave after reflection on a magnetized medium.

$\boldsymbol{\theta_k}$ Rotational angle of the polarization ellipse's principal axis concerning the polarization direction.

$\boldsymbol{\eta_k}$ Ellipticity which is defined as the ratio of the minor axis to the major axis of the ellipse. At low values, it becomes confused with the angle at which the minor axis is seen from the top of the ellipse.

4.4.3.2-a   Polar Configuration

Magnetization is perpendicular to the sample and in the plane of incidence. The Kerr effect in its polar geometry is the most widely used in theoretical and experimental studies, due to its technological applications (magnetic recording and reading).
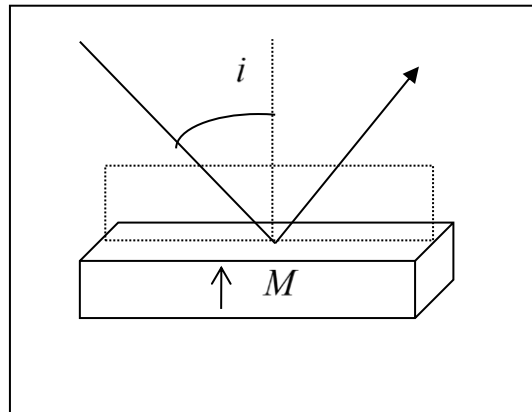
Figure IV.19 Diagram of Polar configuration.

Since all magneto-optical properties are directly related to optical conductivity, in a tetragonal system in which magnetization is oriented along the z-axis, the conductivity tensor is given by the expression [18]:

$$\tilde{\sigma}(\omega) = \begin{pmatrix} \sigma_{xx} & \sigma_{xy} & 0 \\ -\sigma_{xy} & \sigma_{xx} & 0 \\ 0 & 0 & \sigma_{zz} \end{pmatrix} \tag{4.21}$$

 the plane light reflected from a thin-film metal surface becomes elliptically polarized (Figure IV-20), and its major axis undergoes a slight rotation, under these conditions, the complex Kerr angle is given by the relation [19]

$$\frac{1 + \tan \eta_k}{1 - \tan \eta_k} e^{-2i\theta_k} = \frac{(1 + n_+)(1 - n_-)}{(1 - n_+)(1 + n_-)}$$

(4.22)

where θ_k is Kerr rotation and η_k is Kerr ellipticity.

The eigenvalues of the tensor defined by equation **4.21** are given by

$$n_{\pm}^2 = 1 + \frac{4\pi}{\omega}\left(\sigma_{xx} \pm \sigma_{xy}\right)$$

(4.23)

Since θ_k and, for most materials, are less than one degree (small rotations), expression **4.19** takes the form:

$$\theta_k + \eta_k = \frac{-\sigma_{xy}}{\sigma_{xx}\sqrt{1 + \left(\frac{4\pi i}{\omega}\right)\sigma_{xx}}}$$

(4.24)
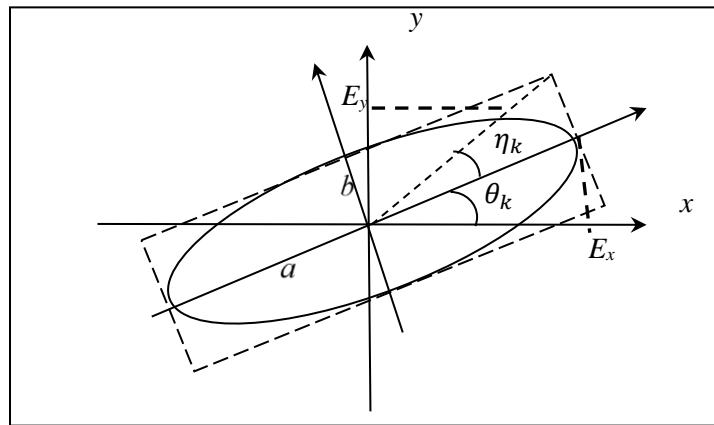
Figure IV.20 The polarization ellipse, with its orientation angle, θ_k and ellipticity, η_k

4.4.3.2-b Longitudinal Configuration

Magnetization is in the plane of the sample and the incidence plane as shown in Figure IV.21, using the Longitudinal -MOKE geometry, the dielectric tensor is written as
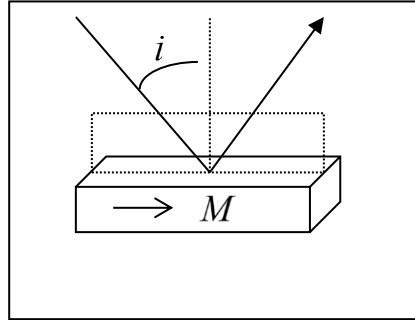
Figure IV.20 Longitudinal configuration

$$\tilde{\varepsilon}(\omega) = \begin{pmatrix} \varepsilon_{xx} & 0 & \varepsilon_{xz} \\ 0 & \varepsilon_{xx} & 0 \\ -\varepsilon_{xz} & 0 & \varepsilon_{xx} \end{pmatrix} \tag{4.25}$$

The Kerr complex angle is given by the relation [20]

$$\theta_{s.p}^{L} + i\eta_{s.p}^{L} = \frac{2\varepsilon_{xz}\ sin\varphi\ \cos\varphi\ \sqrt{\varepsilon_{xx}}}{D} \tag{4.26}$$

With

$$D = \left\{ \sqrt{\varepsilon_{xx}(\varepsilon_{zz} - sin^2\varphi)} + \sqrt{\varepsilon_{zz}(\varepsilon_{xx} - sin^2\varphi)} \right\} \left\{ \sqrt{(\varepsilon_{xx} - sin^2\varphi \pm cos\varphi)} \right\} \left\{ \sqrt{\varepsilon_{xx}\varepsilon_{zz}}cos\varphi \right.$$
$$\left. \mp \sqrt{\varepsilon_{zz} - sin^2\varphi} \right\}$$

φ Is the incidence angle

The (+) and (-) signs refer respectively to the p and s polarizations of the incident light. In the case of $\varepsilon_{xx} \approx \varepsilon_{zz}$, equation **4.26** becomes

$$\theta^L_{s.p} + i\eta^L_{s.p} = \frac{\varepsilon_{xx}\,sin\varphi\,\sqrt{\varepsilon_{xx-}sin^2\varphi} \pm sin\varphi\,tan\varphi}{(\varepsilon_{xx} - 1)(\varepsilon_{xx} - tan^2\varphi)\sqrt{\varepsilon_{xx} - sin^2\varphi}} \tag{4.27}$$

4.4.3.2-c Transversal Configuration

The magnetization is in the plane of the sample and perpendicular to the plane of incidence, this effect is less widely used because it only indicates a change in the intensity of the reflected light, in general, it has the same order of magnitude as the longitudinal effect, in this case, no effect is observed at normal incidence [21]. T-MOKE does not measure rotation or ellipticity, but it measures the difference in the intensity of reflected light, it exists only when the incident light mode is p-type, the difference in reflectivity is given by:

$$\delta_k = Re\left\{\frac{2\varepsilon_0\varepsilon_{xz}sin2\varphi}{\varepsilon^2_{xx}cos^2\varphi - \varepsilon_0\varepsilon_{xx} + \varepsilon^2_0\,sin^2\varphi}\right\} \tag{4.28}$$

T-MOKE is mainly used to study magnetic properties, in particular, to observe magnetic domains on the surfaces of magnetic materials. In polar and longitudinal configurations, the linearly polarized electromagnetic wave is transformed into an elliptical wave after reflection on the magnetized medium, the transverse Kerr effect does not lead to a change in the polarization of the incident wave, but rather to a change in its reflectivity.
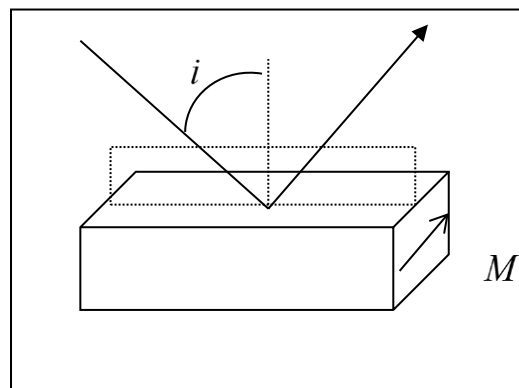
Figure IV.20 Transversal configuration

4.5 Nonlinear Optical Properties

Non-linear optical phenomena appear when the response of a material to a light field depends non-linearly on the intensity of that field, this phenomena play an essential role in the photonics field, offering superior performance to electronic devices in data transmission and processing. In photonics, photons are used to capture, store, process, and transmit information, with many similarities to electronic circuits, the ability of materials to process light at switching points is crucial, as they exhibit nonlinear optical characteristics, materials of this kind have attracted considerable attention over the decades, due to their potential applications in optical signal processing, optical switching, frequency generation, optical data storage, the development of high-speed communication and dynamic image processing, compared to electronics, photonics offers several advantages, including higher speed due to the massless nature of photons. In optical communications, the absence of electromagnetic interference means that many optical information channels can be transmitted in the same optical fiber, due to wavelength division multiplexing [22,23].

4.5.1 Nonlinear Optical Theory

To describe the principle of optical non-linearity more precisely, let's consider how the dipole moment per unit volume (polarization P) depends on the intensity of the electric field E_ω of an optical wave applied at frequency ω, in the case of a linear material, P is a linear function of E, which means P oscillates at the same frequency (ω) as E_ω

$$P^\omega = \varepsilon_0 \chi E^\omega \tag{4.29}$$

Where χ is the linear electrical susceptibility of the dielectric and ε_0 is the permittivity of vacuum. NLO phenomena (i.e. involving at least two optical fields) occur in intense fields, as the intensity of the applied field increases (e.g. using lasers), the polarization response of the material is no longer linear, the optical response can be described by equation **4.30** developing the induced polarization (P) into a series of gradually increasing powers of $E\omega$, and given by

$$P = \varepsilon_0 \chi E^\omega + \varepsilon_0 \chi^2 E^\omega E^\omega + \varepsilon_0 \chi^3 E^\omega E^\omega E^\omega + \cdots \tag{4.30}$$

Where χ is the second-order linear susceptibility tensor of the material, χ^2 and χ^3 are the quadratic and the cubic non-linear optical susceptibility tensors, respectively.

At the molecular level, equation **4.30** is expressed as follows

$$P = \sum_{j} a_{ij}\chi E^{\omega} + \sum_{j<k} \beta_{ijk} E^{\omega 2} + \sum_{j<k<l} \gamma_{ijkl} E^{\omega 3} + \cdots \qquad (4.31)$$

Where

a_{ij} is the linear polarizability

β_{ijk} is the first hyperpolarizability

γ_{ijkl} is the second hyperpolarizability

i, j, k, l are the molecular coordinates

The nonlinearity of molecules and materials depends on their symmetry. If the materials are centrosymmetric amorphous, then their quadratic NLO response is canceled as for any physical quadratic property due to the cancellation of the pair tensors (χ^2, χ^4...). In a standard case, the polarization intensity is proportional to the applied optical field. whereas in a high-intensity field such as a laser, the non-linear terms cannot be neglected [24].

Non-linear optical properties (NLO) defined by polarizability (α), anisotropy of polarizability ($\Delta\alpha$), first-order hyperpolarizability (β) and the second order of polarizability (γ). The polarizability (α) consists of six tensor components α_{xx}, α_{yy}, α_{zz} , α_{xy}, α_{yz}, α_{zx} while the first hyperpolarizability (β) with it ten tensor components (β_{xxx}, β_{yxx}, β_{xyy}, β_{yyy}, β_{zxx}, β_{xyz}, β_{zyy}, β_{xzz}, β_{yzz}, and β_{zzz}), in addition to the second hyperpolarizability (γ) with its 20 tensor components (γ_{xxxx}, γ_{xxxy}, γ_{xxyy}, γ_{xyyy}, γ_{yyyy}, γ_{xxxz}, γ_{xxyz}, γ_{xyyz}, γ_{yyyz}, γ_{xxzz}, γ_{xyzz}, γ_{yyzz}, γ_{xzzz}, γ_{yzzz}, γ_{xxyx}, γ_{xyyx}, γ_{yxyy}, γ_{yyxy}, γ_{yyxx}). reveal the response of a system in an applied electromagnetic field. These parameters are calculated using the following expressions

$$\alpha = \frac{1}{3}(\alpha_{xx} + \alpha_{yy} + \alpha_{zz}) \qquad (4.32)$$

$$\Delta\alpha = \left[\frac{(\alpha_{xx} - \alpha_{yy})^2 + (\alpha_{yy} - \alpha_{zz})^2 + (\alpha_{zz} - \alpha_{xx})^2}{2}\right]^{\frac{1}{2}} \tag{4.33}$$

$$\beta = (\beta_x^2 + \beta_y^2 + \beta_z^2)^{\frac{1}{2}} \tag{4.34}$$

With

$$\beta_x = \beta_{xxx} + \beta_{xyy} + \beta_{xzz} \tag{4.35}$$

$$\beta_y = \beta_{yyy} + \beta_{xxy} + \beta_{yyz} \tag{4.36}$$

$$\beta_z = \beta_{zzz} + \beta_{xxz} + \beta_{yyz} \tag{4.37}$$

$$\gamma = \frac{1}{5}\left[(\gamma_{xxxx} + \gamma_{yyyy} + \gamma_{zzzz}) + 2(\gamma_{xxyy} + \gamma_{yyzz} + \gamma_{zzxx})\right] \tag{4.38}$$

Along with the dipole moment that is calculated with the following expression

$$\mu = (\mu_x^2 + \mu_y^2 + \mu_z^2)^{\frac{1}{2}} \tag{4.39}$$

μ_x, μ_y, μ_z are dipole moments along x, y, and z direction

4.6 References

1   Coey, J. M., & Parkin, S. S. (2021). Handbook of magnetism and magnetic materials. (No Title).

2   Houcher, A. (2022). Etude des propriétés structurales et magnéto-optiques des films ultraminces déposés par épitaxie pseudomorphique (Doctoral dissertation).

3   O'handley, R. C. (2000). Modern magnetic materials: principles and applications. Wiley.

4   Cullity, B. D., & Graham, C. D. (2011). Introduction to magnetic materials. John Wiley & Sons.

5   Suryanarayana, C. (2001). Mechanical alloying and milling. Progress in materials science, 46(1-2), 1-184.

6   Brissonneau, P. (1997). Magnétisme et matériaux magnétiques pour l'électrotechnique. Hermes.

7   Nolting, W., & Ramakanth, A. (2009). Quantum theory of magnetism. Springer Science & Business Media.

8   Serra, R. (2009). Moments magnétiques et structure électronique au voisinage des interfaces : Etude par spectroscopie de pertes d'énergie d'électrons et calculs ab-initio (Doctoral dissertation, Toulouse 3).

9   Faraday, M. (1851, December). Experimental researches in electricity. In Abstracts of the Papers Communicated to the Royal Society of London (No. 5, pp. 592-595). London : The Royal Society.

10   Cadène, A., Sordes, D., Berceau, P., Fouché, M., Battesti, R., & Rizzo, C. (2013). Annexe F. Mémoire d'habilitation à diriger les recherches, 88, 137.

11   Scholten, P. C. (2004). First century of colloid magneto-optics.

12   Argyres, P. N. (1955). Theory of the Faraday and Kerr effects in ferromagnetics. Physical Review, 97(2), 334.

13   Erskine, J. L., & Stern, E. A. (1973). Magneto-optic kerr effect in ni, co, and fe. Physical Review Letters, 30(26), 1329.

14   Bader, S. D., & Moog, E. R. (1987). Magnetic properties of novel epitaxial films. Journal of Applied Physics, 61(8), 3729-3734.

15   Moog, E. R., & Bader, S. D. (1985). Smoke signals from ferromagnetic monolayers: p (1× 1) Fe/Au (100). Superlattices and microstructures, 1(6), 543-552.

16   Kerr, J. (1877). XLIII. On rotation of the plane of polarization by reflection from the pole of a magnet. The London, Edinburgh, and Dublin Philosophical Magazine and Journal of Science, 3(19), 321-343.

17   Kerr, J. (1878). XXIV. On reflection of polarized light from the equatorial surface of a magnet. The London, Edinburgh, and Dublin Philosophical Magazine and Journal of Science, 5(30), 161-177.

18   Kleiner, W. H. (1966). Space-time symmetry of transport coefficients. Physical Review, 142(2), 318.

19   Buschow, K. H. J. (1988). Ferromagnetic Materials, edited by EP Wohlfarth and KHJ Buschow North-Holland.

20   Višňovský, Š. (1984). Magnetooptical longitudinal and transversal Kerr and birefrigence effects in orthorhombic crystals. Czechoslovak Journal of Physics B, 34, 969-980.

21   Boukelkoul, M. (2018). Propriétés magnéto-optiques des couches ultraminces et des slabs à base de métaux de transition (Doctoral dissertation).

22   Khireddine, A. (2022). Étude théorique des propriétés structurales et optiques des composés organométalliques (Doctoral dissertation).

23   ZOUAOUI, R. M. (2017). Substitutions d'Hydrocarbures aromatiques polycycliques (HAP) par divers groupements fonctionnels. Etude par MQ de leurs propriétés (Doctoral dissertation).

24   Shen, Y. R. (1984). Principles of nonlinear optics.

Chapter 5
Results and Discussion

5.1 Study of Structural, Magnetic, and Magneto-Optical Properties of Ni/Rh(001) Ultrathin Films

5.1.1 Introduction

Developing new crystalline structures based on transition metals with exotic physical properties (magnetic, electrical, optical, etc.), different from those observed in usual crystalline states is one of the motivations behind this work. The magneto-elastic and magneto-optical behavior of 3d elements (Ni, Fe, Co) has been the subject in pleanty of theoretical and experimental studies, particularly in magnetic data storage and recording.

In this subchapter, we calculate the structural, magnetic, and magneto-optical properties of ultrathin Nickel films deposited by pseudomorphic epitaxy on a Rh(001) substrate.

5.1.2 Calculation techniques

The surface study using the SPR-LMTO-ASA method differs from that used for the bulk (volume) materials, where the cell that generates the entire system depends on the orientation of the surface under study and must be defined for each orientation, thus for each orientation different properties occurs. For a surface of a monoatomic crystal, the loss of symmetry at the surface forms a new and different environment that makes certain sites inequivalent.

Implimenting SPR-LMTO-ASA method to study ultra-thin films requires the identification of certain technical details that considered essential to elaborate surfaces in specific directions.

5.1.3 Surface design: Supercell

In this work, the used method (SPR-LMTO-ASA) is based on Bloch's theorem, which is designed to study systems with translational symmetry in the three crystallographic directions x, y, and z (crystals considered to be infinite at the atomic scale). The theoretical treatment of surfaces

then leads to the problem of the crystalline symmetry which is fractured in a direction that is perpendicular to the surface (semi-infinite crystals), due to this Bloch's theorem is no longer applicable, to resolve this periodicity problem, the semi-infinite crystal is represented by a limited set of atomic layers (slabs) oriented so that the surface plane is perpendicular to the z-axis, the slab is repeated infinitely, with two consecutive slabs being separated by several planes made up of spherical atoms with zero charge E (Empty). The combination of the slab, layers and the empty spheres forms a super-cell, and the succession of an infinite number of super-cells in a perpendicular direction to the surface becomes symmetrical in the z-direction. To ensure that the surface created is well appropriate to the theoretical study, we ensure that the choice of the atomic planes number in the slab, along with the thickness of the space separating two consecutive slabs must satisfy the following two conditions [1,2]

- the space between two slabs must be large enough to eliminate any mutual interaction between two consecutive slabs, and to achieve this, we must ensure that the central plane of the vacuum space electronic charge remains zero [3], this condition ensures periodicity along the axis perpendicular to the surface without affecting the band structure calculation.

- the slab as a representation of the semi-infinite crystal (volume + surface) must retain the solid state's properties at the center, to achieve this, the number of the metal's atomic planes in the slab must be sufficient to recover the properties of the infinite crystal at the center of the slab [4].

5.1.4 Calculation Details

The calculation method used is the SPR-LMTO-ASA method, implemented in the lmto 5.0.0.2 code with an exchange and correlation potential, introduced by the Local Spin Density Approximation (LSDA) with combined corrections.

The basic geometry in this calculation method is divided into two parts: an interstitial part and a muffin-tin part, inside the muffin-tin spheres where the basic functions are developed in terms of spherical harmonics and radial functions that are solutions to the Dirac equation, while in the

interstitial part, the basis functions are proportional to the regular solution of the Laplace equation, the rest part (tails spheres) are given as a linear combination of Newman functions.

The spin-orbit interaction is included directly in the matrix elements of the Hamiltonian for the part within the muffin-tin spheres, and the Dirac equation is solved in a self-consistent manner [5].

To calculate the magneto-optical properties, the components of the optical conductivity tensor are given by the sum of the interband and intra-band transitions, for the interband transitions calculations, we have adopted the electric dipole approximation, and the elements of the optical conductivity tensor are given by Kubo-greenwood linear response formula, while the intra-band transitions are defined by the Drude formula, which are only noticeable in the vicinity of low values of incident radiation energy (~1eV) [6].

To reduce computation time, the SPR-LMTO-ASA method uses the crystal's symmetries, and solves the problem in only a part of the Brillouin zone (BZ), bounded by the so-called high-symmetry points, in the case of the (001) surface the unit cell is tetragonal, so the BZ part concerned by the calculations is a parallelepiped limited by $2\pi/a$, $2\pi/b$, $2\pi/c$ parameters, where a, b, c are the normal lattice parameters of the supercell [2].

5.1.5 Structural Properties

Our first aim in studying the Nin/Rh (001) system with n=1, 2, and 3 is to determine the crystal structure of the ultrathin Nickel film (supercell parameters a, b, and c), because the deposition of Ni atomic planes on a Rh substrate establishes a new crystal structure for this system.

In our study we chose the rare earth element Rhodium as s substrate due to the good matching (**7%** mismatch) compared to the Nickel, and the growth of Rh in the (001) direction is a cubic-centered structure (CC), however, its bulk structure is a face centered cubic (FCC) with a lattice parameter of a_{Rh}=3.803 Å and 1.34 Å atomic radius that gave it a compact and stable structure, to be the second most dense element, its electronic configuration is [Kr] $4d^8$ $5s^1$ which provides it with high chemical stability, electronic and thermic conductivity, it is also considered as an excellent light reflector [7].

The number of Rh layers is chosen on the concept that the substrate must combine all the physical properties of solid Rhodium

 To proform the surface relaxation process on our film, we first test the number of planes needed to evaluate the relaxation of its first two planes with reasonable accuracy, we limited ourselves to a Rhodium substrate made up of seven atomic planes, to get a central plane that represents a symmetrical point which allow to gain time in the calculations, without compromising the quality of results, by doing so we benefits from a plane of symmetry that facilitates the calculation of the substrate's physical properties. On the other hand, Nickel is a transition metal that is characterized by FCC crystalline structure, lattice parameter of a_{Ni}=3.524 Å and 1.24 Å atomic radius with the electronic configuration [Ar] $3d^8$ $4s^2$ which made it more chemically reactive than rhodium, as well as a good electrical and chemical conductor with high light reflectivity.[7].

The reference distance f_0 is defined as the half distance between two consecutive Rh atomic planes, it is taken for all systems to be equal to a_{Rh} / 2 so $f_0 = \frac{a_{Rh}}{2} = 1.9015$ Å

To obtain the most suitable distance d1, d2, and d3 (shown in Figure V.2), we optimize the total energy of the systems studied as a function of the distance ratio between the desired distance d and the reference distance f_0 (E=f (d/f_0)), using a series function with the powers to fit the calculated results, the obtained results are summed in the three curves presented in   Figure V.3
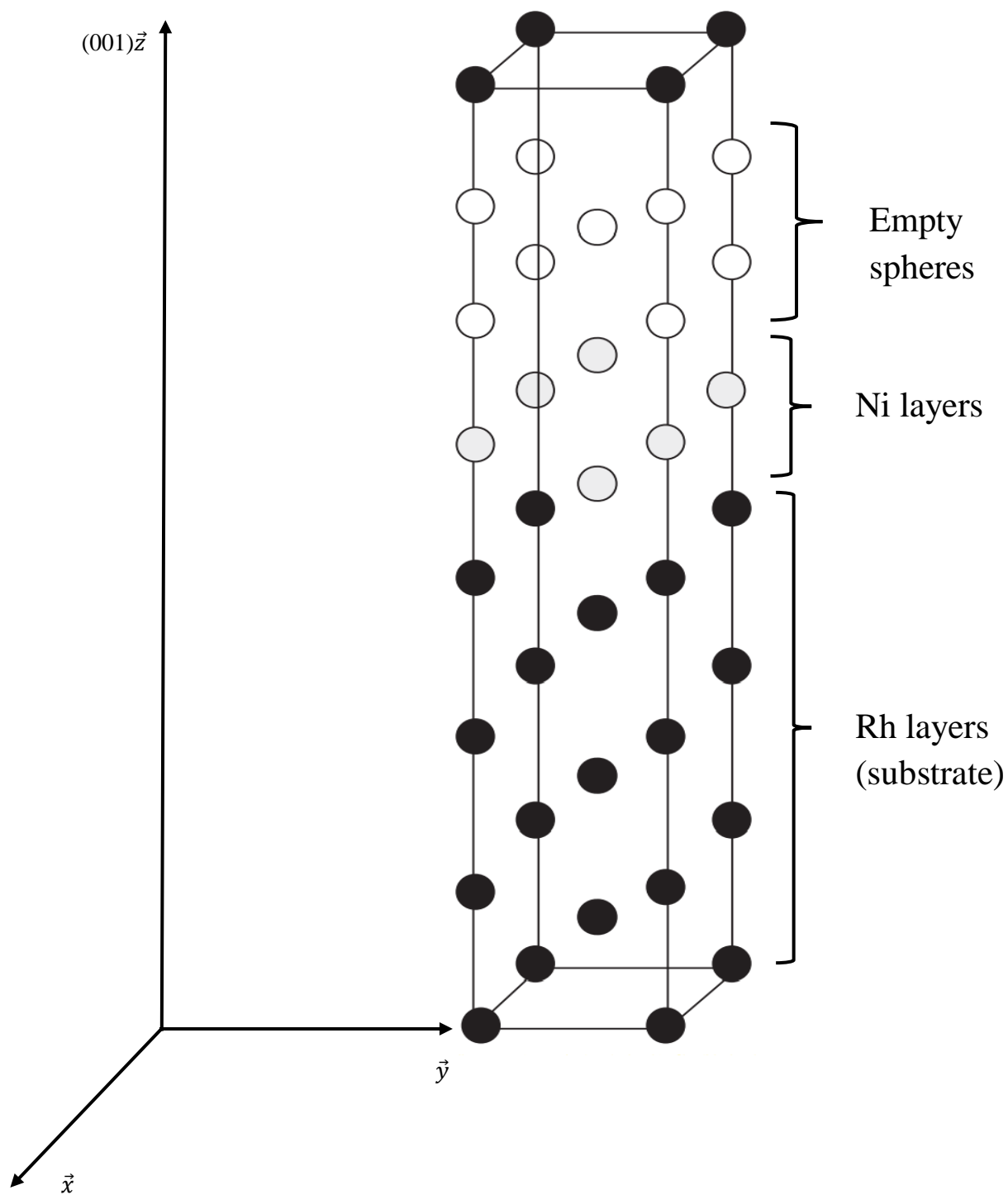
Figure V.1: Super-cell representation of three epitaxial Ni layers on a substrate of seven Rh planes in the crystallographic direction (001)
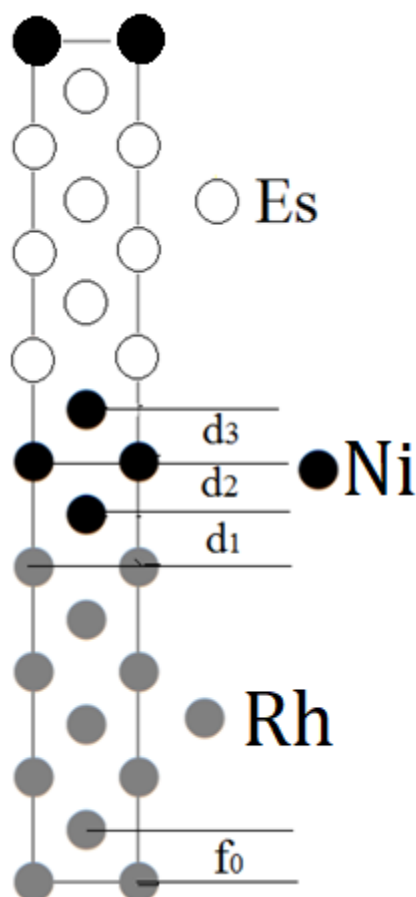
Figure V.2: Distance between planes in the supercell of the Nin/Rh (001) system where d_1: is the distance between the last Rh plane and the first Ni plane, d2 is the distance between the second and third Ni planes, d_3: distance between the second and third Ni planes and f0: distance between two Rh planes.

The first step in the deposition of Nickel first layer on the Rhodium substrate, the Ni_1/Rh (001) obtained system is of special interest, as it represents a contact between the two different elements, according to the first curve in Figure V.3 the first-plane deposition of Ni on Rh (001) takes place at a distance of $d_{Ni1-Rh7} = 1.732$Å

After that, we deposit the second layer of Nickel (Ni_2/Rh (001)) and according to the second curve in Figure V.3, the lowest energy level is reached for $d_{Ni2-Ni1} = 1.6005$Å.

For the final step of deposition with the third Ni layer an interatomic distance is found $d_{Ni3-Ni2}$ =1.577Å corresponding to equilibrium

Based on these results, the lattice parameters in the growth direction are:

$$a = a_{Rh(001)} = \frac{1}{2}[110] = \frac{1}{\sqrt{2}} \, a_{Rh} = \frac{1}{\sqrt{2}} \times 3.803 = 2.689 \text{ Å}$$
$$c = d_2 + d_3 = 3.1776 \text{ Å}$$

The new crystal structure has the characteristics a=b=2.689 Å and c=3.1776 Å with a c/a tetragonal ratio equal to 1.18, this structure corresponds to a body-centered tetragonal (BCT) structure.

This exotic crystalline structure of the Nickel film influences its magnetic and magneto-optical properties, indeed, the presence of the spin-orbit interaction leads to a ground state that depends on the relative orientation of the magnetization and the crystallographic axes, in other words, there is a correlation between the crystallographic properties and the magnetic and magneto-optical properties[8].

5.1.6 Magnetic Properties

This subsection aims to calculate the magnetic moment per atom and determine the magnetic phase of ultrathin Nickel films, the study of magnetic properties of Nin/Rh(001) with n=1, 2, 3 ultrathin films, consists of determining the magnetic moment and magnetic coupling taking into account the correlation between crystal structure and magnetic moment, according to literature the magnetic moment of FCC Nickel in its bulk form varies between 0.52 μ_B and 0.606 μ_B [9,10], however Nickel layers deposited on substrates oriented to (001) or (111) directions have different magnetic moments, in fact, a study of the Nin/ GaAs(001) system proved that the top layers of Ni deposited on GaAs(001) are ferromagnetic, with a enhanced magnetic moment [10].

Based on the results found in the previous section, we study the magnetic properties by calculating the magnetic moment per atom in each atomic plane of the Ni, the magnetic moment distribution for each layer is shown in Figure V.4. The Density of State (DOS) is calculated to back up these findings, DOS results are presented in Figures V.5
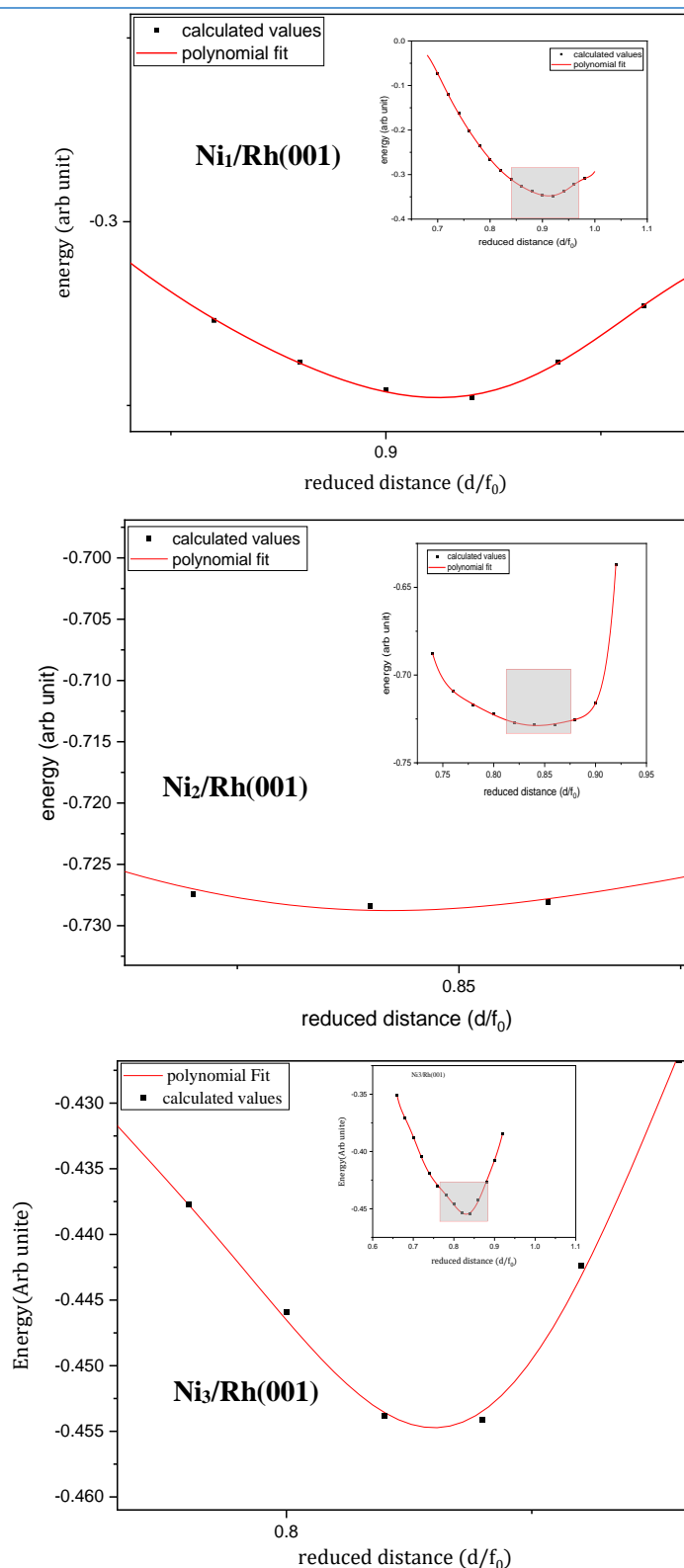
Figure V.3: Relaxation processes of Ni_n/Rh(001) systems (black dots are the calculated values and red solid lines are the fits), d and f_0 represent the inter-plane distance in the film and substrate respectively.

In the first graph that represents the $Ni_1/Rh(001)$, Rh exhibits a considerable magnetic polarization characterized by a high magnetic moment of 0.246 μ_B, this polarization is due to a hybridization between Ni and Rh orbitals, confirmed through the DOS curve through the asymmetrical Rh bands as shown in Figure V.5(a), while the magnetic moment of Ni layers is enhanced to 0.704 μ_B compared to the Bulk system, in contrast, unusual findings for the inter-planes of Rh_{2-5} indicate an antiferromagnetic behavior with a magnetic moment ranging between -0.01 and -0.036 μ_B. Hence, the magnetic moments found are a direct consequence of the new crystalline structure of the Ni film, while the inter planes of Rh are affected by the overlapping between the Ni_1 and Rh_7 so it reacted in a way to save the paramagnetic character of the massive Rh.

For the second layer presented in the second graph, the Ni_1 magnetic moment decreases to 0.554 μ_B going towards the bulk value due to bond formation between Ni_1 and Ni_2, creating a bulk like environment for the Ni_1, while in Figure V.5(b) the DOS registered a noticeable diminution in intensity caused by a drop in the exchange splitting compared to the $Ni_1/Rh(001)$ system, in comparison, the second Ni_2 layer magnetic moment is 0.718 μ_B, which is considered a high value, regarding the last Rh layer, there is a small drop to 0.242 μ_B which further confirms the ferromagnetic correlation between the Ni and Rh layers.

Finely for the last layer Ni_3, the averrage magnetic moments of the Ni layers are different from the bulk value, with a linear development as the number of layers increases, where the magnetic moment of the final Ni layer (Ni_3) is 0.562 μ_B, which is closer to the bulk value due to the stressed state of the system 1.577 Å, less than the bulk value by 0.185 Å that worked on reducing its magnetic moment, for the Ni_2 layer its value is reduced to 0.4 μ_B due to its position between two Ni layers and the stressed situation is characterized by $d_{Ni2-Ni1}$ =1.6005Å, creating a bulk-like compressed environment, on the other hand, the Ni_1 layer has a low magnetic moment of 0.2 μ_B, which is significantly lower than the bulk value, and the interpretation of these data is that the magnetic state of Ni_1 is altered by the substrate via the correlation between Rh_7 and Ni_1, leading to the arrangement of its spins antiparallel to the other Ni layers spins, causing Ni_1 to fluctuate between two states: paramagnetic and ferromagnetic [8], this is supported by the d states curve, which becomes wider according to Figure V.5(c). The Rh_7 layer reverted to its original paramagnetic phase with a 0.034 μ_B magnetic moment. DOS displays a single curve with no spin difference due to the Ni_1 low magnetic moment, indicating that there are no signs of ferromagnetic coupling.

Based on the results found in this study, we conclude that there is a strong correlation between the film's crystalline structure and its magnetic behavior for the first and second layers, indeed, for the three studied systems, the decrease of the inter-atomic distance affected the magnetic moment values, the calculations also led to a magnetic phase characterized by ferromagnetic coupling.
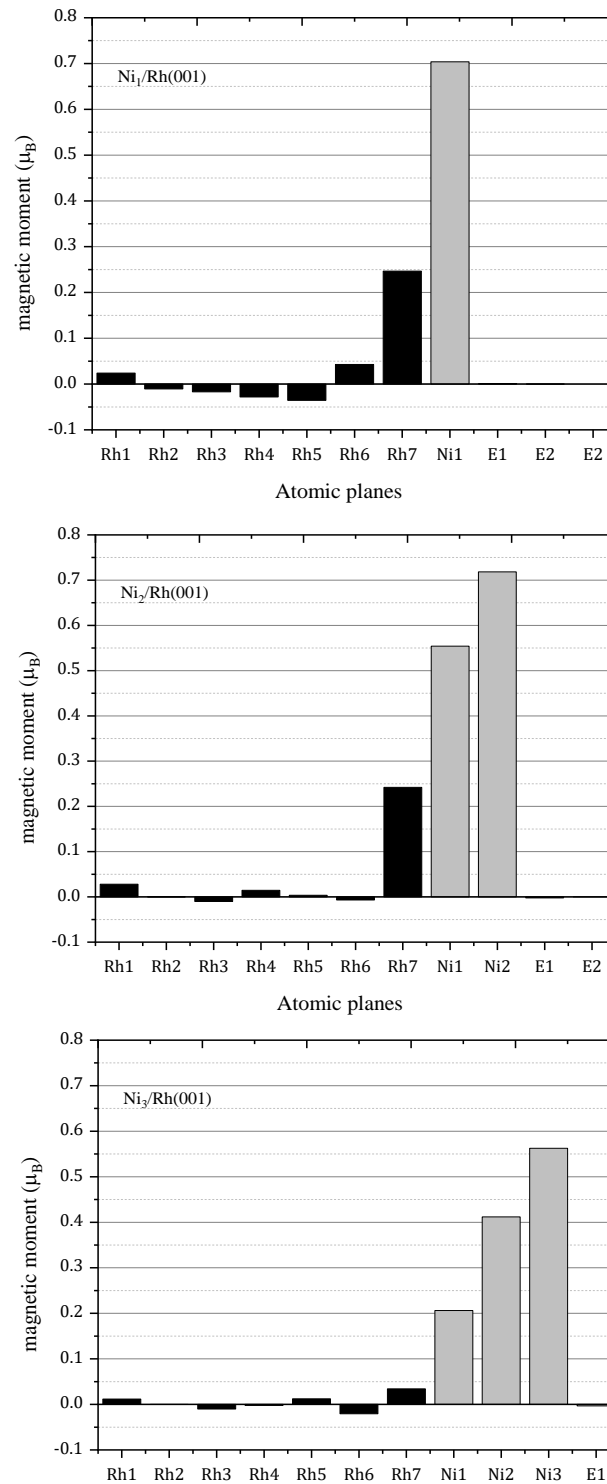
Figure V.4 The magnetic moment distribution of atomic planes in the Ni_n/Rh(001) systems
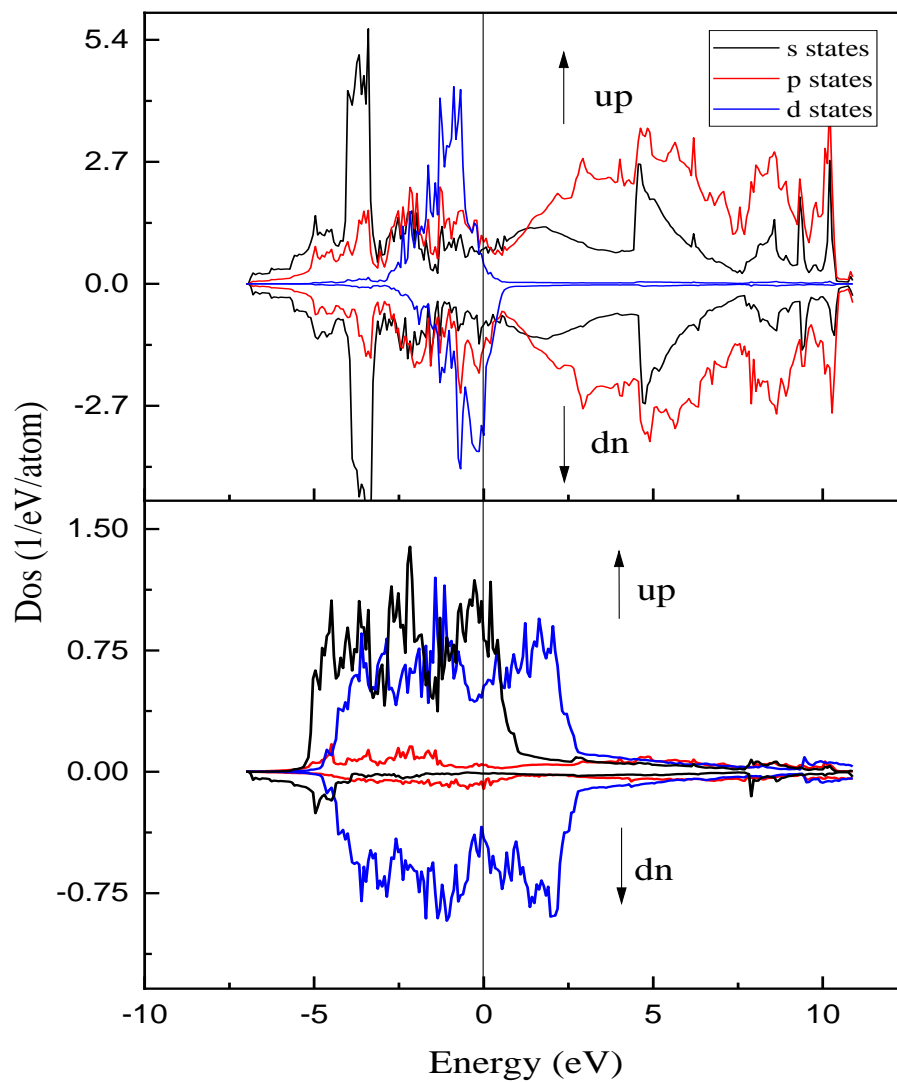
Figure V.5 (a): DOS of the Ni$_1$/Rh system
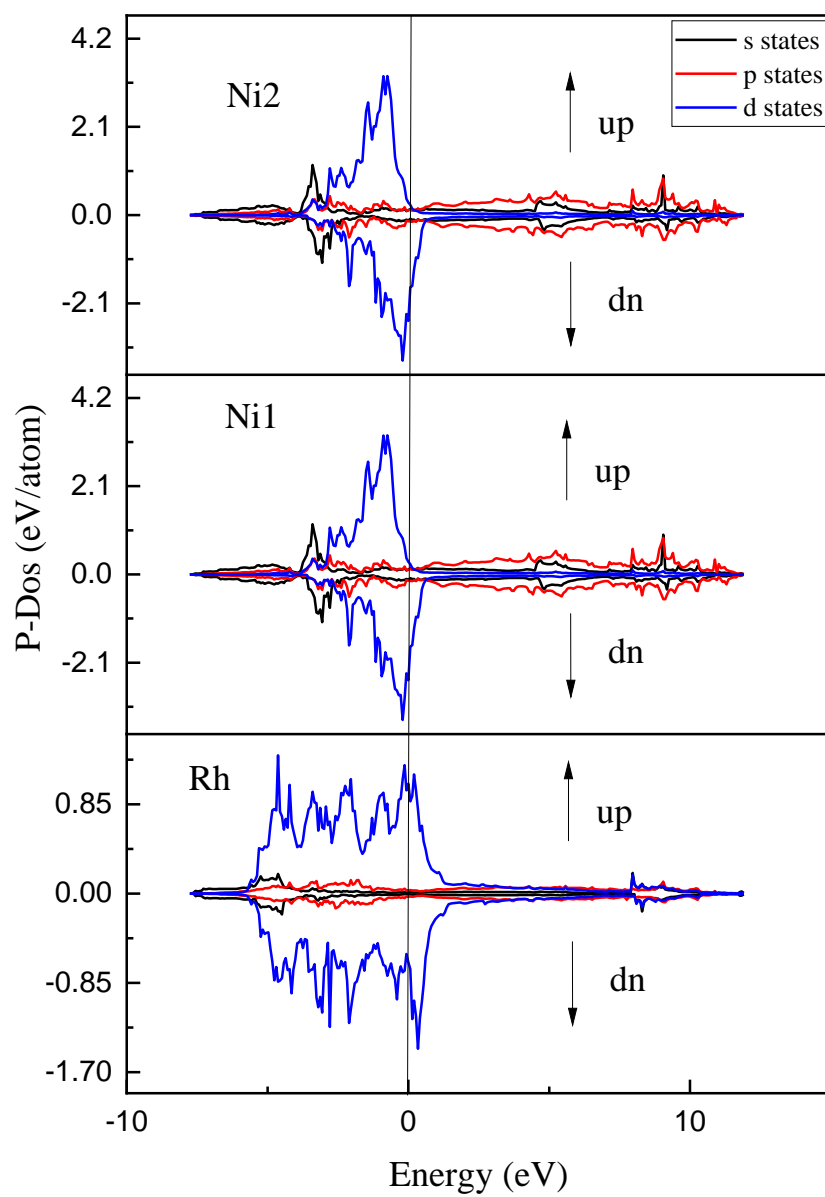
Figure V.5(b): DOS of the Ni2/Rh system
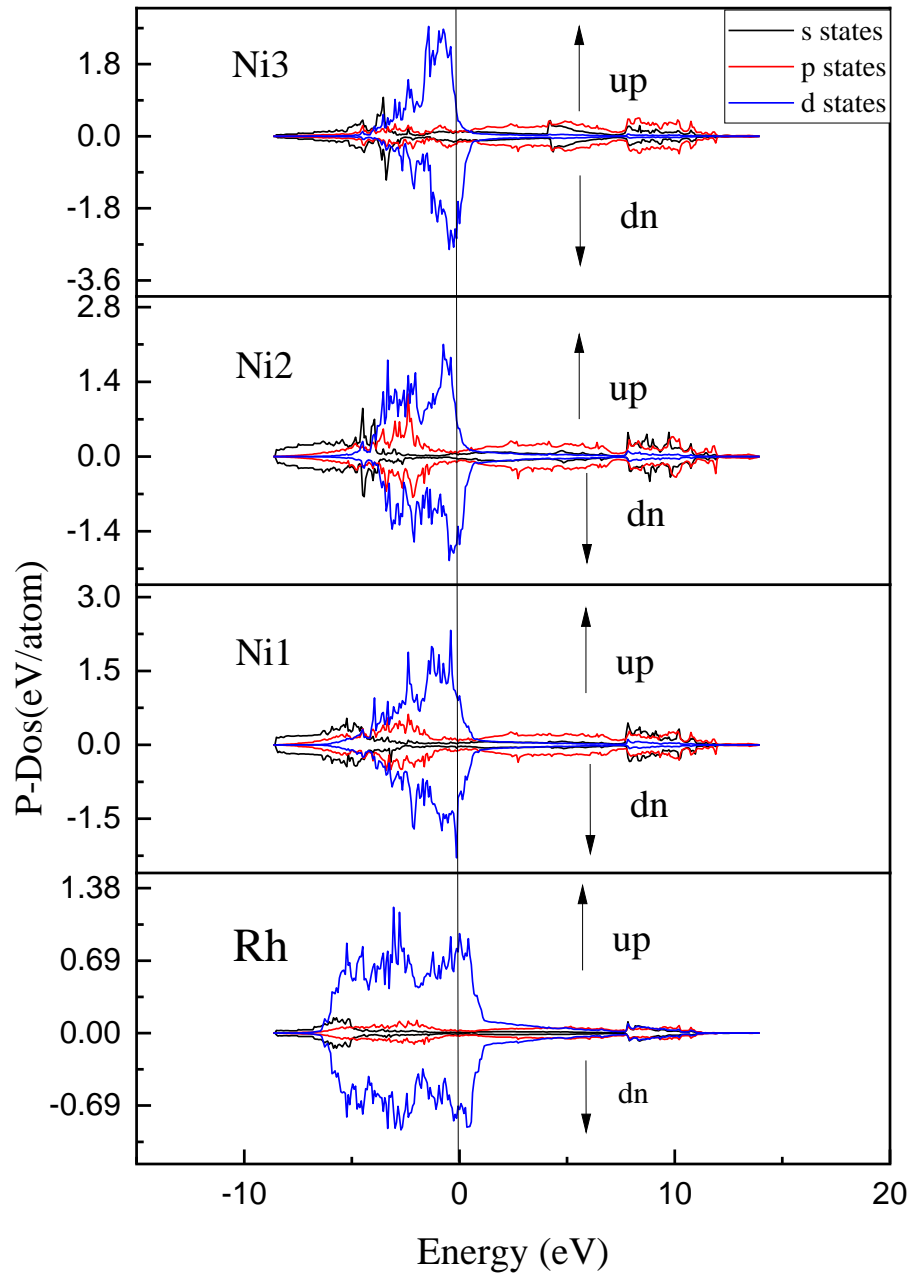
Figure V.5(c): DOS of the Ni_3/Rh system

5.1.7 Magneto-optical Properties

To investigate the magneto-optical properties, we introduce the term for the polarized spin part of the exchange-correlation potential, in our system, we adopt the Kerr effect spectrum calculation in its polar geometry (P-MOKE), and to do so, we calculates Kerr rotations θ_k as a function of incident photon energies, the range of incident radiation energies used is extended to 10 eV, and the corresponding rotations are shown in Figure V.6.

To explain the atomic origins of the different peaks in the Kerr effect spectrum characterizing the system under study, we based our discussion on an analysis of DOS curves presented in Figure V.5 and interband contributions using the electron-photon interaction along with the following selection rules.
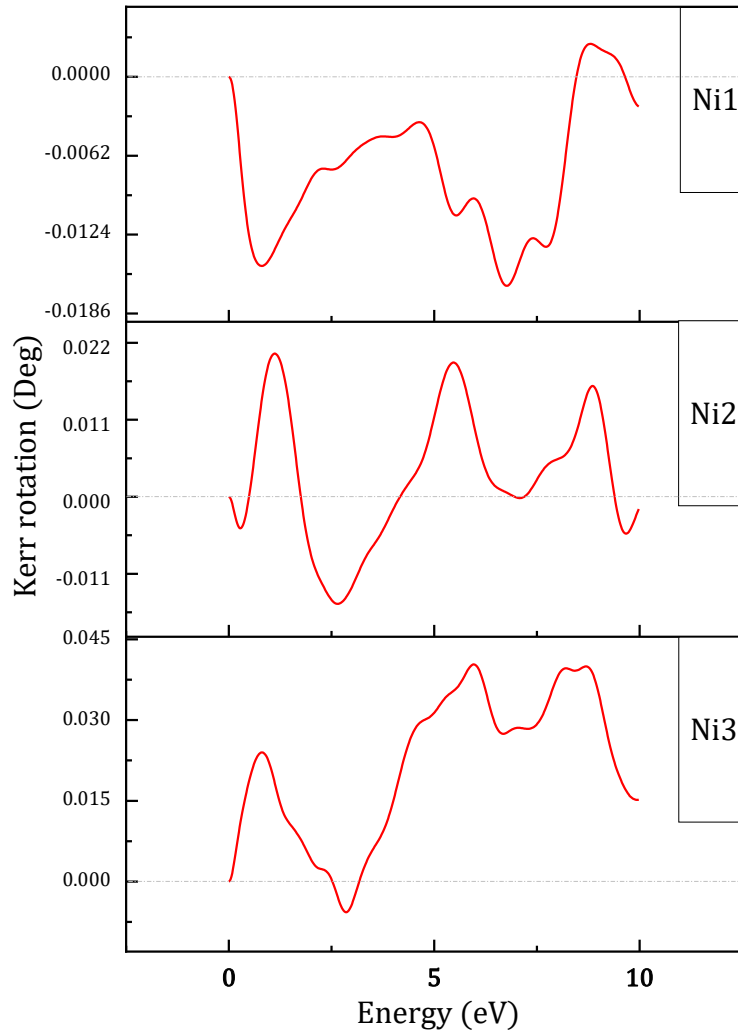
Figure V.6 P-MOKE spectra of the Ni_n/Rh(001) ultrathin films

$$\Delta l = \pm 1 \quad \text{and} \quad \Delta j = 0, \pm 1$$

So

$$\Delta m_j = \begin{cases} +1 & if \quad \lambda > 0 \\ -1 & if \quad \lambda < 0 \\ 0 & if \quad \lambda = z \\ \pm 1 & if \quad \lambda = x, y \end{cases}$$

With

Δl is the orbital quantum number

Δj is total angular momentum

Δm_j is the azimuthal quantum number

λ is vector potential polarization

For the first system $Ni_1/Rh(001)$, two negative rotations are recorded, the one with the wide angle occurring at 6.9 eV, which is in the extreme ultraviolet region (0.177 nm), for the second peak a rotation is recorded at 0.81 eV at the near-infrared region (1520 nm) and a positive rotation at 8.8 eV. The second and third layers (Ni_2/Rh and Ni_3/Rh) exhibited one negative rotation at 2.63 eV and 2.85 eV respectively along with three positive rotations as presented in Figure V.6, according to the DOS presented in Figure V.5 all of the rotations corresponds to an s→p, p→s and d→p transitions. Table V.1 summarizes all of the transitions for each rotation peak, along with their appropriate energy level and rotation angle. The inter-band transitions underlying these rotations occur between localized states in the absence of spin-flip.

Table V.1 Rotation peaks, energy levels, and inter-band transitions for each layer

System	Energy (eV)	rotation angle (deg)	Corresponding Interband Transitions
Ni1/Rh	0.800	-0.01486	s↓→p↑
	6.770	-0.01642	s↑→p↑ , p↑→s↑ , d↑→p↑ , s↓→p↓ , p↓→s↓ , d↓→p↓
	8.796	0.00259	s↑→p↑ , p↑→s↑ , d↑→p↑ , s↓→p↓ , p↓→s↓ , d↓→p↓
Ni2/Rh	1.122	0.02046	p↑→s↓
	2.650	-0.0153	s↑→p↑ , p↑→s↑ , s↓→p↓ , p↓→s↓ , d↓→p↓
	5.469	0.01918	s↑→p↑ , p↑→s↑ , s↓→p↓ , p↓→s↓ , d↓→p↓
	8.85	0.01583	s↓→p↓ , s↑→p↑
	9.673	-0.00526	s↑→p↑ , p↑→s↑ , s↓→p↓ , p↓→s↓
Ni3/Rh	0.800	0.02399	p↓→s↓ , d↓→p↓ , s↑→p↑ , p↑→s↑
	2.850	-0.0057	s↑→p↑ , d↓→p↓
	5.950	0.04034	s↑→p↑ , d↑→p↑ , s↓→p↓ , p↓→d↓ , d↓→p↓
	8.690	0.03997	s↓→p↓ , p↓→s↓ , d↓→p↓ , s↑→p↑ , p↑→s↑ , p↑→d↑ , d↑→p↑

.

The main feature of the magneto-optical properties in ultra-thin films Ni_n/Rh(001) (n=1, 2, 3), is a negative peak with appreciable rotation angles along with a noticeable shift for each layer added. Magnetic storage quality and capacity are influenced by the number of electrons, the average free electron path, and the lifetime of the polarization, given the metallic nature of the studied films, electrons have a relatively large mean free path, and consequently, the information stored can only be influenced by spin-flip, which is absent in Nin/Rh systems, and for This we conclude that the system could be considered as a potential medium of high-capacity magnetic storage

5.2   Theoretical Investigation of Structural, Spectroscopic (IR, 1H and 13C NMR), Static, and Frequency-Dependent Nonlinear Optical Properties of 4-[(1E)-3-(4-Methoxyphenyl)-3-Oxoprop-1-en-1-yl]Phenyl4 Methylbenzene-1-Sulfonate

5.2.1 Introduction

Nonlinear optical (NLO) properties are the reactions of a substance when subjected to a strong optical field. Penetrating in the NLO materials field is a new and exciting area of research, regarding it sophisticated technological application in spectroscopy, sensors, information processing, communication, signal treatment, and data storage. On the other hand organic materials are also an interesting research materials due to their low cost, potential to modify at the atomic level, functional groups that act as electron donors and acceptors via the π-conjugator bridge, and its flexibility [11].

Chalcone, a widely dispersed organic substance that exists in vegetables, fruits, teas, and other plants, is selected in this study due to its potential for superior NLO characteristics when compared to other materials. Chalcone derivatives are an excellent organic supplement that can combine with metals to generate organometallic compounds, they have several uses in the environment, healthcare, pharmaceuticals, and cancer treatment [12]. NLO investigations have demonstrated that chalcone's third-order NLO characteristics may be improved by replacing donor and acceptor groups with enhanced ones, such as hydroxyl and methoxyl groups, furthermore, the asymmetric electron distribution enhances the performance of the acceptor donor groups, resulting in photon absorption of 10^{-7}esu, making it an excellent NLO material for fluorinated chalcone [13].

This subsection employs the DFT approach to explore the vibrational frequencies, electronic absorption spectrum, frontier molecular orbitals, molecular electrostatic potential surface, and NLO characteristics of the 4-[(1E)-3-(4-Methoxyphenyl)-3-Oxoprop-1-en-1-yl]Phenyl 4-Methylbenzene-1-Sulfonate (4MPMS) that was synthesized experimentaly by Vinaya and his co-workers [14].

5.2.2   Computational Details

The geometric structure of 4MPMS is calculated using the GAUSSIAN 16. software, which employs DFT framework, using B3LYP (Becke's three-parameter hybrid functional utilizing the LYP correlation functional) technique. and the 6-311++G(d,p) basis set, data are presented and analyzed using the GAUSSVIEW 6 program. Structural optimization is carried out at the ground state energy level, the IR vibrational spectrum is confirmed by the potential energy distribution (PED) analysis, and the obtained results are multiplied by 0.9614 to reduce the disparity between the experimental and theoretical results. SWIZARD software is used to retrieve and support the highest occupied and lowest unoccupied molecular orbitals (HOMO and LUMO). The Gauge Including the Atomic Orbital (GIAO) approximation approach is used to evaluate the NMR spectra by incorporating the effects of the magnetic field directly into the atomic orbitals, which helps in achieving more accurate results in determining the structural dynamics, and molecules enviroment. The Conductor-like Polarizable Continuum Model (CPCM) is utilized to account for the solvent effect.

Based on the optimized structure, the 4MPMS Non-Linear Optical Properties (NLO) and molecular potential surface are examined in Both static and dynamic states to obtain polarizability, first- and second-order hyperpolarizability (α, β, and γ).

5.2.3 Structural Properties

The obtained experimental [14] and optimal theoretical molecular structures with atomic numbering are shown in Figure V.7, while the experimental and theoretical distances and interatomic angles are presented in Table V.2 and Table V.3 respectively.
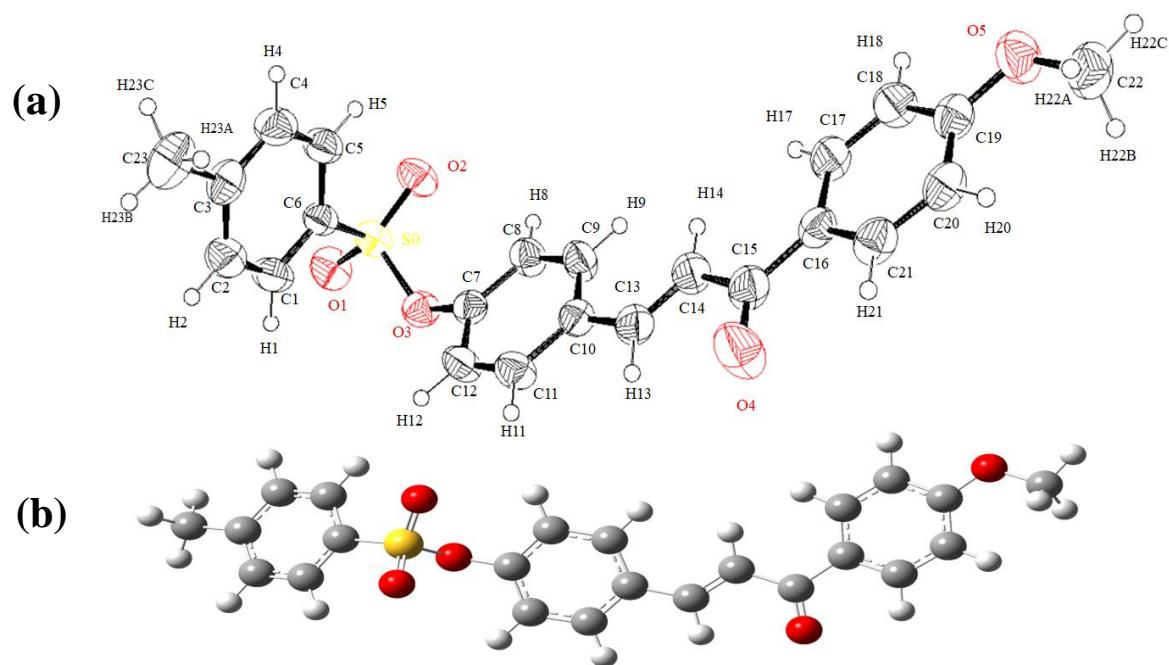
Figure V.7 (a) Crystal structure with the atomic numbering (ORTEP), and (b) optimized geometry for 4MPMS (GAUSSIAN)

Table V.2. The experimental and calculated bond length (Å) for 4MPMS

Bonds	Experimental	B3LYP/6-311++G(d,p)
S-O1	1.4208	1.4545
S-O2	1.4286	1.4554
S-O3	1.5974	1.6837
S-C6	1.746	1.7808
O3-C7	1.41	1.3983
O4-C15	1.218	1.2261
O5-C19	1.364	1.3583
O5-C22	1.422	1.4241
C1-C2	1.371	1.3905
C1-C6	1.377	1.3924
C2-C3	1.375	1.4004
C3-C4	1.377	1.4005
C3-C23	1.508	1.5077
C4-C5	1.373	1.3904

C5-C6	1.377	1.3924
C7-C8	1.375	1.3946
C7-C12	1.369	1.3893
C8-C9	1.38	1.3866
C9-C10	1.386	1.4071
C10-C11	1.39	1.4053
C10-C13	1.464	1.4614
C11-C12	1.374	1.39
C13-C14	1.306	1.3448
C14-C15	1.479	1.4862
C15-C16	1.476	1.4954
C16-C17	1.392	1.406
C16-C21	1.391	1.4004
C17-C18	1.366	1.3848
C18-C19	1.393	1.4009
C19-C20	1.371	1.401
C20-C21	1.37	1.389
C3-C23	1.508	1.5077
C4-C5	1.373	1.3904
C5-C6	1.377	1.3924
C7-C8	1.375	1.3946
C7-C12	1.369	1.3893
C8-C9	1.38	1.3866
C9-C10	1.386	1.4071
C10-C11	1.39	1.4053
C10-C13	1.464	1.4614
C11-C12	1.374	1.39
C13-C14	1.306	1.3448
C14-C15	1.479	1.4862
C15-C16	1.476	1.4954
C16-C17	1.392	1.406

C16-C21	1.391	1.4004
C17-C18	1.366	1.3848
C18-C19	1.393	1.4009
C19-C20	1.371	1.401
C20-C21	1.37	1.389

Table V.3 The experimental and calculated bond angles (°) for 4MPMS

Bond angles	Exp. [17]	B3LYP/6-311++G(d,p)
O1-S-O3	109.71(10)	107.97
O1-S-C6	109.35(11)	110.09
O2-S-O1	119.52(11)	120.66
O2-S-O3	102.64(10)	108.07
O2-S-C6	110.51(11)	110.17
O3-S-C6	103.82(9)	97.24
C7-O3-S	121.86(14)	117.84
C19-O5-C22	117.7(2)	118.9
C2-C1-C6	119.0(2)	118.74
C1-C2-C3	121.8(3)	121.19
C2-C3-C4	118.0(2)	118.55
C2-C3-C23	121.3(3)	120.72
C4-C3-C23	120.7(3)	120.7
C5-C4-C3	121.6(2)	121.18

C4-C5-C6	119.0(2)	118.75
C1-C6-S	119.96(18)	119.16
C5-C6-S	119.39(19)	119.26
C5-C6-C1	120.6(2)	121.56
C8-C7-O3	121.9(2)	119.9
C12-C7-O3	116.5(2)	118.79
C12-C7-C8	121.4(2)	121.22
C7-C8-C9	118.5(2)	119.19
C8-C9-C10	122.0(2)	121.18
C9-C10-C11	117.2(2)	118
C9-C10-C13	123.3(2)	123.43
C11-C10-C13	119.5(2)	118.55
C12-C11-C10	121.8(2)	121.41
C7-C12-C11	119.1(2)	118.97
C14-C13-C10	129.1(2)	127.91
C13-C14-C15	122.2(2)	120.34
O4-C15-C14	119.4(3)	120.86
O4-C15-C16	120.3(2)	120.14
C16-C15-C14	120.3(2)	118.98
C17-C16-C15	123.8(2)	124.27
C21-C16-C15	119.2(2)	117.86

C21-C16-C17	117.0(2)	117.85
C18-C17-C16	121.2(2)	121.16
C17-C18-C19	120.2(2)	120.13
O5-C19-C18	115.3(2)	115.85
O5-C19-C20	125.0(2)	124.54
C20-C19-C18	119.7(2)	119.6
C21-C20-C19	119.4(2)	119.52
C20-C21-C16	122.4(2)	121.71

Carbonyl group (C=O) is an important functional group in our molecule, as it influences its NLO characteristics. Recent investigations showed that its bond lengths range from 1.23 Å to 1.22 Å, which is similar to our findings, the average bond length in benzene rings is 1.396 Å for experimental and 1.38 Å for theoretical structure, Sulfonate bond lengths vary between 1.455 Å for S=O and 1.6 Å for S-O.

Regarding bond angles, we registered for the C-O-C a 118.7°, the C-C-C bond angles in aromatic rings have an average computed angle of 120°, The O=C-C bond angles have an average of 120°, while bond angles surrounding sulfur range from 103° to 120°, all of these findings agree well with the literature [15-18].

In general we conclude that theoretical and experimental results are typically close to each other, with minor discrepancies linked to the fact that in the calculation, the molecule is considered as gas, while in the experimental, the molecules are solid crystals.

5.2.4 Vibrations analysis

To determine the functional groups and intermolecular interactions for the 4MPMS we calculated the vibration spectrum in the range 400-4000 cm^{-1}, the results are presented in figure V.8 and table V.4 and compared with the experimental results [14], to make calculations results more accurate, we multiply by a scaling factor [19] that adjust the overestimated vibrational

frequencies caused by approximations in electron correlation and the harmonic model. To correct this, a scaling factor of 0.96 is applied to align theoretical frequencies with experimental data. The corrected frequency This factor is widely used with the B3LYP functional and was applied in this study for vibrational frequency corrections of the chalcone derivative.
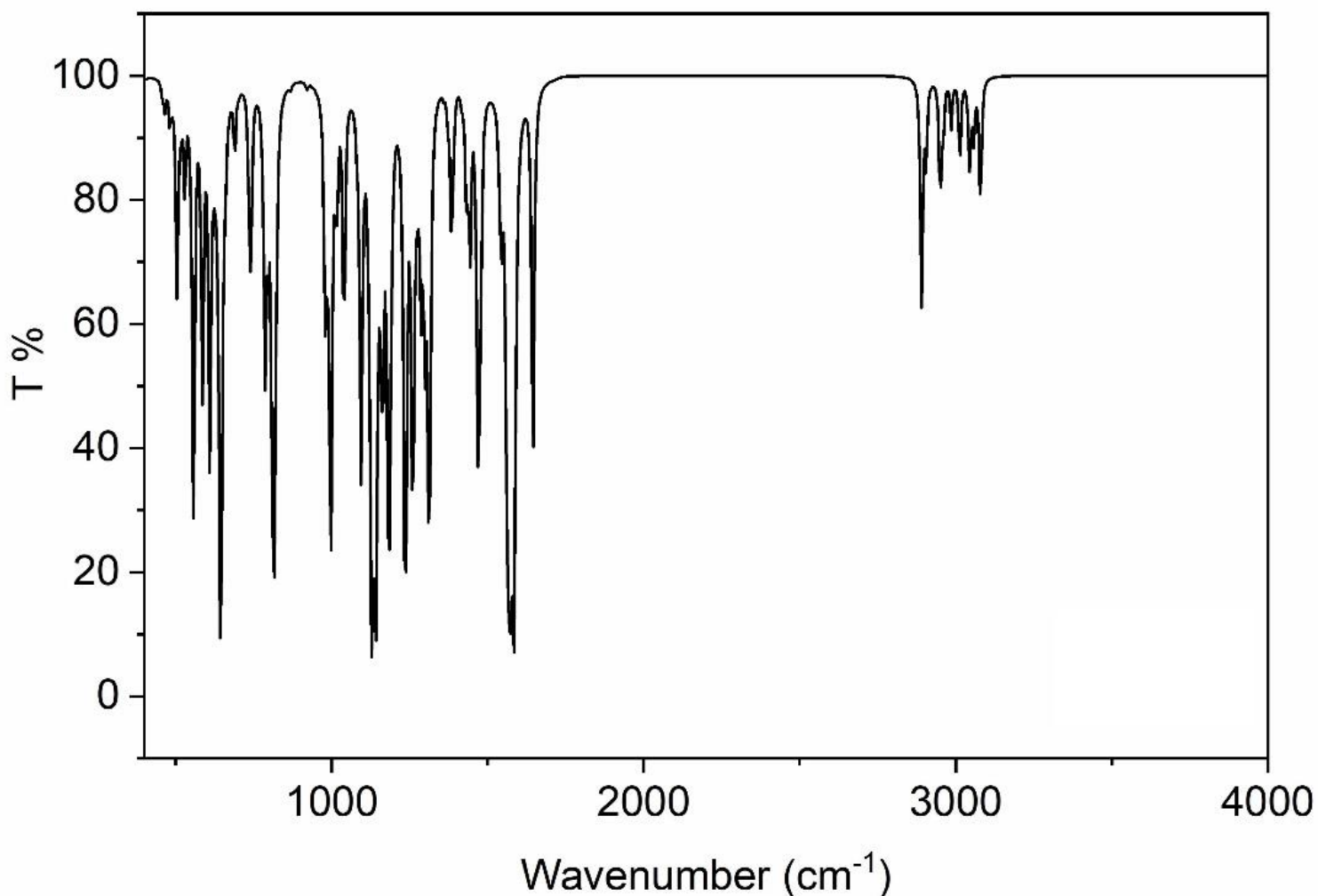
Figure V.8. Theoretical IR spectrum for 4MPSM calculated by B3LYP/6-311++G(d,p) level

Table V.4. Experimental and theoretical vibrational wavenumbers (cm^{-1}) for 4MPMS

FT-IR [14]	B3LYP/6-311++G(d,p)	IR intensity	Raman intensity	Assignment with PED analysis
	3081	6.35	233.0524	ν CH 93(%)
	3080	5.59	103.6861	ν CH 87(%)
	3079	17.76	23.0781	ν CH 86(%)
	3077	4.51	146.3084	ν CH 93(%)
	3077	3.11	10.9302	ν CH 91(%)
	3076	0.1734	9.9469	ν CH 96(%)
	3067	0.4644	48.5039	ν CH 85(%)
3062.3	3065	0.4431	39.7788	ν CH 96(%)
	3058	14.41	62.996	ν CH 93(%)
	3054	0.1547	14.449	ν CH 96(%)
	3047	5.95	71.6029	ν CH 93(%)
	3044	9.2	128.2137	ν CH 95(%)
	3043	10.41	109.7333	ν CH 96(%)
	3022	0.4711	28.3521	ν CH 98(%)
	3012	22.32	175.0867	ν CH 91(%)
	2986	11.93	69.5059	ν CH 99(%)
	2959	14.57	105.0435	ν CH 100(%)
2932.1	2950	32.43	74.9363	ν CH 100(%)

	2905	20.19	420.3453	ν CH 99(%)
	2891	70.5	205.0948	ν CH 91(%)
1661.1	1645	144.79	284.4238	ν CC 22(%) + OC 52(%)
1605	1583	360.08	468.0102	ν CC 21(%) + OC 10(%)
	1572	314.58	645.7628	ν CC 28(%)
	1571	35.95	125.7038	ν CC 31(%)
	1563	177.27	9488.5248	ν CC 13(%) + OC 17(%)
	1550	0.6608	7.5554	ν CC 51(%) + β CCC 10(%)
	1544	35.76	374.3198	ν CC 41(%)
	1538	10.19	578.4512	β CCC 10(%) + ν CC 43(%)
1501.1	1478	35.06	140.5226	β HCC 56(%)
	1471	162.15	6.7775	β HCC 66(%)
	1463	9.45	1.4537	β HCC 64(%)
	1444	50.03	16.688	β HCH 79(%) + γ HCOC 20(%)
	1434	9.74	18.2358	β HCH 76(%) + γ HCOC 16(%)
	1431	16.52	9.1611	β HCH 79(%) + γ HCCC 14(%)
	1430	7.91	18.7237	β HCH 65(%) + γ HCCC 11(%)
1417.4	1417	3.7	10.4502	β HCH 80(%)

	1389	13.33	11.6377	ν CC 40(%) + β HCC 14(%)
	1384	40.92	166.8891	ν CC 32(%) + β HCC 20(%)
	1373	7.53	0.2261	ν CC 37(%)
1360.3	1359	1.778	34.5661	β HCH 94(%)
	1312	225.83	332.6805	β HCC 33(%)
	1299	82.94	139.3251	ν CC 10(%) + β 38(%)
	1287	55.09	21.7054	ν CC 46(%)
	1284	11.13	1.0753	ν CC 58(%)
	1279	0.0895	0.1462	ν CC 21(%) + β HCC 70(%)
	1275	15.86	14.8021	ν CC 13(%) + β HCC 39(%)
	1267	11.73	18.5319	β HCC 35(%)
	1260	91.22	232.5773	ν CC 21(%)
	1259	97.03	43.1323	ν SO 68(%)
	1236	300.69	60.8537	ν OC 44(%)
	1187	136.81	69.3788	ν CC 33(%) + β HCC 17(%)
	1182	134.01	539.8846	ν CC 32(%)
	1180	9.33	105.3319	ν CC 37(%)
	1164	100.49	23.7679	β HCC 19(%) + ν 18(%)
	1159	24.31	4.3092	β HCC 69(%)
1148.8	1154	6.01	2.6704	γ HCOC 56(%) + β HCH 16(%)

	1141	331.49	125.322	β HCC 44(%)
	1129	393.81	900.1926	ν OC 17(%) + β HCC 34(%)
	1120	0.6438	2.7284	β HCH 30(%) + γ HCOC 69(%)
	1094	130.31	20.0276	ν SO 51(%) + SC 11(%)
	1093	8.96	0.237	ν CC 15(%) + β HCC 61(%)
1091.7	1093	8.96	2.0868	ν CC 26(%) + β HCC 46(%)
	1081	5.77	4.7529	ν CC 29(%) + β HCC 34(%)
	1040	80.55	50.1741	ν CC 34(%) + SO 35(%)
	1019	18.02	0.6228	γ HCCC 55(%) + β HCH 16(%)
	1014	18.72	29.1029	ν OC 68(%)
	997	209.73	323.7467	ν CC 45(%)
	991	6.55	0.8432	β CCC 66(%)
	990	14.27	15.9515	β CCC 53(%)
	982	27.55	3.6392	γ HCCC 90(%)
	978	53.25	123.7915	β CCC 55(%) + ν CC 10(%)
	970	0.1154	0.2901	γ HCCC 48(%) + β HCH 20(%)
	953	0.0275	0.0136	γ HCCC 65(%) + HCCS 22(%)
	950	0.6852	1.6616	γ HCCC 81(%)

	937	0.2421	0.3368	γ HCCC 87(%)
	937	0.2566	0.2072	γ HCCC 74(%)
	924	0.285	0.9085	γ HCCC 64(%)
	921	1.62	0.8381	γ HCCC 35(%) + CCCC 34(%)
874.3	869	1.51	22.8755	β CCC 22(%)
	857	0.2334	12.9115	γ HCCC 56(%) + τ OCCC 12(%)
823	826	10.15	1.8003	γ HCCC 14(%) + τ CCOC 12(%)
	817	3.74	0.6297	γ HCCC 76(%) + HCCS 22(%)
	816	200.26	40.3148	ν CC 27(%) + OC 17(%)
	810	113.17	5.6181	γ HCCC 10(%) + τ OCCC 12(%)
	797	34.02	2.8482	γ HCCC 63(%)
	796	0.1196	0.2242	γ HCCC 95(%)
	789	0.1223	0.8918	γ HCCC 99(%)
	786	92.42	23.1769	ν CC 11(%)
	781	1.93	8.2347	ν CC 14(%) + β 27(%)
	735	18.79	87.3344	γ CCCC 12(%) + τ OCCC 14(%)
708.2	703	0.845	2.4548	γ CCCC 45(%)

	689	16.84	8.8188	γ CCCC 60(%) + τ CCCC 10(%)
659.5	660	10.39	1.0228	γ CCCC 24(%) + τ OCCC 28(%)
	644	376.13	150.5793	ν CC 12(%) + SC 17(%)
	628	8.33	69.131	β CCC 56(%)
	621	10.14	7.7397	β CCC 36(%)
	621	0.1855	6.0046	β CCC 71(%)
	610	137.7	379.3931	ν SO 35(%)
	587	103.66	29.9998	β OCC 10(%) + CCC 22(%)
	529	29.6	19.116	τ OCOS 23(%)
	516	8.68	6.2129	β CCC 19(%)
	504	61.18	0.7382	β OSO 20(%) + τ CCOC 16(%)
	491	2.66	0.5164	γ CCCC 11(%) + τ OCCC 29(%)
	482	10.98	13.8435	β COC 15(%) + OCC 10(%)
	466	6.61	2.5875	β OSO 20(%) τ OCOS 30(%)
	458	3.89	44.5582	τ CCCC 21(%)
	451	0.2055	24.2259	β OSO 33(%)
	406	0.2396	0.2925	γ HCCC 14(%) + γ CCCC 63(%)

| 404 | 0.1753 | 1.611 | γ CCCC 32(%) + γ CCCO 24(%) |
| 400 | 0.2715 | 7.5394 | γ CCCC 30(%) |

IR spectra show two bands: the first one is a high frequency near 500-1600 cm^{-1} associated mostly with CO, CC, SO, and SC vibrations while the second band is in a wide frequency range (2900-3200cm^{-1}) related to CH stretching.

According to Table V.4 the C-C and C=C stretching is reported in the range 1284 - 1550 cm^{-1} and 1593-1629 cm^{-1} while experiment indicated the C=C in 1605 cm^{-1}, in-plane, and out-of-plane bending are reported also with different Potentiel Energy Distribution (PED) contribution in range 400-1200 cm^{-1}, carbonyl groups(C=O) stretching, on the other hand, occurred in the range 1014 - 1645 cm^{-1} along with other types of vibrations (bending and torsion) in the range 466-1120 cm^{-1}, while the sulfur and its related atoms vibrations occurred with low PED (11%-35%) contribution, where the S-C stretching was registered at 1094 cm^{-1}, the S=O in the range 1040 – 1259 cm^{-1} and finely the S-O at the 610 cm^{-1}, the provided experimental results did not mention any sulfur vibrations.

Regarding the second band vibrations that represent the C-H vibrations, theoretical calculations showed a stretching in the range 2891-2986 cm^{-1} with high PED contribution, other types of C-H vibrations occurred between 789-1478 cm^{-1} which define the in-plane and out-of-plane bending.

5.2.5 ^{1}H and ^{13}C NMR analysis

To examine the chemical properties and the way the structure is formed for the studied material, we measured the resonance frequency of nuclear magnetic moments in an applied magnetic field, results are presented in Table V.5 along with the provided experimental results [14]. According to Table V.5, the ^{1}H NMR chemical shifts for the methoxyl group (OCH$_3$) protons are calculated at 4.1983, 3.8948, and 3.8813 ppm, while the experimental result at 3.89 ppm, benzene rings ^{1}H NMR signals are calculated at 8.7363-7.1778 ppm, while ^{1}H NMR signals for H-C-C-H (H13 and H14) are calculated at 8.3468 and 8.1631 ppm, the highest chemical shifts for

H5 (8.24 ppm), H1 (8.17 ppm), and H9 (8.49 ppm) are related to being near atoms with high electronegativity. Regarding ^{13}C NMR signals for all aromatic C atoms are calculated at 115.44 - 172.99 ppm, and the highest chemical shift is calculated for C15 with 191.95 ppm, agreeing with the literature, studies reprted methyl C atoms NMR signals at 24.6 ppm, while the calculated NMR signal for the methyl group C atom (C23) is at 24.16 ppm. The other methyl group C atom (C22) gives an NMR band at 57.4671 ppm due to the electronegativity of the O atom.

^{13}C NMR experimental results were not mentioned.

Table V.5 ^{1}H and ^{13}C NMR isotropic shifts (ppm) for 4MPMS

H/C	B3LYP/6-311++G(d,p)	Experimental
H21	8.7363	8.034
H9	8.4924	8.012
H13	8.3468	7.735
H17	83,197	7.714
H5	8.2451	7.701
H1	8.1712	7.57
H14	8.1631	7.5
H11	7.8574	7.549
H5	7.8434	7.461
H8	7.8434	7.339
H2	7.7722	7.319
H4	7.7418	7.264
H12	7.5977	7.047

H18	7.2773	7.026
H20	7.1778	6.995
H22C	4.1983	3.896
H22A	3.8948	3.896
H22B	3.8813	3.896
H23B	2.7944	2.46
H23C	2.4805	2.46
H23A	2.4736	2.46
C15	191.958	-
C19	172.998	-
C7	159.73	-
C3	156.582	-
C13	153.175	-
C6	145.083	-
C11	142.541	-
C10	141.802	-
C21	139.652	-
C16	137.86	-
C17	137.025	-
C2	136.772	-
C4	136.772	-

C5	134.831	-
C1	134.647	-
C9	132.82	-
C12	132.714	-
C8	132.45	-
C14	124.57	-
C18	123.108	-
C20	115.44	-
C22	57.4671	-
C23	24.1602	-

5.2.6 Electrical Properties

5.2.6.1 Frontier Molecular Orbital Analysis

The frontier molecular orbitals are defined as the high occupied molecular orbitals (HOMO) and the low unoccupied molecular orbitals (LUMO), that work on determining the electrical and optical properties of the studied materials, by calculating the energy gap that leads to predicting the chemical stability and polarizability of the material. As presented in Figure V.9 which illustrates the frontier molecular orbitals of the 4MPMS system, calculations reported that the charges are concentrated near aromatic rings and oxygen atoms in both HOMO and LUMO, the HOMO and LUMO energies for the 4MPMS are determined to be -6.4382 and -2.4139 eV, respectively, and the resulted energy gap is found to be 4.0241 eV.
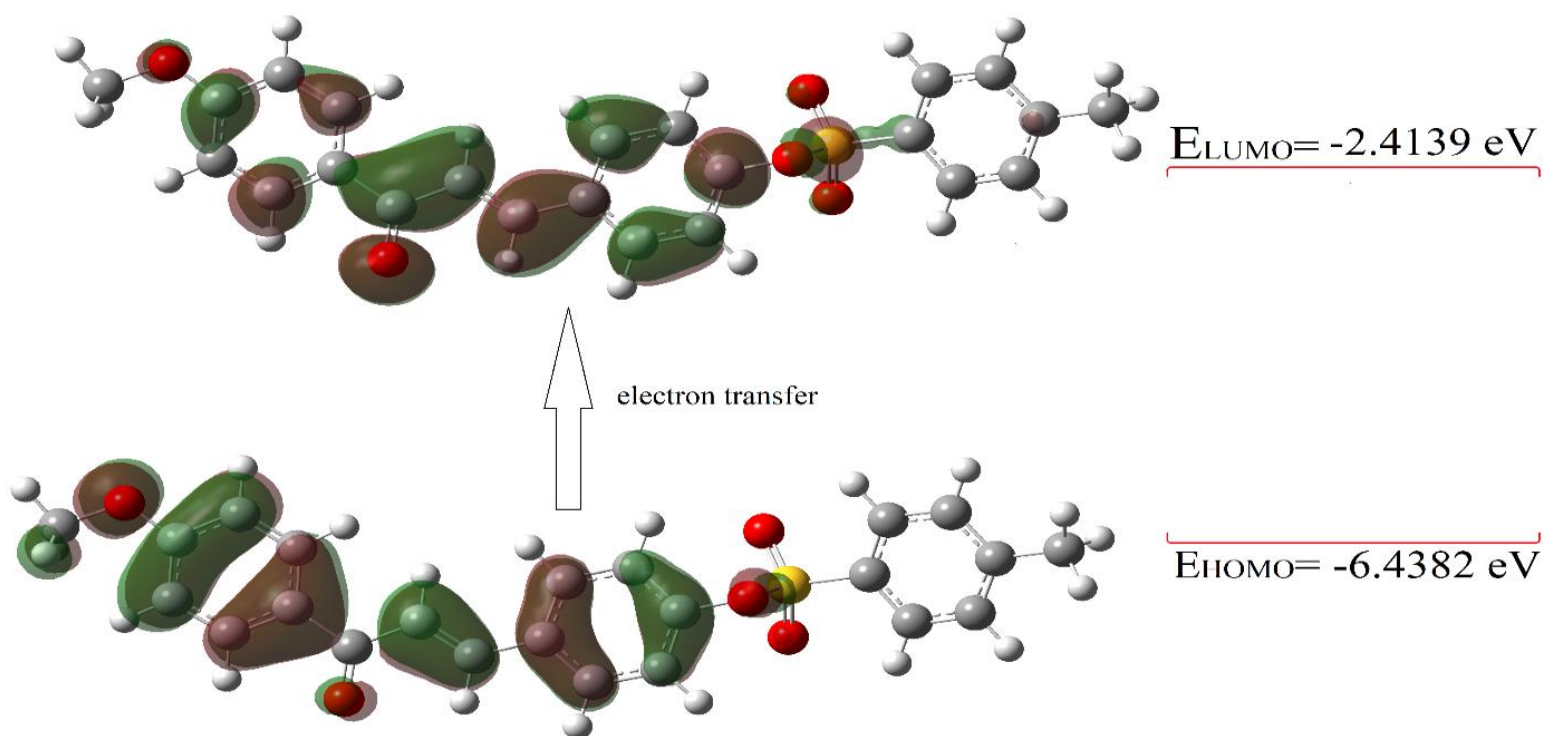
Figure V.9 The molecular orbital frontiers and their energies calculated for 4MPMS by

B3LYP/6-311++G(d,p)

To investigate the chemical properties of the 4MPMS, the quantum chemical parameters, such as the ionization potential (IP), electron affinity (EA), electronegativity ($\Box$), hardness (η), chemical potential (P), and softness (S), are calculated through molecular orbital frontier energies. Table V.6 displays the obtained $\Box$, η, and S findings.

Table V.6 Molecular orbital Frontier energies, electronegativity ($\Box$), hardness (η), and softness (S) for 4MPMS obtained by B3LYP/6–311++G(d,p) level.

Parameters	4MPMS
E_{HOMO}(eV)	-6.4382
E_{LUMO}(eV)	-2.4139
ΔE(eV)	4.0241
$\Box$(eV	4.42605
η(eV)	1.9996
S(eV^{-1})	0.25

Based on these findings, we conclude that the 4MPMS is a more polarizable, chemically soft, and reactive molecule.

5.2.6.2 Molecular Electrostatic Potential (MEP) Analysis

To study and visualize the electrical charge distribution of the 4MPMS, we calculated the Molecular Electrostatic Potential (MEP) surface in the range -0.06248, 0.06248 a.u as presented in Figure V.10, as it shows that the C=O group contains the most negatively charged area, followed by the SO_3 group, however, the methyl group, C-CH_3, O-CH_3 groups and the aromatic H atoms, have the most positive charged area, regarding these results we conclude that, C=O and SO_3 groups are the most likely positions that could participate in chemical reactions.

-0.06246 a.u   **0.06246 a.u**
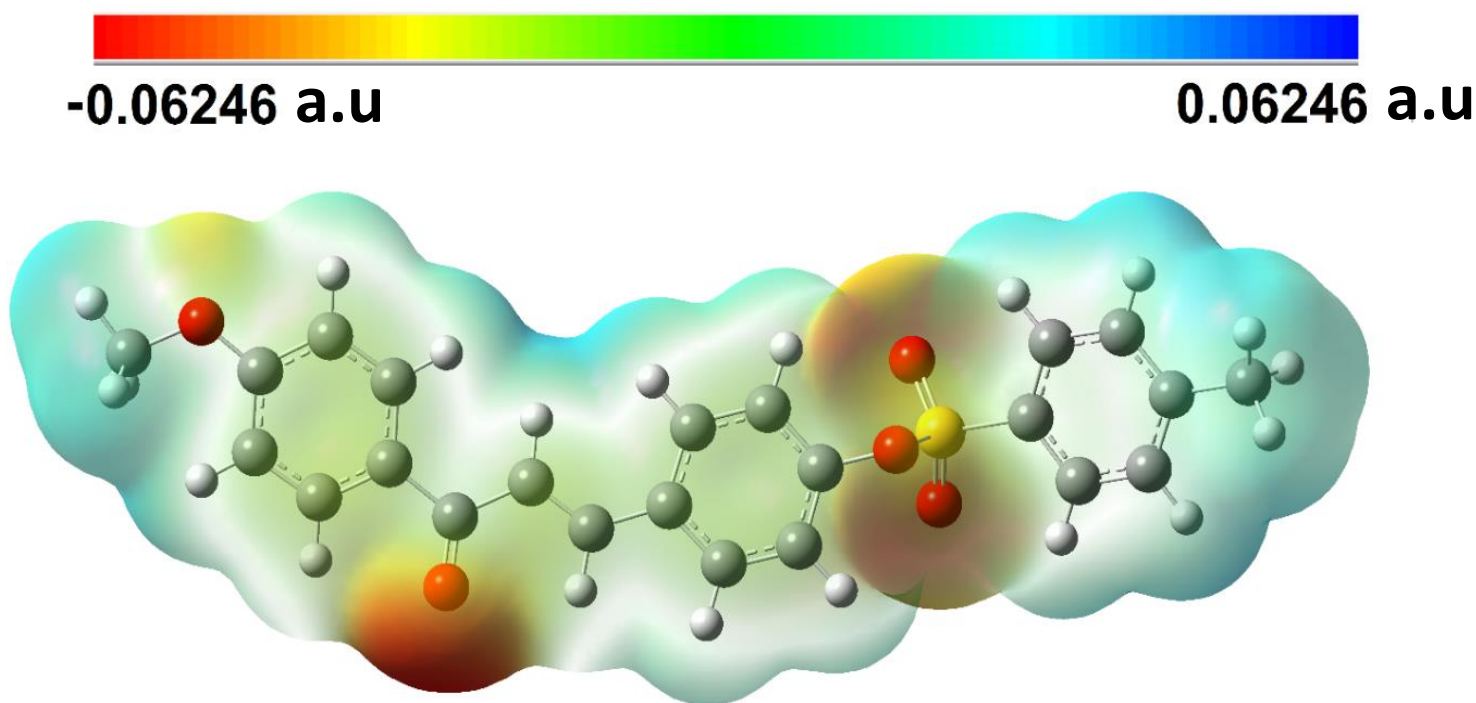
Figure V.10 MEP surfaces for 4MPMS calculated by B3LYP/6-311++G(d,p)

5.2.7 Nonlinear Optical Properties

A theoretical study of the 4MPMS system NLO response, through the calculation of the dipole moment μ, polarizability (α), the anisotropy of polarizability ($\Delta\alpha$), first-order

hyperpolarizability (β) and second-order hyperpolarizability (γ) in the static (λ=0 nm) and dynamic state (λ=532 nm) results are presented in Table V.7

For the title molecule, μ is found to be 4.56088 Debye, α is 5.3067×10^{-23} esu (static) and 6.2319×10^{-23} esu (dynamic), the $\Delta\alpha$ is calculated at 5.5224×10^{-23} and 7.7171×10^{-23} in the static and dynamic state respectively, **w**hile, $\beta(0,0,0)$, $\beta(-w,w,0)$, and $\beta(-2w,w,w)$ parameters are 16.240×10^{-30}, $82.240 \text{x} \times 10^{-30}$, 213.97×10^{-30} esu, respectively, and finely the second-order hyperpolarizability (γ). The $\gamma(0,0,0,0)$, $\gamma(-w,w,0,0)$, and $\gamma(-2w,w,w,0)$ parameters results are 213.77×10^{-36}, 943.74×10^{-36} and 485.90×10^{-36} esu respectively.

Regarding all these results we conclude that the NLO characteristics of the 4MPMS molecule are much higher than those of the Urea molecule, which indicates that the title molecule has strong NLO capabilities.

Table V.7 Static and frequency-dependent (λ=532 nm) α (esu), $\Delta\alpha$ (esu), β (esu) and γ (esu) for 4MPMS

Parameter	4MPMS
μ	4.56088
$\alpha(0.0)$	5.3067×10^{-23}
$\Delta\alpha(0.0)$	5.5224×10^{-23}
$\alpha(-\omega.\omega)$	6.2319×10^{-23}
$\Delta\alpha(-\omega.\omega)$	7.7171×10^{-23}
$\beta(0;0.0)$	16.240×10^{-30}
$\beta(-\omega;\omega.0)$	82.240×10^{-30}
$\beta(-2\omega;\omega.\omega)$	213.97×10^{-30}
$\gamma(0;0.0.0)$	213.77×10^{-36}
$\gamma(-\omega;\omega.0.0)$	943.74×10^{-36}
$\gamma(-2\omega;\omega.\omega.0)$	485.90×10^{-36}

5.4 References

1   Wu, R., & Freeman, A. J. (1992). Spin density at the Fermi level for magnetic surfaces and overlayers. Physical review letters, 69(19), 2867.

2   Boukelkoul, M., Kharoubi, M., & Haroun, A. (2008). Magnetic and magneto-optical properties of ultrathin films of iron epitaxied on iridium (001). Canadian Journal of Physics, 86(12), 1421-1426.

3   Cortona, P., Doniach, S., & Sommers, C. (1985). Relativistic extension of the spin-polarized local-density-functional theory: Study of the electronic and magnetic properties of the rare-earth ions. Physical Review A, 31(5), 2842.

4   Boukelkoul, M. (2018). Propriétés magnéto-optiques des couches ultraminces et des slabs à base de métaux de transition (Doctoral dissertation).

5   Strange, P., Staunton, J., & Gyorffy, B. L. (1984). Relativistic spin-polarised scattering theory-solution of the single-site problem. Journal of Physics C: Solid State Physics, 17(19), 3355.

6   Szotek, Z., Temmerman, W. M., & Winter, H. (1993). Application of the self-interaction correction to transition-metal oxides. Physical Review B, 47(7), 4029.

7   Britannica, T. Editors of Encyclopaedia (2024, March 5). rhodium. Encyclopedia Britannica. https://www.britannica.com/science.

8   Ouarab, N., Haroun, A., & Baadji, N. (2016). Structural changes induced spin-reorientation of ultrathin Mn films grown on Ag (001). Journal of Magnetism and Magnetic Materials, 419, 5-16.

9   Kaneko, T., Kawazoe, Y., & Uwatoko, Y. (Eds.). (2014). Numerical Data and Functional Relationships in Science and Technology: New Series. Physical Chemistry. High Pressure Materials Properties. Magnetic Properties of D-elements, Alloys and Compounds Under Pressure. Springer

10   Boukelkoul, M., & Haroun, A. (2011). Structural, magnetic and magneto-optical properties of ultrathin films of nickel on iridium (001). Thin solid films, 520(3), 1109-1114.

11   Khan, M. U., Ibrahim, M., Khalid, M., Jamil, S., Al-Saadi, A. A., & Janjua, M. R. S. A. (2019). Quantum chemical designing of indolo [3, 2, 1-jk] carbazole-based dyes for highly efficient nonlinear optical properties. Chemical Physics Letters, 719, 59-66.

12   Naik, V. S., Patil, P. S., Wong, Q. A., Quah, C. K., Gummagol, N. B., & Jayanna, H. S. (2020). Molecular structure, linear optical, second and third-order nonlinear optical properties of two non-centrosymmetric thiophene-chalcone derivatives. Journal of Molecular Structure, 1222, 128901.

13   Yang, Y., Wu, X., Jia, J., Shen, L., Zhou, W., Yang, J., & Song, Y. (2020). Investigation of ultrafast optical nonlinearities in novel bis-chalcone derivatives. Optics & Laser Technology, 123, 105903.

14   Vinaya, P. P., Prabhu, A. N., Bhat, K. S., & Upadhyaya, V. (2019). Synthesis, growth and characterization of a long-chain π-conjugation based methoxy chalcone derivative single crystal; a third order nonlinear optical material for optical limiting applications. Optical Materials, 89, 419-429..

15   Süleymanoğlu, N., Ustabaş, R., Eyduran, F., Direkel, Ş., Ünver, Y., & Kahriman, N. (2021). (2E)-3-(1-benzothiophen-2-yl)-1-(4-hydroxyphenyl) prop-2-en-1-one: Synthesis, Characterization (IR, NMR and UV-Vis) DFT Study and Antimicrobial Activity. Journal of the Chemical Society of Pakistan, 43(6).

16   Fun, H. K., Patil, P. S., Jebas, S. R., & Dharmaprakash, S. M. (2008). (E)-3-(2-Chlorophenyl)-1-(2-furyl) prop-2-en-1-one. Acta Crystallographica Section E: Structure Reports Online, 64(8), o1467-o1467.

17   Parol, V., Prabhu, A. N., Taher, M. A., Naraharisetty, S. R. G., Lokanath, N. K., & Upadhyaya, V. (2020). A third-order nonlinear optical single crystal of 3, 4-dimethoxy-substituted chalcone derivative with high laser damage threshold value: a potential material for optical power limiting. Journal of Materials Science: Materials in Electronics, 31, 9133-9150.

18   Patel, U. H., Gandhi, S. A., Barot, V. M., & Patel, M. C. (2012). 3-(2-Chloro-3-hydroxy-4-methoxyphenyl)-1-(4, 5-dimethoxy-2-methylphenyl) prop-2-en-1-one. Acta Crystallographica Section E: Structure Reports Online, 68(10), o2926-o2927.

19   Chermette, H. (1998). Density functional theory: a powerful tool for theoretical studies in coordination chemistry. Coordination chemistry reviews, 178, 699-721.

General conclusion

In this dissertation, we investigated two distinct systems, each with its unique set of properties. The first system involved studying the structural, magnetic, and magneto-optical properties of Nickel ultra-thin films deposited on a Rhodium substrate using the SPR-LMTO ASA program. The structural properties of the Nin/Rh(001) (n = 1, 2, 3) system were obtained through a relaxation process, optimizing the total energy as a function of the distance between atomic planes. Equilibrium was achieved for a body-centered tetragonal (BCT) structure with a tetragonal ratio of c/a = 1.18 and a calculated lattice mismatch of 7%.

Magnetic properties were explored by calculating the magnetic moments. Nickel films exhibited magnetic moment values higher than bulk Nickel, similar to those of free Nickel surfaces, due to the compressed state of the Ni layers with interplane distances smaller than those of bulk Nickel. The Rhodium layers showed two distinct behaviors: the Rh layer adjacent to Nickel exhibited ferromagnetic behavior with a higher magnetic moment than bulk Rhodium, while some interplane layers showed antiferromagnetic behavior, maintaining the paramagnetic nature of bulk Rhodium. These results were confirmed by Density of State (DOS) curves, indicating overall ferromagnetic coupling in the system.

Magneto-optical properties were studied by calculating the polar Kerr effect (P-MOKE) across an extended energy range up to 10 eV. The system showed alternating positive and negative Kerr rotations due to transitions between localized states, primarily involving s→p, p→s, and d→p transitions as identified from DOS spectra. We conclude that the Nin/Rh(001) system is well-suited for magneto-optical applications, particularly in sensors and storage devices.

The second system is a theoretical study of a synthesized organic chalcone derivative, 4-[(1E)-3-(4-methoxyphenyl)-3-oxoprop-1-en-1-yl]phenyl   4-methylbenzene-1-sulfonate   (4MPMS). Geometry optimization was performed, followed by the calculation of electronic and optical properties using the GAUSSIAN program at the B3LYP/6-311++G(d,p) level. Frontier molecular orbitals and MEP surface analysis, along with dipole moment calculation, revealed a low energy gap and variable charge distribution, giving the molecule high charge mobility, a beneficial trait for Nonlinear Optical (NLO) applications. The presence of donor-acceptor groups linked by π-bridges further enhanced its NLO properties.

Static and dynamic NLO properties, including polarizability (α), anisotropy of polarizability ($\Delta\alpha$), first-order hyperpolarizability (β), and second-order hyperpolarizability (γ), were calculated, along with the second harmonic generation (SHG) values. In the static state, we obtained values of 5.3067×10^{-23} esu, 5.5224×10^{-23} esu, 16.24×10^{-30} esu, and 213.77×10^{-36} esu, while in the dynamic state, the values were higher: 6.2319×10^{-23} esu, 7.7171×10^{-23} esu, 82.24×10^{-30} esu, 213.97×10^{-30} esu (SHG), 943.74×10^{-36} esu, and 485.9×10^{-36} esu (SHG). These values were compared to urea, and the dynamic NLO properties were notably higher.

Spectroscopic (IR and NMR) analysis confirmed the consistency between the theoretically fabricated and experimentally synthesized molecules. In conclusion, the 4MPMS molecule demonstrates excellent potential for NLO applications due to its favorable properties, low cost, and diverse benefits.

Appendix

Appendix A

A.1 Kubo formalism

The behavior of a medium in the presence of electromagnetic waves is described by its electrical conductivity or dielectric constant. Both depend on the frequency of the electromagnetic wave. Hence the need to find a link between these parameters and changes in electronic states, to understand how the interaction of electromagnetic waves with solids.

The simplest way to approach this problem is to use the Kubo formalism, in which conductivity is interpreted in terms of interband transitions. Consider a solid made up of N electrons. In the presence of a vector potential and a scalar potential, the Hamiltonian of a system is written as [1]

$$H = \frac{1}{2m} \sum_{i=1}^{N} \left(p_i \frac{e}{c} A(r_i) \right)^2 + \sum_{i=1,k=1}^{N,M} V_k(r_i - R_k) + \frac{1}{2} \sum_{i=1,k=1}^{N,M} \frac{e^2}{|r_i - r_j|} \qquad \text{(A-1)}$$
$$- \sum_{i=1}^{N} e\Phi(r_i)$$

The first term expresses the coupling between electromagnetic waves (described by the vector potential), and the electrons described by the moments p_i, position r_i and the second term defines the interaction between ions and electrons. It is given by the potential V_k. The third term represents, the electron-electron interaction and the last term represents the external scalar potential. In general, the Hamiltonian is written as:

$$H = H_0 + H_{int} \qquad \text{(A-2)}$$

H_0 is the Hamiltonian in the absence of $A(r)$ and $\Phi(r)$

$$H_0 = \frac{1}{2m} \sum_{i=1}^{N} p_i^2 + \sum_{i=1,k=1}^{N,M} V_k(r_i - R_k) + \frac{1}{2} \sum_{i=1,k=1}^{N,M} \frac{e^2}{|r_i - r_j|} \qquad \text{(A-3)}$$

H_{int} describes the system's interaction with $A(r)$ and $\Phi(r)$ and it is given by the expression:

$$H_{int} = \frac{e}{2mc} \sum_{i=1}^{N} [p_i A(r_i) + A(r_i)p_i]^2 - \sum_{i=1}^{N} e\Phi(r_i) \qquad \text{(A-4)}$$

In this equation, we have neglected the A^2 terms.

The electrical charge density is given by:

$$J(r) = -\frac{e}{2} \sum_{i=1}^{N} [v_i \delta(r - r_i) + \delta(r - r_i)v_i] \qquad \text{(A-5)}$$

In the non-relativistic limit, velocity can be written as :

$$v = \frac{p}{m} + \frac{eA}{mc} \qquad \text{(A-6)}$$

Therefore, the equation A-5 is expressed as:

$$J(r) = -\frac{e}{2} \sum_{i=1}^{N} [p_i \delta\{r - r_i\} + \delta\{r - r_i\}p_i] - \frac{e^2}{mc} \sum_{i=1}^{N} A(r_i)\delta\{r - r_i\} \qquad \text{(A-7)}$$

The first expression is the paramagnetic current and the second is the diamagnetic current.

Using the A-5 equation of electrical current density, for a transversal field $\Phi(r) = 0$, the interaction term in the expression for H is given by

$$H_{int} = -\frac{1}{c} \int J(r)A(r)dr \qquad \text{(A-8)}$$

In the k-space, this term is written as

$$H_{int} = -\frac{1}{c} J(k)A(k) \qquad \text{(A-9)}$$

According to Fermi's rule, the transition probability per unit of time and unit of volume of the initial state $|n\rangle$ to the final state $|n'\rangle$ is

$$W_{nn'} = \frac{2\pi}{\hbar^2}|\langle n'|H_{int}|n\rangle|^2\delta\{\omega - \omega_{nn'}\} \tag{A-10}$$

$\hbar\omega_n$ and $\hbar\omega_{n'}$ are the energies of the initial and final states respectively.

The energy absorbed per unit of time and unit volume is written as

$$P = \hbar\omega W = |A(k)|^2\sum_n\frac{\omega}{\hbar c^2}\int dt|\langle n|J(k,0)J^*(k,t)|n\rangle|e^{-i\omega t} \tag{A-11}$$

Considering that the vector potential is given by $E = \frac{i\omega}{c}A$ and $P = \sigma E^2$. We arrive to the Kubo-Greenwood formula [2,3]

$$\sigma_{\alpha\beta}(\omega) = \frac{\pi e^2}{\hbar^2\omega}\sum_k\sum_{nn'}\frac{f(\varepsilon_{nk}) - f(\varepsilon_{n'k})}{\omega_{nn'}(k)}\frac{M_{nn'}^\alpha(k)M_{nn'}^\beta(k)}{\omega - \omega_{nn'}(k) + i\gamma} \tag{A-12}$$

$f(\varepsilon_{nk})$ is the Fermi function, $\hbar\omega_{nn'} = \varepsilon_{nk} - \varepsilon_{n'k}$ is the energy difference between Kohn-Sham levels, and γ is the inverse of the relaxation time. $M_{nn'}^\alpha$ are the matrix elements of optical transitions.

In the relativistic case, the current density vector is given by

$$j = -ec\alpha \tag{A-13}$$

With α Dirac operator so $M_{nn'}$ is defined as

$$M_{nn'} = \langle\Psi_n^k|c\alpha|\Psi_{n'}^k\rangle \tag{A-14}$$

Ψ_n^k is the four-component wave function.

A.2 Drude-Sommerfeld Theory

For metals, the components of the optical conductivity tensors, are given by the sum of the interband and intraband contribution [4]. In the optical domain and for low photon energies, the intraband contribution is dominant

From equation A-12, we can see that the expression of optical conductivity is a double sum, one for interband transitions $(n \neq n')$ and the other on intraband transitions $(n = n')$ energy bands, in other words, one describes the contribution, the conductivity equation then takes the following form

$$\sigma_{\alpha\beta}(\omega) = \sigma_{\alpha\beta}^{inter}(\omega) + \sigma_{\alpha\beta}^{intra} \tag{A-15}$$

In the Drude-Sommerfeld approach, the metal is considered as a classical gas in which the electron performs a diffusive motion. In the presence of an electric field E, the equation of motion is given by [5].

$$\frac{d}{dt}\langle p \rangle = -\frac{\langle p \rangle}{\tau_D} - eE \tag{A-16}$$

τ_D relaxation time.

The electric current density is given by

$$j = -Ne\frac{p}{m} \tag{A-17}$$

N charge density, while m and e represent the mass and charge of the electron

For a given $p = m\frac{dr}{dt}$ the solution to equation A-16 gives the expression for the conductivity as [6]

$$\hat{\sigma}(\omega) = \frac{Ne^{2\tau_D}}{m}\frac{1}{1 - i\omega\tau_D} = \frac{\omega_p^2}{4\pi\left[\frac{1}{\tau_D - i\omega}\right]} \tag{A-18}$$

With ω_p plasma frequency, it is given by

$$\omega_p^2 = \frac{4\pi e^2}{m^2\Omega}\sum_{nk}\delta(\varepsilon_{nk} - E_F)|M_{nn'}|^2 \tag{A-19}$$

E_F is Fermi energy and Ω is the atomic volume

The relaxation time parameter $\gamma_D = \frac{1}{\tau_D}$ from the Drude-Sommerfeld expression is different from the equation A-16. This is an intrinsic parameter that differs from one metal to another.

A.3 Selection Rules

The DOS plays an important role in estimating a material's electrical conductivity, magnetic behavior, and optical absorption when interacted by photons that leads to indicating the number of electronic states available at each energy level for electrons to occupy. On the other hand electromagnetic radiation is considered within the classical framework so we use the potential vector $A_{q\lambda}(r)$ to represent photons with a wave vector $\overrightarrow{(q)}$ and polarization λ. The operator corresponding to the electron-photon interaction is given by[7,8]

$$\chi_{q\lambda} = -\frac{1}{c}J.A_{q\lambda}(r) = -\frac{1}{c}J.\hat{a}_{\lambda}Ae^{iqr} \tag{A-20}$$

Where J is the current density operator

$$j_{el} = -ec\alpha \tag{A-21}$$

The polarization vector in equation A-20 is real for linearly polarized photons $\lambda = (x, y, z)$ For q along the z axis, the complex polarization vector is given by

$$\hat{a}_{\lambda} = \frac{1}{\sqrt{2}}\begin{pmatrix} 1 \\ \pm i \\ 0 \end{pmatrix} \tag{A-22}$$

It represents the left (right) circular polarization of the radiation, or, similarly, light with positive (or negative) helicity. In the optical frequency system generally we assume that the vector potential amplitude varies slowly on the microscopic scale. So we can limite the development of the exponential factor in Taylor series on the first term

$$e^{iqr} = 1 + iqr - \frac{1}{2}(qr)^2 + \cdots \tag{A-23}$$

and this means that only the first interaction of the electric dipole is considered in equation A-20. to becom[9]

$$(q.r)(\alpha.\hat{a}_{\lambda}) = \frac{1}{2}[(q.r)(\alpha.\hat{a}_{\lambda}) - (q.\alpha)(r.\hat{a}_{\lambda})]$$
$$+ \frac{1}{2}[(q.r)(\alpha.\hat{a}_{\lambda}) + (q.\alpha)(r.\hat{a}_{\lambda})] \tag{A-24}$$

we can see that it represents the two interactions, of the electric dipole and the magnetic quadrupole, Based on the SPR-LMTO method, and the corresponding expression A-20 for the electron-photon interaction, matrix elements of the form[8]

$$M_{q\lambda}^{nn'} = \langle \Phi_n | X_{q\lambda} | \Phi_{n'} \rangle \tag{A-25}$$

where $\Phi_{n(n')}(r, E_{n(n')})$ are the band wave functions, initial (*n*) and final (*n'*), which can be written as a sum of partial wave functions $\Phi_\Lambda(r, E)$ with a unique spin-orbital character Λ

To estimate the matrix elements $M_{q\lambda}^{\Lambda\Lambda'}$, it is therefore sufficient to consider only those elements concerning the functions $\Phi_\Lambda(r, E)$. Adopting the electric dipole approximation and keeping *ec* a constant factor the matrix elements can be written as follows[8]

$$M_{q\lambda}^{\Lambda\Lambda'} = \langle \phi_\Lambda | \boldsymbol{\alpha}.\widehat{\boldsymbol{a}}_\lambda | \phi_{\Lambda'} \rangle = i\left[\boldsymbol{R}_1^{\Lambda\Lambda'} A_\lambda^{\Lambda-\Lambda'} - \boldsymbol{R}_2^{\Lambda\Lambda'} A_\lambda^{-\Lambda\Lambda'} \right] \tag{A-26}$$

with matrix elements

$$\boldsymbol{R}_1^{\Lambda\Lambda'} = \int r^2 dr \, g_\lambda(r, E_\Lambda) f_{\Lambda'}(r, E_{\Lambda'}) \tag{A-27}$$

$$\boldsymbol{R}_2^{\Lambda\Lambda'} = \int r^2 dr \, f_\Lambda(r, E_\Lambda) g_{\Lambda'}(r, E_{\Lambda'}) \tag{A-28}$$

and angular

$$A_\lambda^{\Lambda\Lambda'} = \langle \chi_\Lambda | \boldsymbol{\alpha}.\widehat{\boldsymbol{a}}_\lambda | \chi_{\Lambda'} \rangle \tag{A-29}$$

The radial functions, $g_\lambda(r, E_\Lambda)$ and $f_{\Lambda'}(r, E_{\Lambda'})$ and angular χ_Λ are defined by equation 2.83. For the various polarization states λ, these turn out to be

$$A_\pm^{\Lambda\Lambda'} = 2C\left(l\frac{1}{2}j; \mu \mp \frac{1}{2}, \pm\frac{1}{2} \right) C\left(l'\frac{1}{2}j'; \mu \pm \frac{1}{2}, \mp\frac{1}{2} \right) \delta_{l-l';\pm1} \delta_{\mu-\mu';\pm1} \tag{A-30}$$

$$A_x^{\Lambda\Lambda'} = \frac{\left(A_-^{\Lambda\Lambda'} + A_+^{\Lambda\Lambda'} \right)}{\sqrt{2}} \tag{A-31}$$

$$A_y^{\Lambda\Lambda'} = i\frac{\left(A_+^{\Lambda\Lambda'} - A_-^{\Lambda\Lambda'}\right)}{\sqrt{2}} \tag{A-32}$$

$$A_\pm^{\Lambda\Lambda'} = \left[C\left(l\frac{1}{2}j;\ \mu-\frac{1}{2},+\frac{1}{2}\right)C\left(l'\frac{1}{2}j';\ \mu-\frac{1}{2},+\frac{1}{2}\right)\right.$$
$$\left. - C\left(l\frac{1}{2}j;\ \mu+\frac{1}{2},-\frac{1}{2}\right)C\left(l'\frac{1}{2}j';\ \mu+\frac{1}{2},-\frac{1}{2}\right)\right]\delta_{l-l';\pm 1}\delta_{\mu\mu'} \tag{A-33}$$

where $C_\Lambda^{m_s} = C\left(l\frac{1}{2}j;\ \mu-m_s,m_s\right)$ are the Clebsch-Gordon coefficients.

Taking into account the coupling between the large and small components in equation A-26, we arrive at the famous matrix element selection rules $M_\lambda^{\Lambda\Lambda'}$ of the electric dipole

$$l - l' = \pm 1 \tag{A-34}$$

$$j - j' = 0 \quad or \pm 1 \tag{A-35}$$

$$\mu - \mu' = \begin{cases} +1 & if \quad \lambda = + \\ -1 & if \quad \lambda = - \\ 0 & if \quad \lambda = z \\ \pm 1 & if \quad \lambda = x,y \end{cases} \tag{A-36}$$

These rules must be satisfied in any computations involving an electronic transition of type $\Lambda \to \Lambda'$ in the electric dipole approximation [9]

A.4 Non-Relativistic Muffin-Tin Orbital

Let's consider an atomic cell shaped into a sphere so that the potential inside it is spherically symmetrical and the electron's kinetic energy outside it is zero. Inside the sphere, the wave function of an electron is a solution for the Schrödinger's equation, which leads to the separation of variables (radial part) while in the exterior part, it satisfies Laplace's equation $\nabla^2\psi = 0$ in general, the radial part of the wave function has the form [10,11] The α_l and b_l coefficients are determined from the continuity conditions and the wave function differentiability on the sphere surface. Thus, the radial function is given by

$$\Phi_l(r, E)$$

$$= \begin{cases} u_l(r, E), & r \leq s \\ \left[\dfrac{D_l + l + 1}{2l + 1} \left(\dfrac{r}{s}\right)^l + \dfrac{l - D_l}{2l + 1} \left(\dfrac{r}{s}\right)^{-l-1} \right] u_l(r, E), & r > s \end{cases} \qquad \textbf{(A-37)}$$

Where $u_l(r, E)$ represents a solution to the radial Schrödinger equation for the atomic sphere with radius s, however, these functions are not used as basic functions because of the divergent part in the exterior part of the sphere $\frac{D_l + l + 1}{2l + 1} \left(\frac{r}{s}\right)^l$

To get rid of this part we do a subtraction of the divergent part from the two equations then we replace the $\left(\frac{r}{s}\right)^l$ with $\frac{\Phi_l(r,D)}{\Phi_l(s,l)}$. For the $r \leq s$ and the energy E with the logarithmic derivative D that corresponds to the energy $\left(D(E) = \left[\frac{\partial \ln(u(E,r))}{\partial \ln(r)} \right]_{r=s} \right)$ for both parts so the wave functions are written as [12]:

$$\overline{\Phi}_l(r, D)$$

$$= \begin{cases} \Phi_l(r, D) - \dfrac{D_l + l + 1}{2l + 1} \dfrac{\Phi_l(r, D)}{\Phi_l(s, l)} \Phi_l(r, l), & r \leq s \\ \dfrac{l - D_l}{2l + 1} \left(\dfrac{r}{s}\right)^{-l-1} \Phi_l(s, D), & r > s \end{cases} \qquad \textbf{(A-38)}$$

using the **A-38** equation the basic functions are written as:

$$\overline{\Phi}_L(r, D) = i^l Y_L(\hat{r}) \Phi_L(r, D) \qquad \textbf{(A-39)}$$

Creating a crystal using the ASA approximation mentioned above, and to simplify the problem we assumed that every cell contains one atom, to write the basic functions in this case we must take into consideration the effect of other atoms located at a distance R from the central atom. So, the crystal is described using the Bloch theorem written as follow [13]:

$$\chi_L^k(r, D) = \sum_{R \neq 0} e^{ik.R} \, \overline{\Phi}_L(r - R, D) \qquad \textbf{(A-40)}$$

the effect of other atoms sited on R is given by:

$$\overline{\Phi}_L(r - R, D) = i^l Y_L(\hat{r}, D) \left| \frac{r - R}{s} \right|^{-l-1} \frac{l - D_l}{2l + 1} \Phi_l(s, D) \tag{A-41}$$

using the additivity principle:

$$i^l Y_L(\hat{r}, D) \left| \frac{r - R}{s} \right|^{-l-1}$$

$$= 4\pi \sum_{L''L'}^{l''=l+l'} C_{LL''L'} \frac{(2l-1)!!}{(2l-1)(2l'+1)!!} \times (-i)^{l'} \left(\frac{R}{s} \right)^{-l'-1} Y_{L''}^*(\hat{R}) \tag{A-42}$$

$$\times i^{l'} \left(\frac{R}{s} \right)^{l'} Y_{L'}(\hat{r})$$

where $C_{LL''L'}$ are Gaunt coefficients defined by [14]:

$$C_{LL''L'} = \int Y_L(\hat{k}) Y_{L'}^*(\hat{k}) Y_{L''}(\hat{k}) d\hat{k} \tag{A-43}$$

For the function to be continuous and differentiable on the surface of the sphere, it is necessary to establish a change of the $\left(\frac{r}{s} \right)^l$ with $\frac{\Phi_{l'}(r,l')}{\Phi_{l'}(s,l')}$ in equation **A-42** so the basic functions that describe our system are written as:

$$\chi_L^k(r, D)$$

$$= \begin{cases} \Phi_L(r, D) - \Phi_l(s, D) \dfrac{l - D}{2l + 1} \displaystyle\sum_{L'} \left[S_{LL'}^k - \dfrac{l + 1 + D}{l - D} 2(2l + 1)\delta_{L'L} \right] \times \Phi_{L'}(r, l') \dfrac{1}{\Phi_{l'}(s, l')2(2l + 1)} & , r \leq s \\[2em] \Phi_l(s, D) \dfrac{l - D}{2l + 1} \left[i^l Y_L(r) \left(\dfrac{r}{s} \right)^{-l-1} + \displaystyle\sum_{L'} S_{LL'}^k \times i^{l'} Y(\hat{r}) \left(\dfrac{r}{s} \right)^{l'} \dfrac{1}{2(2l' + 1)} \right], & r > s \end{cases} \tag{A-44}$$

Where $S_{LL'}^k$ is the canonical structural constant defined as

$$S_{LL'}^k = \sum_{R \neq 0} e^{ik.R} S_{LL'}(R) \tag{A-45}$$

$$S_{LL'}^k(R) = -\frac{8\pi(2l + 2l' - 1)!!}{(2l - 1)!! (2l' - 1)!!} \times \sum_{L''}^{l''=l+l'} C_{LL''L'}(-i)^{l''} \left(\frac{R_s}{s} \right)^{-l''-1} Y_{L''}(\hat{R}) \tag{A-46}$$

147

The linear combination of the muffin-tin orbitals provides a solution to the Schrödinger equation for the whole crystal and it is written as follows:

$$\Psi_k(r) = \sum_L C_L(k) \sum_R e^{ik.R} \chi_L(k, r - R, D_l(E))$$

(A-47)

A.5   Relativistic Muffin Tin Orbitals

Unlike the non-relativistic approach that describes the crystal using a simplified approach that estimates the effect of other atoms to be constant, the relativistic approach uses a more realistic system taking into consideration the effect of spin and orbitals angular momentum and their interactions [1].

This approach implies the use of the Dirac equation that represents the relativistic version of the Schrödinger equation

$$\left[c\alpha.p + \frac{\beta c^2}{2} + V(r) \right] \Psi_k(r) = \left(\frac{c^2}{2} + E \right) \Psi_k(r)$$

(A-48)

Where c is light speed, the operator $p = -i\nabla$, α and β are the four-dimensional Dirac matrixes.

The solution to this equation with a spherically symmetrical potential is:

$$\Phi_K(r, E) = i^l Z_K(\hat{r}) \Phi_k(r, E)$$

(A-49)

with $K = (k, \mu)$, k is the quantum relativistic number and $\Phi_K(r, E)$ is the matrix radial solutions defined as

$$\Phi_K(r, E) = \begin{pmatrix} g_k(r, E) \\ if_k(r, E) \end{pmatrix}$$

(A-50)

while $Z_K(\hat{r})$ is the matrix angular spin functions and it is written as:

$$Z_K(\hat{r}) = \begin{pmatrix} \chi_k^\mu(\hat{r}) & 0 \\ 0 & \chi_{-k}^\mu(\hat{r}) \end{pmatrix}$$

(A-51)

with

$$\chi_k^\mu(\hat{r}) = \sum_{m=\pm\frac{1}{2}} C_{l,\mu-m,\frac{1}{2},m}^{j\mu} \, Y_{l,\mu-m}(\hat{r})\chi(m) \tag{A-52}$$

$C_{l,\mu-m,\frac{1}{2},m}^{j\mu}$ are the Klebsch-Gordan coefficients, $Y_{l,\mu-m}$ is the spherical harmonic and $j = l \pm \frac{1}{2}$

are the eigenvalue of the total angular momentum operator and can have two values:

$\chi\left(\frac{1}{2}\right) = \begin{pmatrix} 1 \\ 0 \end{pmatrix}$ or $\chi\left(-\frac{1}{2}\right) = \begin{pmatrix} 0 \\ 1 \end{pmatrix}$ which are Pauli spinors.

The radial function **A-47** is normalized within the muffin-tin sphere which means

$$\langle \Phi_K(r,E)|\Phi_K(r,E)\rangle = \int_0^s r^2 dr \, (g_k^2(r,E) + f_k^2(r,E) = 1 \tag{A-53}$$

The corresponding form of the logarithmic derivative of the radial part D is given by:

$$D_K(E) = s\frac{cf(s,E)}{g_k(s,E)} - k - 1 \tag{A-54}$$

Taking into consideration that $E = V_c = 0$ in the interstitial area, the radial part of the Dirac equation can be written as:

$$\left(\frac{d}{dr} + \frac{1-k}{r}\right)\tilde{f}_k(r) = 0 \tag{A-55}$$

their solutions are:

$$\left(\frac{d}{dr} + \frac{1+k}{r}\right)\tilde{g}_k(r) - c\tilde{f}_k(r) = 0 \tag{A-56}$$

$$\Phi_K(r,D) = \begin{pmatrix} g_k(r,D) \\ if_k(r,D) \end{pmatrix} = \begin{pmatrix} \left(\dfrac{r}{s}\right)^k \\ i\dfrac{(2k+1)}{cs}\left(\dfrac{r}{s}\right)^{k-1} \end{pmatrix}, \qquad D = k \tag{A-57}$$

$$\Phi_K(r,D) = \begin{pmatrix} g_k(r,D) \\ if_k(r,D) \end{pmatrix} = \begin{pmatrix} \left(\frac{r}{s}\right)^{-k-1} \\ 0 \end{pmatrix}, \qquad D = -k-1 \tag{A-58}$$

and

$$\widetilde{\Phi}_k(r,D) = i^l Z_K(\hat{r}) \widetilde{\Phi}_k(r,D) \tag{A-59}$$

The representation of solutions expressions **A-57, A-58** near the origin which mean $D = -l - 1$ is:

$$\Phi_K(r, -l-1) = i^l Z_K(\hat{r}) \begin{pmatrix} \left(\frac{r}{s}\right)^{-l-1} \\ i \dfrac{(-l-1+k+1)}{cs} \left(\frac{r}{s}\right)^{-l-2} \end{pmatrix} \tag{A-60}$$

while the regular solutions mean $D = l$ is:

$$\Phi_K(r, l) = i^l Z_K(\hat{r}) \begin{pmatrix} \left(\frac{r}{s}\right)^{l} \\ i \dfrac{(l+k+1)}{cs} \left(\frac{r}{s}\right)^{l-1} \end{pmatrix} \tag{A-61}$$

Hence, in the interstitial region, the solution of the Dirac equation that must be continued at the surface of the sphere is given by:

$$\Phi_K(r,D)$$
$$= i^l Z_K(\hat{r}) \times \begin{cases} \begin{pmatrix} g_k(r,D) \\ if_k(r,D) \end{pmatrix}, & r \le s \\ \left(\dfrac{l+1+D}{2l+1} \widetilde{\Phi}_k(r,l) + \dfrac{l-D}{2l+1} \widetilde{\Phi}_k(r,-l-1) g_k(s,D) \right), & r > s \end{cases} \tag{A-62}$$

Following the same procedures in equation **A-38**, we write new functions by eliminating the divergent parts. As a result, we obtain solutions of the Dirac equation:

$$\Phi_K(r, D)$$
$$= i^l Z_K(\hat{r})$$

$$\times \begin{cases} \Phi_k(r, D) - \dfrac{l + 1 + D}{2l + 1} \dfrac{g_k(s, D)}{g_k(s, l)} \widetilde{\Phi}_k(r, l), & r \leq s \\[4mm] \left(\dfrac{l - D}{2l + 1} \widetilde{\Phi}_k(r, -l - 1) g_k(s, D) \right), & r > s \end{cases} \tag{A-63}$$

To create all the crystals, we use the Bloch theorem as follows:

$$\chi_L^k(r, D) = \sum_{R \neq 0} e^{ik.R} \, \overline{\Phi}_L(r - R, D) \tag{A-64}$$

Then we develop the contribution of the function arriving from a point located at R. For this reason, we use the generalized form of the additivity principle[9]

$$i^l Z_K(\hat{r}) \widetilde{\Phi}_k(|r - R|, -l - 1) = \sum_{K'} i^{l'} Z_{K'}(\hat{r}) \widetilde{\Phi}_{k'}(r, l') \dfrac{S_{K'K}(R)}{-2(2l' + 1)} \tag{A-65}$$

$$S_{K'K}(R) = \sum_{LL'L''}^{l'' = l + l'} \left(-\dfrac{1}{2} \right) \dfrac{4\pi(2l'' - 1)!!}{(2l - 1)!! \, (2l' - 1)!!} C_{l', \mu' - m, 1/2, m}^{j' \mu'}$$
$$\times C_{L''L'L}(-i)^{l''} \left(\dfrac{R_s}{s} \right)^{-l'' - 1} Y_{L''}(\hat{R}) C_{l, \mu - m, 1/2, m}^{j \mu} \tag{A-66}$$

An expansion by analogy to the non-relativistic case is performed to finally obtain the exact expression of the relativistic MT orbitals inside the sphere [9]

$$\chi_L^k(r, D) = i^l Z_K(\hat{r}) \Phi_k(r, D) - \dfrac{D - l}{2l + 1} g_k(s, D)$$
$$\times \sum_{K'} i^{l'} Z_{K'}(\hat{r}) \Phi_{k'}(r, l') \dfrac{1}{g_k(s, l')} \left(-\dfrac{1}{2} \dfrac{1}{2l' + 1} \right) \tag{A-67}$$
$$\times \left(S_{KK'}^k - \delta_{KK'} \dfrac{D + l + 1}{D - l} 2(2l + 1) \right)$$

$S_{KK'}^k$ is the structural factor [1]

A.4 References

1   Boukelkoul, M. (2018). Propriétés magnéto-optiques des couches ultraminces et des slabs à base de métaux de transition (Doctoral dissertation).

2   Szotek, Z., Temmerman, W. M., & Winter, H. (1993). Application of the self-interaction correction to transition-metal oxides. Physical Review B, 47(7), 4029.

3   Wang, C. P. S., & Callaway, J. (1974). Band structure of nickel: Spin-orbit coupling, the Fermi surface, and the optical conductivity. Physical Review B, 9(11), 4897.

4   Singh, M., Wang, C. S., & Callaway, J. (1975). Spin-orbit coupling, Fermi surface, and optical conductivity of ferromagnetic iron. Physical Review B, 11(1), 287.

5   Ravindran, P., Delin, A., James, P., Johansson, B., Wills, J. M., Ahuja, R., & Eriksson, O. (1999). Magnetic, optical, and magneto-optical properties of MnX (X= As, Sb, or Bi) from full-potential calculations. Physical Review B, 59(24), 15680.

6   Antonov, V., Harmon, B., & Yaresko, A. (2004). Electronic structure and magneto-optical properties of solids. Springer Science & Business Media.

7   Horn, K., & Scheffler, M. (2000). Electronic structure. Elsevier.

8   Ebert, H. (1996). Magneto-optical effects in transition metal systems. Reports on Progress in Physics, 59(12), 1665.

9   Kharoubi, M. (2018). Effet Kerr magnéto-optique dans les multicouches de type métal magnétique/métal paramagnétique : FePt (Doctoral dissertation).

10   VARSHALOVICH, D., MOSKALEV, A., & KHERSONSKII, V. (1975). Quantum theory of angular momentum (Russian book). Leningrad, Izdatel'stvo Nauka, 1975. 440.

11   Turek, I., Drchal, V., Kudrnovský, J., Šob, M., Weinberger, P., Turek, I., ... & Weinberger, P. (1997). Linear Muffin-Tin Orbital (LMTO) Method. Electronic Structure of Disordered Alloys, Surfaces and Interfaces, 37-58.

12   Gunnarsson, O., Jepsen, O., & Andersen, O. K. (1983). Self-consistent impurity calculations in the atomic-spheres approximation. Physical Review B, 27(12), 7144.

13   Ouarda, B. (2017). Etude des propriétés magnétiques des multicouches métal/oxyde.

14   Xu, Y. L. (1996). Fast evaluation of the Gaunt coefficients. Mathematics of computation, 65(216), 1601-1612.

Appendix B

Scientific publications

Theoretical Investigation of Structural, Spectroscopic (IR, ^{1}H and ^{13}C NMR), Static, and Frequency-Dependent Nonlinear Optical Properties of 4-[(1E)-3-(4-Methoxyphenyl)-3-Oxoprop-1-en-1-yl]Phenyl 4-Methylbenzene-1-Sulfonate

Mohamed Bensebaa, Mebarek Boukelkoul, Ömer Tamer, Yusuf Atalay & Davut Avcı

Published online: 12 Sep 2023.

Submit your article to this journal ↗

View related articles ↗

View Crossmark data ↗

Taylor & Francis
Taylor & Francis Group

Check for updates

Theoretical Investigation of Structural, Spectroscopic (IR, ^{1}H and ^{13}C NMR), Static, and Frequency-Dependent Nonlinear Optical Properties of 4-[(1E)-3-(4-Methoxyphenyl)-3-Oxoprop-1-en-1-yl]Phenyl 4-Methylbenzene-1-Sulfonate

Mohamed Bensebaa[a], Mebarek Boukelkoul[a], Ömer Tamer[b], Yusuf Atalay[b], and Davut Avcı[b]

[a]Laboratoire de Physique Quantique et Systèmes Dynamiques, Department of Physics, Faculty of Sciences, Ferhat ABBAS Sétif1 University, Sétif, Algeria; [b]Faculty of Science, Department of Physics, Sakarya University, Sakarya, Turkey

ABSTRACT

The present study reports the theoretical investigations of nonlinear optical properties of chalcone derivative namely 4-[(1E)-3-(4-methoxyphenyl)-3-oxoprop-1-en-1-yl]phenyl 4-methylbenzene-1-sulfonate (4MPMS). Density functional theory calculations on the geometry optimization, vibrational spectrum, ^{1}H and ^{13}C NMR chemical shifts, frontier molecular orbitals energies, and nonlinear optical properties are carried out by using B3LYP level in conjunction with 6–311++G(d,p) basis set. The static and frequency-dependent nonlinear optical properties (polarizability (α), anisotropy of polarizability ($\Delta\alpha$), first and second-order hyperpolarizabilities (β and γ)) are investigated by using B3LYP level. The static NLO parameters (β(0;0,0) and γ(0;0.0.0)) were calculated as 16.240×10^{-30} and $213.77 \times 10^{-36\,esu}$. The second harmonic generation (SHG) β(-2w,w,w) and γ(-2w,w,w,0) parameters for the title molecule are found to be 213.97×10^{-30} esu and 485.90×10^{-36} esu, respectively. So, the frequency-dependence of β and γ parameters is clear. The obtained results demonstrated that there is a frequency dependence on the nonlinear optical properties of 4MPMS, and the title molecule is a possible candidate for first and second-order nonlinear optical materials.

Introduction

Nonlinear optical (NLO) properties, discovered in 1961 a short time after discovering the laser, describe the reaction of a material being exposed to an intense optical field.[1] The search for novel nonlinear optical materials is one of the newest and most attractive studies in materials regarding their vast field of application, especially in advanced technology devices such as spectroscopy, sensors, information processing,[2] communication, signal treatment, and data storage.[3] Since the beginning of NLO studies, a lot of materials have been examined from organic, and organometallic to inorganic materials, and it has been reported that each type of these materials has its advantages and disadvantages. However organic materials are the most commonly used recently due to their low cost of production and their potential possibility to make changes on the atomic level, the functional groups that work as electron donors and acceptors through the π-conjugator

bridge, and their flexibility.[4] All those advantages in the organic materials give them the ability to have better NLO properties compared to other types of materials which was the purpose and the excitement for us to choose the chalcone as an organic material for our study.

In chalcones, two fragrant rings are connected by an aliphatic three-carbon series with π conjugation bound, which gives high electron mobility, two functional groups that work as donors and acceptors which give the material a good polarizability, and a high damage threshold.[5,6] Studies have also proved that chalcone derivatives are a good organic complement that can bond with metals to form an organometallic material.[7] Chalcone has a large domain of application in the environment and healthcare field as an antioxidant[8] and in pharmaceutical and medicine as an antibacterial, antifungal, anti-inflammatory, and anticancer therapy.[9,10] And in the optical field where chalcones have been experienced as a solar shield from UV irradiation,[11] and in nonlinear optics especially optical telecommunication with the optical switching and optical limiting due to ultrafast sign change for absorption and refraction,[12] also in frequency mixing and conversion.[13]

Many NLO studies have been carried out on chalcone derivatives. For example, the effect of 2-chloro-4-fluorochalcone molecular structure on the NLO response was investigated. The findings indicated that the NLO properties of chalcone can be optimized by substituting donor and acceptor groups with enhanced ones, such as hydroxyl and methoxy groups.[14]

Additionally, researchers aimed to synthesize chalcone with thiophene heterocyclic. This was done because of its ability to form crystals with a desirable, well-defined shape. These crystals exhibited a high non-linear refractive index susceptibility and absorption coefficient, estimated to be in the order of 10–9cm2/W. Also, the asymmetric electron distribution increases with the substitution of the acceptor and donor groups to the opposite edges of the investigated system. It is in good agreement with the results found for fluorinated chalcone.[15]

Density functional theory (DFT) is a quantum mechanical method used in a wide range of fields such as physics, chemistry, and material science. The DFT method is used to calculate the electronic structure of atoms, molecules, and solids. The DFT approximation is a popular method in solid-state physics since the 1970s, Until the 1990s, improvements in the method made it acceptably accurate for quantum-chemical applications, resulting in increased applications. Improvements to the method until the 1990s made the DFT method acceptably accurate for quantum chemical applications, resulting in increased applications. Thus, large molecular systems can be investigated with high accuracy, thereby expanding the predictive power inherent in electronic structure theory. As a result, DFT is now by far the most widely used electronic structure method. The DFT method also allows to control of various parameters that can't be achieved experimentally such as very high or low temperature and pressure or unusual chemical environments can be simulated to understand how molecules behave in such scenarios.[16] The use of the DFT method for the key fields of technology such as nonlinear optics and photonics is expected to supply guidance and accelerate improvements in these fields.

In this study, it is intended to calculate the ground-state geometric structure, vibrational spectrum, electronic and nonlinear optical properties of the 4MPMS molecule synthesized by Vinaya and his coworkers,[17] which has electron donor and acceptor groups, and which contains long π-bridges between these groups, and which has a relatively high electrical charge asymmetry, by using DFT/B3LYP/6-311++G(d,p) level. In this way, the relationship between molecular structure and NLO activity for 4MPMS will be explained and the validity of the DFT method on chalcone derivatives will be tested.

Computational details

The geometric structure of the title molecule is calculated using the GAUSSIAN 16[18] program using the B3LYP (Becke's three-parameter hybrid functional using the LYP correlation functional) method[19,20] and 6-311++G(d,p) basis set. The results are displayed and analyzed using

GAUSSVIEW 6 software.[21] Structural optimization is performed at the ground state energy level. IR vibrational spectrum is supported by the potential energy distribution (PED) analysis, the obtained results are multiplied by 0.9614 to lower the difference between the experimental and the theoretical results.[22,23] The highest occupied and lowest unoccupied molecular orbitals (HOMO, LUMO) are obtained and supported *via* the SWIZARD program.[24] The NMR spectra are evaluated by GIAO (Gauge Including Atomic Orbital) approximation method.[25–27] The solvent effect is considered with the CPCM (Conductor like Polarizable Continuum Model). The NLO properties and the molecular potential surface of the title molecule are investigated on the basis of the optimized structure. The NLO parameters such as polarizability, first-and second-order hyperpolarizability (α, β, and γ) are obtained in a static and dynamic method.

Results and discussion

Optimized geometry

The molecular geometry of the studied material is optimized in the ground state energy level without any imposed condition *via* the B3LYP level and 6-311++G(d,p) basis set. The experimental structure and the optimized theoretical structure are presented in Figure 1. Both theoretical and experimental results are in good agreement. However, the small difference between them is due to the fact that during the theoretical calculation, the molecule is taken in the gas phase but in the experimental one, it is considered in the solid crystal phase. The theoretical and experimental[17] bond length results are presented in Table 1. In our molecule, the carbonyl group (C=O) represents an important functional group, especially in our study, and it was reported that this functional group has an important effect on the NLO properties. In recent studies this bond length was obtained in the range of 1.23 Å- 1.22 Å which is similar to our theoretical and experimental results which are localized in the range of 1.22 Å-1.23 Å,[28,29] for the benzene rings the average bond length is 1.396 Å which also agrees with the experimental and theoretical results
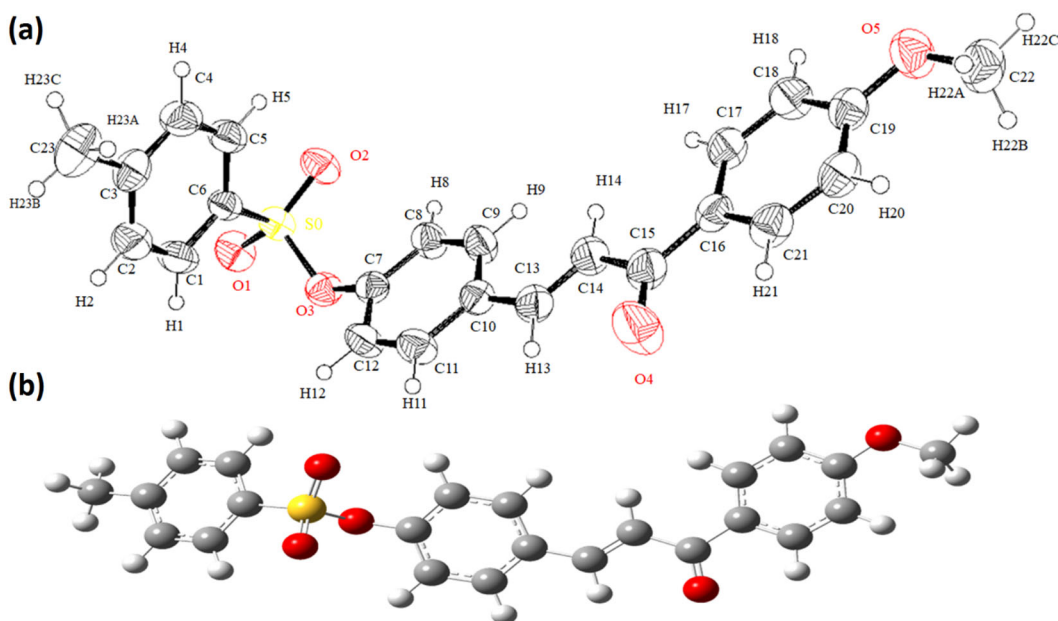
Figure 1. a) Crystal structure,[17] b) optimized geometry for 4MPMS with the atomic numbering.

Table 1. The experimental and calculated bond length (Å) for 4MPMS.

Bonds	Exp.[17]	B3LYP/6-311++G(d,p)
S-O1	1.4208	1.4545
S-O2	1.4286	1.4554
S-O3	1.5974	1.6837
S-C6	1.746	1.7808
O3-C7	1.41	1.3983
O4-C15	1.218	1.2261
O5-C19	1.364	1.3583
O5-C22	1.422	1.4241
C1-C2	1.371	1.3905
C1-C6	1.377	1.3924
C2-C3	1.375	1.4004
C3-C4	1.377	1.4005
C3-C23	1.508	1.5077
C4-C5	1.373	1.3904
C5-C6	1.377	1.3924
C7-C8	1.375	1.3946
C7-C12	1.369	1.3893
C8-C9	1.38	1.3866
C9-C10	1.386	1.4071
C10-C11	1.39	1.4053
C10-C13	1.464	1.4614
C11-C12	1.374	1.39
C13-C14	1.306	1.3448
C14-C15	1.479	1.4862
C15-C16	1.476	1.4954
C16-C17	1.392	1.406
C16-C21	1.391	1.4004
C17-C18	1.366	1.3848
C18-C19	1.393	1.4009
C19-C20	1.371	1.401
C20-C21	1.37	1.389
C3-C23	1.508	1.5077
C4-C5	1.373	1.3904
C5-C6	1.377	1.3924
C7-C8	1.375	1.3946
C7-C12	1.369	1.3893
C8-C9	1.38	1.3866
C9-C10	1.386	1.4071
C10-C11	1.39	1.4053
C10-C13	1.464	1.4614
C11-C12	1.374	1.39
C13-C14	1.306	1.3448
C14-C15	1.479	1.4862
C15-C16	1.476	1.4954
C16-C17	1.392	1.406
C16-C21	1.391	1.4004
C17-C18	1.366	1.3848
C18-C19	1.393	1.4009
C19-C20	1.371	1.401
C20-C21	1.37	1.389

1.397 Å and 1.38 Å respectively.[29,30] Sulfonate bond length varies between 1.42 Å for S=O and 1.59 Å for S-O compared to 1.455 and 1.425 Å for the theoretical and experimental results respectively.[29,31] In the literature, it is known that The C-O-C bond angle is given to be 118.7° which strongly agrees with our theoretical and experimental results. For the C-C-C bond angles in the aromatic rings, the average calculated result is 120°. It is similar to the experimental results and also agrees well with the literature. For the O=C-C, the literature indicates that the average angle is 120° which is similar to the results we obtained and the experimental results.[29,32,33] For the sulfur, the O-S-O and C-S-O bond angles are in the range of 103°–120° for both experimental and calculated results. It is clear that it is in good agreement with the literature. The bond angle details are presented in Table 2.

Table 2. The experimental and calculated bond angles (°) for 4MPMS.

Bond angles	Exp.[17]	B3LYP/6-311++G(d,p)
O1-S-O3	109.71(10)	107.97
O1-S-C6	109.35(11)	110.09
O2-S-O1	119.52(11)	120.66
O2-S-O3	102.64(10)	108.07
O2-S-C6	110.51(11)	110.17
O3-S-C6	103.82(9)	97.24
C7-O3-S	121.86(14)	117.84
C19-O5-C22	117.7(2)	118.9
C2-C1-C6	119.0(2)	118.74
C1-C2-C3	121.8(3)	121.19
C2-C3-C4	118.0(2)	118.55
C2-C3-C23	121.3(3)	120.72
C4-C3-C23	120.7(3)	120.7
C5-C4-C3	121.6(2)	121.18
C4-C5-C6	119.0(2)	118.75
C1-C6-S	119.96(18)	119.16
C5-C6-S	119.39(19)	119.26
C5-C6-C1	120.6(2)	121.56
C8-C7-O3	121.9(2)	119.9
C12-C7-O3	116.5(2)	118.79
C12-C7-C8	121.4(2)	121.22
C7-C8-C9	118.5(2)	119.19
C8-C9-C10	122.0(2)	121.18
C9-C10-C11	117.2(2)	118
C9-C10-C13	123.3(2)	123.43
C11-C10-C13	119.5(2)	118.55
C12-C11-C10	121.8(2)	121.41
C7-C12-C11	119.1(2)	118.97
C14-C13-C10	129.1(2)	127.91
C13-C14-C15	122.2(2)	120.34
O4-C15-C14	119.4(3)	120.86
O4-C15-C16	120.3(2)	120.14
C16-C15-C14	120.3(2)	118.98
C17-C16-C15	123.8(2)	124.27
C21-C16-C15	119.2(2)	117.86
C21-C16-C17	117.0(2)	117.85
C18-C17-C16	121.2(2)	121.16
C17-C18-C19	120.2(2)	120.13
O5-C19-C18	115.3(2)	115.85
O5-C19-C20	125.0(2)	124.54
C20-C19-C18	119.7(2)	119.6
C21-C20-C19	119.4(2)	119.52
C20-C21-C16	122.4(2)	121.71

Vibrations analysis

The vibration analysis is a commonly used method to identify the functional groups and intermolecular interaction for organic and organometallic structures, which represents a useful tool to study the physical and chemical properties of molecular systems.[34] The IR vibration frequencies of 4-[(1E)-3-(4-methoxyphenyl)-3-oxoprop-1-en-1-yl]phenyl 4-methylbenzene-1-sulfonate (4MPMS) are reported experimentally in the range 400–4000 cm^{-1}.[17] In our study, the corresponding vibration spectrum is calculated by the B3LYP method and 6-311 G++(d,p) basis set and presented in Figure 2 and Table 3. VEDA 4[35] software and the potential energy distribution (PED) are also executed to provide detailed information about the contribution of vibrational modes to a specific wavenumber. The obtained theoretical wavenumbers are multiplied by the scale factor 0.96 to make theoretical results more comparable to experimental data. The studied molecule is formed by different elements and functional groups related to each other by bonds which lead to different types of vibrations at different wavelengths.
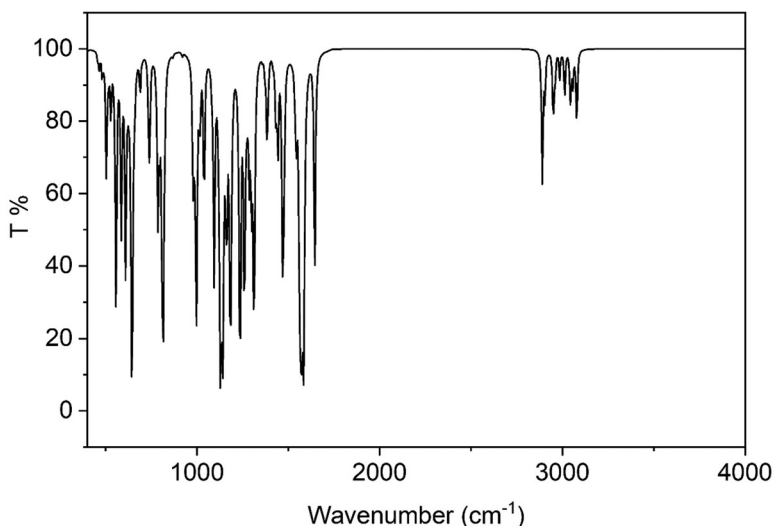
Figure 2. Theoretical IR spectrum for 4MPSM calculated by B3LYP/6-311++G(d,p) level.

C-C And C = C vibration

This type of vibration is caused by the movement of electrons through the bonds between carbon atoms, it can be used to study the molecule structure and many other properties such as the identification of specific chemical compounds. These types of stretching vibration have been reported in the range 1000–1650 cm^{-1} in the literature,[29,34] which agrees well with the calculated results that we have obtained. The C-C stretching is calculated with different PED contributions, and two of the highest PED contributions are 58% at 1284 cm^{-1} and 51% at 1550 cm^{-1}. The double bond stretching of carbon is expected in the range of $1593 - 1629$ cm^{-1}.[36-39] The experimental results indicated that this bond vibration is located at 1605 cm^{-1} which is in the range of the calculated wavelength in the range of $1583 - 1645$ cm^{-1} that matches the results obtained by R.S Saji et al.,[40] and agrees with literature results in both cases. The carbon bending vibration occurs in the range 400–1200 cm^{-1} which contains the in-plane and out-of-plane deformation with different PED contributions between (10% −90%), as would be expected.[41,42]

C-H vibration

The C-H stretching appears at around 3000 cm^{-1}.[36] The obtained theoretical results indicate that the C-H stretching in the range 2891− 2986 cm^{-1} originates from the vibration of the methyl group. The vibration bands at the $3043 - 3082$ cm^{-1} range are related to the vibration of the stretching of the aromatic rings confirming the experimental results that are identified between $2932.1 - 3062.3$ cm^{-1} as a C-H stretching. These vibrations at this region are pure C-H stretching with a high PED contribuof tion around 90%-100% which agrees with the results obtained by R.S Saji et al.[40] The in-plane bending C-H vibrations are calculated at the range of 1100–1478 cm^{-1} but the out-of-plane bending is in the range of 789–1019 cm^{-1}. They agree with the previous studies where the reported in-plane bending of C-H is at the range of $970 - 1230$ cm^{-1} while the out-plan bending is at the range of 660 cm^{-1} – 910 cm^{-1}.[36,39,41,43,44]

C-O And C = O vibration

The carbonyl group is an important structural unit in organic chemistry, it plays a key role in plenty of chemical reactions and compounds properties such as NLO properties, because of its electronegativity which makes it a polar group and this compound has also an intense stretching

Table 3. Experimental[17] and theoretical vibrational wavenumbers (cm^{-1}) for 4MPMS.

FT-IR[17]	B3LYP/6-311++G(d,p)	IR intensity	Raman intensity	Assignment with PED analysis
	3081	6.35	233.0524	ν CH 93(%)
	3080	5.59	103.6861	ν CH 87(%)
	3079	17.76	23.0781	ν CH 86(%)
	3077	4.51	146.3084	ν CH 93(%)
	3077	3.11	10.9302	ν CH 91(%)
	3076	0.1734	9.9469	ν CH 96(%)
	3067	0.4644	48.5039	ν CH 85(%)
3062.3	3065	0.4431	39.7788	ν CH 96(%)
	3058	14.41	62.996	ν CH 93(%)
	3054	0.1547	14.449	ν CH 96(%)
	3047	5.95	71.6029	ν CH 93(%)
	3044	9.2	128.2137	ν CH 95(%)
	3043	10.41	109.7333	ν CH 96(%)
	3022	0.4711	28.3521	ν CH 98(%)
	3012	22.32	175.0867	ν CH 91(%)
	2986	11.93	69.5059	ν CH 99(%)
	2959	14.57	105.0435	ν CH 100(%)
2932.1	2950	32.43	74.9363	ν CH 100(%)
	2905	20.19	420.3453	ν CH 99(%)
	2891	70.5	205.0948	ν CH 91(%)
1661.1	1645	144.79	284.4238	ν CC 22(%) + OC 52(%)
1605	1583	360.08	468.0102	ν CC 21(%) + OC 10(%)
	1572	314.58	645.7628	ν CC 28(%)
	1571	35.95	125.7038	ν CC 31(%)
	1563	177.27	9488.5248	ν CC 13(%) + OC 17(%)
	1550	0.6608	7.5554	ν CC 51(%) + β CCC 10(%)
	1544	35.76	374.3198	ν CC 41(%)
	1538	10.19	578.4512	β CCC 10(%) + ν CC 43(%)
1501.1	1478	35.06	140.5226	β HCC 56(%)
	1471	162.15	6.7775	β HCC 66(%)
	1463	9.45	1.4537	β HCC 64(%)
	1444	50.03	16.688	β HCH 79(%) + γ HCOC 20(%)
	1434	9.74	18.2358	β HCH 76(%) + γ HCOC 16(%)
	1431	16.52	9.1611	β HCH 79(%) + γ HCCC 14(%)
	1430	7.91	18.7237	β HCH 65(%) + γ HCCC 11(%)
1417.4	1417	3.7	10.4502	β HCH 80(%)
	1389	13.33	11.6377	ν CC 40(%) + β HCC 14(%)
	1384	40.92	166.8891	ν CC 32(%) + β HCC 20(%)
	1373	7.53	0.2261	ν CC 37(%)
1360.3	1359	1.778	34.5661	β HCH 94(%)
	1312	225.83	332.6805	β HCC 33(%)
	1299	82.94	139.3251	ν CC 10(%) + β 38(%)
	1287	55.09	21.7054	ν CC 46(%)
	1284	11.13	1.0753	ν CC 58(%)
	1279	0.0895	0.1462	ν CC 21(%) + β HCC 70(%)
	1275	15.86	14.8021	ν CC 13(%) + β HCC 39(%)
	1267	11.73	18.5319	β HCC 35(%)
	1260	91.22	232.5773	ν CC 21(%)
	1259	97.03	43.1323	ν SO 68(%)
	1236	300.69	60.8537	ν OC 44(%)
	1187	136.81	69.3788	ν CC 33(%) + β HCC 17(%)
	1182	134.01	539.8846	ν CC 32(%)
	1180	9.33	105.3319	ν CC 37(%)
	1164	100.49	23.7679	β HCC 19(%) + ν 18(%)
	1159	24.31	4.3092	β HCC 69(%)
1148.8	1154	6.01	2.6704	γ HCOC 56(%) + β HCH 16(%)
	1141	331.49	125.322	β HCC 44(%)
	1129	393.81	900.1926	ν OC 17(%) + β HCC 34(%)
	1120	0.6438	2.7284	β HCH 30(%) + γ HCOC 69(%)
	1094	130.31	20.0276	ν SO 51(%) + SC 11(%)
	1093	8.96	0.237	ν CC 15(%) + β HCC 61(%)
1091.7	1093	8.96	2.0868	ν CC 26(%) + β HCC 46(%)
	1081	5.77	4.7529	ν CC 29(%) + β HCC 34(%)

(continued)

Table 3. Continued.

FT-IR[17]	B3LYP/6-311++G(d,p)	IR intensity	Raman intensity	Assignment with PED analysis
	1040	80.55	50.1741	ν CC 34(%) + SO 35(%)
	1019	18.02	0.6228	γ HCCC 55(%) + β HCH 16(%)
	1014	18.72	29.1029	ν OC 68(%)
	997	209.73	323.7467	ν CC 45(%)
	991	6.55	0.8432	β CCC 66(%)
	990	14.27	15.9515	β CCC 53(%)
	982	27.55	3.6392	γ HCCC 90(%)
	978	53.25	123.7915	β CCC 55(%) + ν CC 10(%)
	970	0.1154	0.2901	γ HCCC 48(%) + β HCH 20(%)
	953	0.0275	0.0136	γ HCCC 65(%) + HCCS 22(%)
	950	0.6852	1.6616	γ HCCC 81(%)
	937	0.2421	0.3368	γ HCCC 87(%)
	937	0.2566	0.2072	γ HCCC 74(%)
	924	0.285	0.9085	γ HCCC 64(%)
	921	1.62	0.8381	γ HCCC 35(%) + CCCC 34(%)
874.3	869	1.51	22.8755	β CCC 22(%)
	857	0.2334	12.9115	γ HCCC 56(%) + τ OCCC 12(%)
823	826	10.15	1.8003	γ HCCC 14(%) + τ CCOC 12(%)
	817	3.74	0.6297	γ HCCC 76(%) + HCCS 22(%)
	816	200.26	40.3148	ν CC 27(%) + OC 17(%)
	810	113.17	5.6181	γ HCCC 10(%) + τ OCCC 12(%)
	797	34.02	2.8482	γ HCCC 63(%)
	796	0.1196	0.2242	γ HCCC 95(%)
	789	0.1223	0.8918	γ HCCC 99(%)
	786	92.42	23.1769	ν CC 11(%)
	781	1.93	8.2347	ν CC 14(%) + β 27(%)
	735	18.79	87.3344	γ CCCC 12(%) + τ OCCC 14(%)
708.2	703	0.845	2.4548	γ CCCC 45(%)
	689	16.84	8.8188	γ CCCC 60(%) + τ CCCC 10(%)
659.5	660	10.39	1.0228	γ CCCC 24(%) + τ OCCC 28(%)
	644	376.13	150.5793	ν CC 12(%) + SC 17(%)
	628	8.33	69.131	β CCC 56(%)
	621	10.14	7.7397	β CCC 36(%)
	621	0.1855	6.0046	β CCC 71(%)
	610	137.7	379.3931	ν SO 35(%)
	587	103.66	29.9998	β OCC 10(%) + CCC 22(%)
	529	29.6	19.116	τ OCOS 23(%)
	516	8.68	6.2129	β CCC 19(%)
	504	61.18	0.7382	β OSO 20(%) + τ CCOC 16(%)
	491	2.66	0.5164	γ CCCC 11(%) + τ OCCC 29(%)
	482	10.98	13.8435	β COC 15(%) + OCC 10(%)
	466	6.61	2.5875	β OSO 20(%) τ OCOS 30(%)
	458	3.89	44.5582	τ CCCC 21(%)
	451	0.2055	24.2259	β OSO 33(%)
	406	0.2396	0.2925	γ HCCC 14(%) + γ CCCC 63(%)
	404	0.1753	1.611	γ CCCC 32(%) + γ CCCO 24(%)
	400	0.2715	7.5394	γ CCCC 30(%)

ν: stretching, β: in-plane binding, γ: out-of-plane bending

in the interval $1600 - 1800\,\mathrm{cm}^{-1}$.[36] The C=O bond occurred in the range $1563 - 1645\,\mathrm{cm}^{-1}$ (52% PED contribution), on the other hand, the experimental results reported the wavenumber at $1661.1\,\mathrm{cm}^{-1}$ which is close to the calculated results and both results agree with the literature.[29]

C-O stretching vibration has been identified at $1014\,\mathrm{cm}^{-1}$ with 68% PED contribution and at $1236\,\mathrm{cm}^{-1}$ with 44% PED contribution and that approves the experimental results that referred to the C-O in the wavenumber $1091.7\,\mathrm{cm}^{-1}$. For the out-of-plane, bending occurs with a high PED contribution in the $1154\,\mathrm{cm}^{-1}$ and the $1120\,\mathrm{cm}^{-1}$ beside other wavenumbers but with a low PED contribution which agrees well with F. Rizwana et al. where they found the C-O seretching at 1021, 1036 and $1092\,\mathrm{cm}^{-1}$.[36,45,46] The other types of vibration are obtained in the range of 466 - $1120\,\mathrm{cm}^{-1}$ which contains torsion and bending vibrations.[47,48]

S = O, S-O, and S-C vibration

The S-C stretching vibration changes by the variety of compounds where the literature pointed that it is in the range, of 590-700 cm^{-1} while our results indicate it at 644 cm^{-1} with 17% PED contribution, and 1094 cm^{-1} with 11% PED contribution.[33,49] The S = O bond stretching vibration is determined between 1259 and 1040 cm^{-1} which agrees well with P. Manjusha et al. and other previous studies.[49–52] The experimental stretching results are found in the range 1148.8 − 1360.3 cm^{-1}, and this interval encompasses our results. Another vibration band is noted at 610 cm^{-1} with a 35% PED contribution which is likely to be the S-O stretching. All the obtained results are generally in agreement with the literature despite the slight difference due to the fact that our calculation is made on an isolated molecule in the gas phase, while the experimental molecule is in the solid phase with interactions with other molecules.

^{1}H and ^{13}C NMR analysis

The NMR analysis is a technique used to study the physical and chemical properties of materials by measuring the resonance frequency of nuclear magnetic moments in a sample under the effect of an electromagnetic field. The NMR method represents a useful tool to anticipate how the structure is formed for the organic and organometallic compounds.[52] Concerning the theoretical study, ^{1}H and ^{13}C NMR calculation of 4MPMS is performed with the B3LYP method and 6-311++G(d,p) basis sets using the GIAO (gauge independent atomic orbital) approach.[53] The obtained results are shown in Table 4 and compared with the experimental results.

In a previous study, the methoxy group (OCH$_3$) protons give a resonance signal at 3.88 ppm.[54] The ^{1}H NMR chemical shifts for the OCH$_3$ group are calculated at 4.1983, 3.8948, and 3.8813 ppm which includes the experimentally reported result of 3.89 ppm.[17] In another study, a methyl group (CH$_3$) bounding to a benzene ring give signals in the range of 2.85–4.46 ppm.[55] In the current study, the same ^{1}H NMR signals previously reported at 3.896 and 2.460 ppm[17] have been calculated at the range of 4.1983–2.4736 ppm. When it comes to benzene ring protons, these protons give ^{1}H NMR signals in the range of 8.2791–6.7086 ppm.[52] In the experimental study,[17] the same protons give signals in the range of 8.034–6.995 ppm. In the present study, benzene ring proton NMR signals are calculated at the range of 8.7363–7.1778 ppm. The ^{1}H NMR signals for H-C-C-H (H13 and H14) experimentally observed at 7.735 and 7.50 ppm are calculated at 8.3468 and 8.1631 ppm. The higher chemical shifts for the H5 (8.24 ppm), H1 (8.17 ppm), and H9 (8.49 ppm) are related to the near atoms that have high electronegativity. The obtained ^{1}H NMR results for the C$_6$H$_4$SO$_3$ group agree with the previously reported results for a similar structure reported in the range of 10.74-7.369 ppm.[52]

The ^{13}C NMR shifts for the title molecule are calculated by using B3LYP/6-311++G(d,p) level, and the obtained results are presented in Table 4. It is known that aromatic carbon has ^{13}C NMR signals in the interval of 120–160 ppm.[56] In this study, ^{13}C NMR signals for all aromatic C atoms are calculated at the range of 115.44 − 172.99 ppm. It should be noted that the electronegative O and S atoms are responsible for the shifts of some ^{13}C NMR signals (C19 and C7) to up-field regions. Atoms with high electronegativities, such as O, S, or N, polarize the electron densities of the surrounding (especially bonding) atoms around themselves and stimulate the C atoms to resonate in the lower region. Accordingly, the chemical shifts for C15, C19, and C7 are calculated higher than other carbon signals. The highest chemical shift is calculated for C15 with 191.95 ppm as consistent with the literature.[36] It was reported that the methyl C atom gives NMR signal at 24.6 ppm.[55] The NMR Signal for the methyl group C atom (C23) is calculated at 24.16 ppm. The other methyl group C atom (C22) gives NMR band at 57.4671 ppm due to the electronegativity of the O atom.[35]

Table 4. ^{1}H and ^{13}C NMR Isotropic shifts (ppm) for 4MPMS.

H/C	B3LYP/6-311++G(d,p)	Exp.[17]
H21	8.7363	8.034
H9	8.4924	8.012
H13	8.3468	7.735
H17	83,197	7.714
H5	8.2451	7.701
H1	8.1712	7.57
H14	8.1631	7.5
H11	7.8574	7.549
H5	7.8434	7.461
H8	7.8434	7.339
H2	7.7722	7.319
H4	7.7418	7.264
H12	7.5977	7.047
H18	7.2773	7.026
H20	7.1778	6.995
H22C	4.1983	3.896
H22A	3.8948	3.896
H22B	3.8813	3.896
H23B	2.7944	2.46
H23C	2.4805	2.46
H23A	2.4736	2.46
C15	191.958	–
C19	172.998	–
C7	159.73	–
C3	156.582	–
C13	153.175	–
C6	145.083	–
C11	142.541	–
C10	141.802	–
C21	139.652	–
C16	137.86	–
C17	137.025	–
C2	136.772	–
C4	136.772	–
C5	134.831	–
C1	134.647	–
C9	132.82	–
C12	132.714	–
C8	132.45	–
C14	124.57	–
C18	123.108	–
C20	115.44	–
C22	57.4671	–
C23	24.1602	–

Frontier molecular orbital analysis

The frontier molecular orbitals, the highest occupied molecular orbital (HOMO), and the lowest unoccupied molecular orbital (LUMO) are commonly used in quantum chemistry since they play a crucial role in predicting the electric and optical properties of a molecular system.[57] The energy gap between the HOMO and LUMO energies also reflects the chemical stability of a molecular system.[58,59] HOMO-LUMO energy gap in organic molecules plays a significant role in the movement of electrons. This energy gap can have significant implications for the stability and reactivity of the molecule. Molecules with large HOMO-LUMO gaps are typically more stable and unreactive, while those with small gaps tend to be more reactive. It is also used to assess molecular hardness and softness, where hard molecules, which have a high HOMO-LUMO energy gap, are less polarizable and have lower chemical and biological activity, but are more kinetically susceptible. On the other hand, soft molecules, which have a low HOMO-LUMO gap, are more polarizable and have higher chemical and biological activity, and this leads to better NLO properties.[52,60,61]
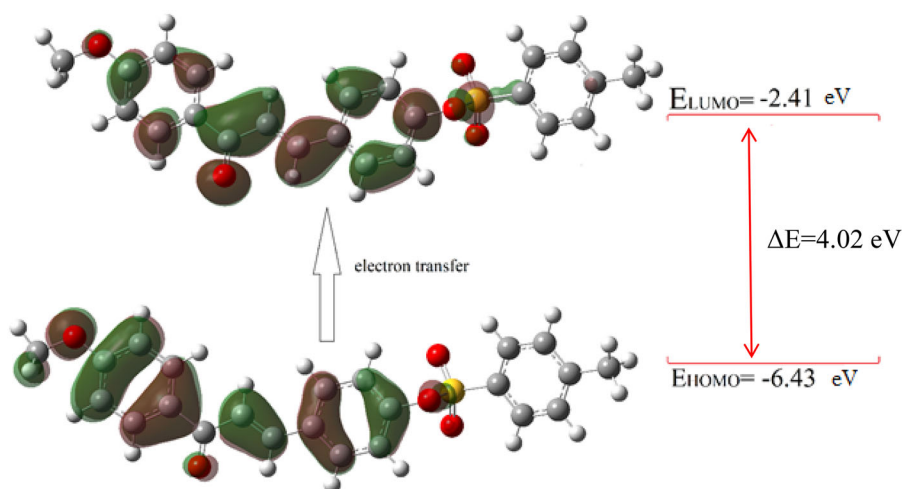
$E_{LUMO}= -2.41$ eV

$\Delta E = 4.02$ eV

$E_{HOMO}= -6.43$ eV

electron transfer

Figure 3. The frontier molecular orbitals and their energies calculated for 4MPMS by B3LYP/6-311++G(d,p).

Table 5. Frontier molecular orbital energies, electronegativity (χ), hardness (η), and softness (S) for 4MPMS obtained by B3LYP/6−311++G(d,p) level.

Parameters	4MPMS
E_{HOMO}(eV)	−6.43
E_{LUMO}(eV)	−2.41
ΔE(eV)	4.02
χ(eV)	4.42
η(eV)	1.9
S(eV^{-1})	0.25

HUMO and LUMO energies of the 4MPMS molecule are calculated using the B3LYP/6-311++G(d,p) level and the obtained results are shown in Figure 3. As presented in Figure 2, the charges are localized around the aromatic rings and the oxygen atoms for both HOMO and LUMO. The HOMO and LUMO energies are calculated for the 4MPMS as −6.4382 and −2.4139 eV respectively. The gap energy is found to be 4.0241 eV.

To understand the chemical reactivity of the 4MPMS, it is helpful to consider the quantum chemical parameters, such as the ionization potential (IP), electron affinity (EA), electronegativity (χ), hardness (η), chemical potential (P), and softness (S) calculated by frontier molecular orbital energies.[59] The obtained χ, η, and S are represented in Table 5. According to these results, 4MPMS is a more polarizable, chemically soft, and reactive molecule.

MEP analysis

Molecular electrostatic potential (MEP) is a way of visualizing the distribution of electrical charge within the studied molecule. The MEP is often represented as a surface map that displays molecular size, and shape as well as positive, negative, and neutral electrostatic potential regions in terms of color grading. The red color indicates an area with a negative charge, while the blue color represents an area with a positive charge. The MEP is used to understand the reactivity of the molecule, as well as to predict the behavior of electrons in the molecule.[62,63] MEP surfaces are obtained by B3LYP/6-311++G(d,p) level in the range of −0.06248, 0.06248 a.u, and the result is represented in Figure 4. It should be noted that the highest negatively charged area is located
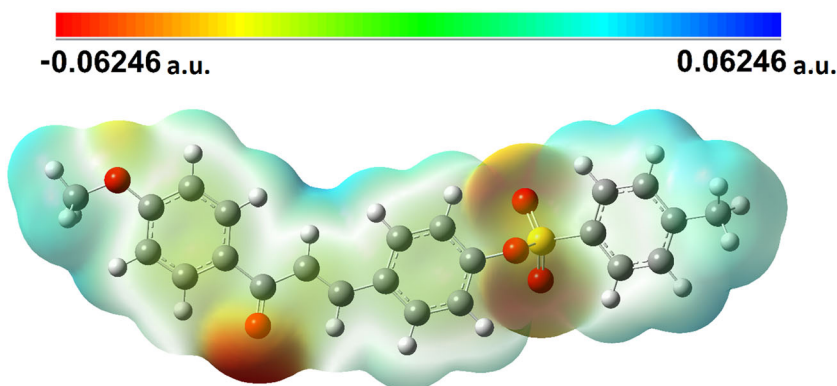
Figure 4. MEP surface for 4MPMS calculated by B3LYP/6-311++G(d,p).

Table 6. The static and frequency-dependent ($\lambda = 532\,nm$) α (esu), $\Delta\alpha$ (esu), β (esu), and γ (esu) for 4MPMS.

Parameter	4MPMS
μ	4.56088
μ[67]	6.20
$\alpha(0,0)$	5.3067×10^{-23}
$\alpha(0,0)$[67]	1.7×10^{-23}
$\Delta\alpha(0,0)$	5.5224×10^{-23}
$\alpha(-\omega,\omega)$	6.2319×10^{-23}
$\Delta\alpha(-\omega,\omega)$	7.7171×10^{-23}
$\beta(0;0,0)$	16.240×10^{-30}
$\beta(0;0,0)$[67]	9.2×10^{-30}
$\beta(-\omega;\omega,0)$	82.240×10^{-30}
$\beta(-2\omega;\omega,\omega)$	213.97×10^{-30}
$\gamma(0;0.0.0)$	213.77×10^{-36}
$\gamma(0;0,0,0)$[67]	15.5×10^{-36}
$\gamma(-\omega;\omega,0,0)$	943.74×10^{-36}
$\gamma(-2\omega;\omega,\omega,0)$	485.90×10^{-36}

in the $C=O$ group, and the second one is the SO_3 group. On the other hand, the highest positive charged area is located in the methyl group and C-CH_3 and O-CH_3 groups as well as the aromatic H atoms. So, if the 4MPMS molecule participates in any reaction, the sites most likely to interact are $C=O$ and SO_3 groups.

Nonlinear optical properties

Nonlinear optics is a phoneme of the interaction of intense light with matter. It is a relatively new field of research that has seen significant growth in recent years due to the potential of non-linear optical phenomena to be used in a wide range of applications, including high-speed tele-communications, all-optical signal processing, and biomedical imaging.[64,65] Currently, the nonlinear optical response of organic materials having electron donor and acceptor groups as well as the conjugated bridge that connects these groups is being heavily studied as they have faster response times and higher nonlinearities, due to the charge transfer and polarization effect.[66]

In theoretical NLO study, the static and frequency-dependent ($\lambda = 532\,nm$) values of nonlinear optical parameters such as polarizability ($<\alpha>$), the anisotropy of polarizability ($\Delta\alpha$), first-order hyperpolarizability (β) and second-order hyperpolarizability (γ) for 4MPMS are calculated using B3LYP/6-311++G(d,p) level and summarized in Table 6.

These parameters are calculated from the following equations;[68]

$$\mu = (\mu_x^2 + \mu_y^2 + \mu_z^2)^{1/2} \tag{1}$$

where the μ_x, μ_y, μ_z are dipole moments along the x, y, and z directions. This equation calculates the distribution of charge, the strength, and the chemical bond direction of the studied material.[69] The calculated μ for 4MPMS is found to be 4.56088 Debye, and it is found that the charge movement is dominant along the z direction. The obtained μ value is 3 times higher compared to that of Urea (1.527 Debye).[70] The polarizability equation is given by:

$$\alpha = \frac{1}{3}(\alpha_{xx} + \alpha_{yy} + \alpha_{zz}) \tag{2}$$

where the α_{xx}, α_{yy}, and α_{zz} are the polarizability tensor components. This equation displays the material's response under the magnetic field's effect. The α for the title molecule is found to be 5.3067×10^{-23} esu (static) and 6.2319×10^{-23} esu (dynamic). The $\Delta\alpha$ is equal to 5.5224×10^{-23} and 7.7171×10^{-23} in the static and dynamic ($w = 532$ nm) states respectively.

The coefficients of the dynamic first hyperpolarizability such as the electro-optic Pockel's effects (EOPE) with $\beta(-\omega, \omega, 0)$ and the second harmonic generation (SHG) with $\beta(-2\omega, \omega, \omega)$ of 4MPMS are calculated at the B3LYP/6-311++G(d,p) level of theory. From the results, it can be concluded that the first hyperpolarizability coefficients depend on the wavelength because the frequency-dependent first hyperpolarizability is largely increased.

The equation giving the first-order hyperpolarizability is expressed as the following:

$$\beta = (\beta_x^2 + \beta_y^2 + \beta_z^2)^{1/2} \tag{3}$$

$$\beta_a = Sum \ (\beta_{ajj} + \beta_{jaj} + \beta_{jja}) \tag{4}$$

It is a measure of the susceptibility of a material to an applied electric field. The $\beta(0,0,0)$, $\beta(-w,w,0)$, and $\beta(-2w,w,w)$ parameters for the title molecule are found to be 16.240×10^{-30}, $82.240x \times 10^{-30}$, 213.97×10^{-30} esu, respectively and as it is registered the $\beta(0,0,0)$ is 43 times greater than the Urea ($\beta(0,0,0)$ of urea is $0.3728 \times 10{-30}$ esu).[48]

The second-order hyperpolarizability (γ) is calculated via the following equation:

$$\gamma = \frac{1}{5}\left[(\gamma_{xxxx} + \gamma_{yyyy} + \gamma_{zzzz}) + 2(\gamma_{xxyy} + \gamma_{yyzz} + \gamma_{zzxx})\right] \tag{5}$$

where the γ_{xxxx}, γ_{yyyy}, γ_{zzzz}, γ_{xxyy}, γ_{yyzz}, and γ_{zzxx} are second-order hyperpolarizability tensors along x, y, and z direction. The $\gamma(0,0,0,0)$, $\gamma(-w,w,0,0)$, and $\gamma(-2w,w,w,0)$ parameters are calculated as 213.77×10^{-36}, 943.74×10^{-36} and 485.90×10^{-36} esu, respectively. In all these comparisons it is found that the NLO properties of the 4MPMS molecule, are very high compared to the Urea molecule, which leads us to state that the 4MPMS has good NLO properties regarding its promising results.

The computed values of first and second hyperpolarizability are high due to the molecule symmetry and delocalization of charge, specifically the movement of the π-electron cloud from the donor to the acceptor group.

These impressive results suggest that the title molecule 4MPMS possesses good NLO properties, making it a promising material for nonlinear optical devices.[44,71]

Thermodynamic properties

Regarding the many application fields of the title molecule, it is important to investigate the behavior of the 4MPMS at high temperatures. Online SHERMO application was used to calculate
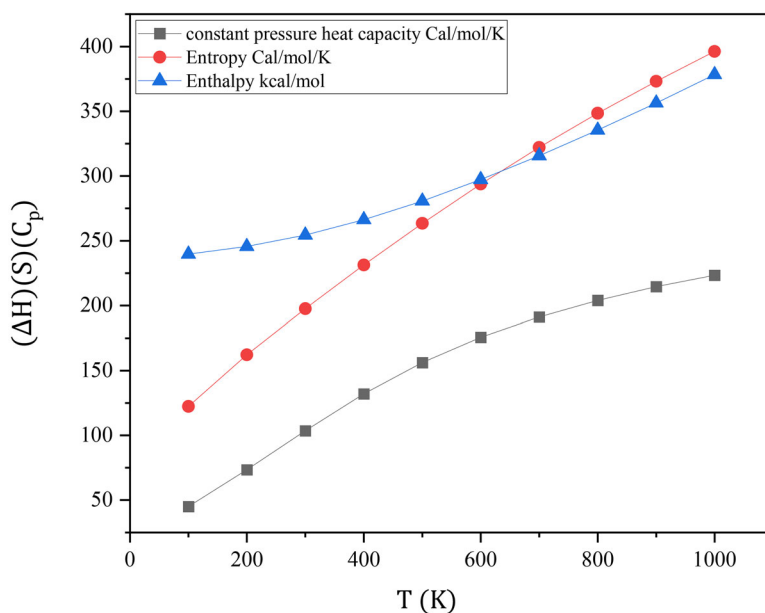
Figure 5. Thermodynamic properties of 4MPMS.

Table 7. Thermodynamic properties at different temperatures for the 4MPMS obtained by B3LYP/6-311++G(d,p) method.

Temperature K	C_p Cal mol^{-1} K^{-1}	S Cal mol^{-1} K^{-1}	ΔH Kcal mol^{-1}
100	45.064	122.324	239.709
200	73.439	162.137	245.615
298.150	103.023	196.956	254.270
300	103.578	197.595	254.461
400	132.06	231.378	266.273
500	156.143	263.524	280.724
600	175.595	293.777	297.346
700	191.254	322.063	315.716
800	204.019	348.463	335.501
900	214.58	373.121	356.447
1000	223.424	396.201	378.36

the thermodynamic properties of the title compound.[72] The online calculations for thermodynamic parameters are done under 1 atm pressure within the gas phase.

Among all the thermodynamic parameters Enthalpy(ΔH), Entropy (S), and the constant pressure heat capacity (C_p) are calculated as a function of temperature variation from 100 K to 1000 K with a 100 K step. The results are detailed in Figure 5 and Table 7. It is registered that these parameters are increasing with the temperature the as a result of the movement of electrons increasing with temperature which leads to an increase in atom vibration.[73]

Another calculation of total energy, zero-point energy **(ZPE)**, enthalpy **(ΔH)** entropy **(S)**, and constant pressure heat capacity (C_p) was carried out at room temperature 298.15 K and 1 atm pressure. The results are detailed in Table 8. The total energy represents the molecule energy and contains all the movements of the system rotational translational, vibrational, and electronic energy.

The total energy of the studied molecule is found to be -1663.081 a.u. and ZPE 236.695 kcal/mol. For other thermodynamic parameters, the vibrational partition represents the major contribution in the total energy of the system where, C_p, S, and (ΔH) registered 95.074 Cal mol^{-1} K^{-1}, 115.672 Cal mol^{-1} K^{-1}, and 251.9 Kcal mol^{-1} respectively on the other hand the

Table 8. The calculated thermodynamic parameters of 4MPMS.

Parameters	Calculation method
total energy (a.u.)	−1663.081003
Zero point energy (ZPE) kcal/mol	236.695
Rotational constants (GHz)	0.581037
	0.035246
	0.034107
Rotational temperatures (K)	0.027885
	0.001692
	0.001637
Entropy S (cal mol^{-1} K^{-1})	
total	196.956
Translational	43.91
Rotational	37.374
Vibrational	115.672
Enthalpy ΔH (kcal mol^{-1})	
total	254.27
Translational	1.481
Rotational	0.889
Vibrational	251.9
Specific heat capacity C$_p$ (cal mol^{-1} K^{-1})	
Total	103.023
Translational	4.968
Rotational	2.981

rotational represent the miniority with 37.374 Cal mol^{-1} K^{-1}, 12.981 Cal mol^{-1} K^{-1} and 0.889 Kcal mol^{-1} which signify the role of vibration in molecular systems.[73,74]

Conclusion

The optimized geometry, vibrational spectrum, ^{1}H and ^{13}C NMR spectra, frontier molecular orbital energies, molecular electrostatic potential surface as well as the static and frequency-dependent nonlinear optical properties of a chalcone derivative, 4-[(1E)-3-(4-methoxyphenyl)-3-oxoprop-1-en-1-yl]phenyl 4-methylbenzene-1-sulfonate (4MPMS) are calculated by using B3LYP/6-311++G(d,p) level. It is demonstrated that there is a general consistency between the obtained theoretical results and previously reported experimental data. The relatively small HOMO-LUMO energy gap indicated that the charge movement occurs in the 4MPMS molecule, inducing the nonlinear optical properties of the title molecule. The separation of positive and negative potential regions demonstrated with MEP surface also claimed the effective charge movements in 4MPMS. The frequency-dependent first-order and second-order hyperpolarizability for electro-optical Pockels effect $\beta(-\omega; \omega,0)$, the second harmonic generation $\beta(-2\omega; \omega, \omega)$, for the quadratic electro-optic Kerr effect, $\gamma(-\omega; \omega,0,0)$ and the electric field induced second-harmonic generation $\gamma(-2\omega; \omega, \omega,0)$ of the 4MPMS have been calculated to be 82.240×10^{-30}, 213.97×10^{-30}, 943.74×10^{-36} and 485.90×10^{-36} respectively using B3LYP/6-311++G(d,p). The frequency-dependent first and second-order hyperpolarizabilities (β and γ) are calculated as higher than those calculated for the absence of an additional electrical field. When both static and frequency-dependent NLO parameters are compared with those reported for a prototype NLO material pNA, it can be said that 4MPMS is a promising candidate for first and second-order NLO materials.

Disclosure statement

References

1. R. W. Boyd, A. L. Gaeta, and E. Giese . "Nonlinear Optics," In *Springer Handbook of Atomic, Molecular, and Optical Physics*, edited by Gordon W. F. Drake (Cham: Springer International Publishing, 2008), 1097–1110.

2. Z. Li, W. Zhang, and F. Xing, "Graphene Optical Biosensors," *International Journal of Molecular Sciences* 20, no. 10 (2019): 2461. doi:10.3390/ijms20102461

3. M. U. Khan, M. Ibrahim, M. Khalid, S. Jamil, A. A. Al-Saadi, and M. R. S. A. Janjua, "Quantum Chemical Designing of Indolo [3, 2, 1-jk] Carbazole-Based Dyes for Highly Efficient Nonlinear Optical Properties," *Chemical Physics Letters* 719 (2019): 59–66. doi:10.1016/j.cplett.2019.01.043

4. R. Kumar, T. Karthick, V Parol, P. Rawat, P. Tandon, A. Gupta, A. N. Prabhu, and V. Upadhyaya, "Spectroscopic Characterization and Structural Insights of 4-[(1E)-3-(4-Methoxyphenyl)-3-Oxoprop-1-en-1-yl] Phenyl 4-Methylbenzene-1-Sulfonate Using Vibrational, Electronic Spectra and Quantum Chemical Calculations," *Journal of Molecular Structure* 1225 (2021): 129144. doi:10.1016/j.molstruc.2020.129144

5. C. Zhuang, W. Zhang, C. Sheng, W. Zhang, C. Xing, and Z. Miao, "Chalcone: A Privileged Structure in Medicinal Chemistry," *Chemical Reviews* 117, no. 12 (2017): 7762–7810. doi:10.1021/acs.chemrev.7b00020

6. A. Aditya Prasad, K. Muthu, V. Meenatchi, M. Rajasekar, R. Agilandeshwari, K. Meena, J. Vijila Manonmoni, and S. P. Meenakshisundaram, "Optical, Vibrational, NBO, First-Order Molecular Hyperpolarizability and Hirshfeld Surface Analysis of a Nonlinear Optical Chalcone," *Spectrochimica Acta. Part A, Molecular and Biomolecular Spectroscopy* 140 (2015): 311–327. doi:10.1016/j.saa.2014.12.011

7. M. Kaur, and R. Kaushal, "Spectroscopic Investigations, ab-Initio DFT Calculations, Molecular Docking and in-Vitro Assay Studies of Novel Oxovanadium (V) chalcone Complexes as Potential Antidiabetic Agents," *Journal of Molecular Structure* 1271 (2023): 133994. doi:10.1016/j.molstruc.2022.133994

8. W. T. Eden, D. Alighiri, N. Wijayati, and S. Mursiti, "Synthesis of Chalcone Derivative from Clove Leaf Waste as a Natural Antioxidant," *Pharmaceutical Chemistry Journal* 55, no. 3 (2021): 269–274. doi:10.1007/s11094-021-02410-3

9. J. S. Dhaliwal, S. Moshawih, K. W. Goh, M. J. Loy, M. S. Hossain, A. Hermansyah, V. Kotra, N. Kifli, H. P. Goh, S. K. S. Dhaliwal, et al. "Pharmacotherapeutics Applications and Chemistry of Chalcone Derivatives," *Molecules* 27, no. 20 (2022): 7062. doi:10.3390/molecules27207062

10. Y. Ouyang, J. Li, X. Chen, X. Fu, S. Sun, and Q. Wu, "Chalcone Derivatives: Role in Anticancer Therapy," *Biomolecules* 11, no. 6 (2021): 894. doi:10.3390/biom11060894

11. L. W. Wijayanti, R. T. Swasono, W. Lee, and J. Jumina, "Synthesis and Evaluation of Chalcone Derivatives as Novel Sunscreen Agent," *Molecules* 26, no. 9 (2021): 2698. doi:10.3390/molecules26092698

12. Y. Yang, X. Wu, J. Jia, L. Shen, W. Zhou, J. Yang, and Y. Song, "Investigation of Ultrafast Optical Nonlinearities in Novel Bis-Chalcone Derivatives," *Optics & Laser Technology* 123 (2020): 105903. doi:10.1016/j.optlastec.2019.105903

13. J. C. Jebapriya, D. R. Jonathan, S. R. Maidur, P. Nallamuthu, P. S. Patil, and J. C. Prasana, "Crystal Structure, Synthesis, Growth and Characterization of a Non-Linear Chalcone Crystal:(2E)-1-(4-Chlorophenyl)-3-(4-Diethylaminophenyl)-Prop-2-en-1-One," *Journal of Molecular Structure* 1246 (2021): 131184. doi:10.1016/j.molstruc.2021.131184

14. Q. A. Wong, C. K. Quah, X. A. Wong, S. R. Maidur, H. C. Kwong, Y.-F. Win, P. S. Patil, and N. B. Gummagol, "Structure-Property Relationship of Three 2-Chloro-4-Fluoro Chalcone Derivatives: A Comprehensive Study on Linear and Non-Linear Optical Properties, Structural Characterizations and Density Functional Theory," *Journal of Molecular Structure* 1267 (2022): 133584. doi:10.1016/j.molstruc.2022.133584

15. A. H. Anizaim, S. Arshad, M. F. Zaini, M. Abdullah, D. A. Zainuri, and I. A. Razak, "Third Order Nonlinear Optical Properties of Selected Fluorinated Chalcone Derivatives," *Optical Materials* 98 (2019): 109406. doi:10.1016/j.optmat.2019.109406

16. P. Vennila, M. Govindaraju, G. Venkatesh, C. Kamal, Y. S. Mary, C. Y. Panicker, S. Kaya, S. Armaković, and S. J. Armaković, "A Complete Computational and Spectroscopic Study of 2-Bromo-1, 4-Dichlorobenzene–a Frequently Used Benzene Derivative," *Journal of Molecular Structure* 1151 (2018): 245–255. doi:10.1016/j.molstruc.2017.09.049

17. P. P. Vinaya, A. N. Prabhu, K. S. Bhat, and V. Upadhyaya, "Synthesis, Growth and Characterization of a Long-Chain π-Conjugation Based Methoxy Chalcone Derivative Single Crystal; a Third Order Nonlinear Optical Material for Optical Limiting Applications," *Optical Materials* 89 (2019): 419–429. doi:10.1016/j.optmat.2019.01.061

18. M. J. Frisch, G. W. Trucks, H. B. Schlegel, G. E. Scuseria, M. A. Robb, J. R. Cheeseman, G. Scalmani, V. Barone, G. A. Petersson, H. Nakatsuji, et al. Gaussian, Inc., Wallingford CT, 2016. Gaussian 16, revision C. 01.

19. A. D. Becke, "Density-Functional Thermochemistry. I. The Effect of the Exchange-Only Gradient Correction," *The Journal of Chemical Physics* 96, no. 3 (1992): 2155–2160. doi:10.1063/1.462066

20. C. Lee, W. Yang, and R. G. Parr, "Development of the Colle-Salvetti Correlation-Energy Formula into a Functional of the Electron Density," *Physical Review B* 37, no. 2 (1988): 785–789. doi:10.1103/PhysRevB.37.785

21. R. Dennington, T. A. Keith, and J. M. Millam, (2016). *GaussView, Version 6.0. 16.* (Shawnee, Kansas: Semichem Inc.).

22. A. Khireddine, M. Boukelkoul, Y. Atalay, Ö. Tamer, D. Avcı, L. Merzoud, and H. Chermette, "Structural, Electronic, Thermodynamic, Optical and Nonlinear Optical Properties of Curcumin Complexes with Transition Metals: DFT and TD-DFT Study," *ChemistrySelect* 7, no. 14 (2022): e202104442. doi:10.1002/slct.202104442

23. H. Chermette, "Density Functional Theory: A Powerful Tool for Theoretical Studies in Coordination," *Coordination Chemistry Reviews* 178-180 (1998): 699–721. doi:10.1016/S0010-8545(98)00179-9

24. S. I. Gorelsky, (2013). SWizard Program, University of Ottawa, Ottawa, Canada, 2010. There is no corresponding record for this reference.[Google Scholar].

25. P. A. Belaykov, and V. P. Ananikov, "Modeling of NMR Spectra and Signal Assignment Using Real-Time DFT/GIAO Calculations," *Russian Chemical Bulletin* 60, no. 5 (2011): 783–789. doi:10.1007/s11172-011-0125-8

26. F. Liu, D. M. Sanchez, H. J. Kulik, and T. J. Martínez, "Exploiting Graphical Processing Units to Enable Quantum Chemistry Calculation of Large Solvated Molecules with Conductor-like Polarizable Continuum Models," *International Journal of Quantum Chemistry* 119, no. 1 (2019): e25760. doi:10.1002/qua.25760

27. Z. Khanjari, B. Mohtat, R. Ghiasi, H. Djahaniani, and F. K. Behbahani, "Solvent and Temperature Effects on the Tautomerization of a Carbonitrile Molecule: A Conductor-like Polarizable Continuum Model (CPCM) Study," *Main Group Chemistry* 20, no. 1 (2021): 59–68. doi:10.3233/MGC-210016

28. N. Süleymanoğlu, R. Ustabaş, F. Eyduran, Ş. Direkel, Y. Ünver, and N. Kahriman, "2E)-3-(1-Benzothiophen-2-yl)-1-(4-Hydroxyphenyl) Prop-2-en-1-One: Synthesis, Characterization (IR, NMR and UV-Vis) DFT Study and Antimicrobial Activity," *Journal of the Chemical Society of Pakistan* 43, no. 6, (2021): 712–725.

29. V. Parol, A. N. Prabhu, M. A. Taher, S. R. G. Naraharisetty, N. K. Lokanath, and V. Upadhyaya, "A Third-Order Nonlinear Optical Single Crystal of 3, 4-Dimethoxy-Substituted Chalcone Derivative with High Laser Damage Threshold Value: A Potential Material for Optical Power Limiting," *Journal of Materials Science: Materials in Electronics* 31 (2020): 9133–9150.

30. H.-K. Fun, P. S. Patil, S. R. Jebas, and S. M. Dharmaprakash, "("E)-3-(2-Chlorophenyl)-1-(2-Furyl) Prop-2-en-1-One," *Acta Crystallographica. Section E, Structure Reports Online* 64, no. Pt 8 (2008): O 1467. doi:10.1107/S1600536808020965

31. F. Basha, F. L. A. Khan, S. Muthu, and M. Raja, "Computational Evaluation on Molecular Structure (Monomer, Dimer), RDG, ELF, Electronic (HOMO-LUMO, MEP) Properties, and Spectroscopic Profiling of 8-Quinolinesulfonamide with Molecular Docking Studies," *Computational and Theoretical Chemistry* 1198 (2021): 113169.

32. U. H. Patel, S. A. Gandhi, V. M. Barot, and M. C. Patel, "3-(2-Chloro-3-Hydroxy-4-Methoxyphenyl)-1-(4, 5-Dimethoxy-2-Methylphenyl) Prop-2-en-1-One," *Acta Crystallographica. Section E, Structure Reports Online* 68, no. Pt 10 (2012): o2926–o2927. doi:10.1107/S1600536812038275

33. V. V. Aswathy, Y. Sheena Mary, P. J. Jojo, C. Y. Panicker, A. Bielenica, St, Armaković, S. J. Armaković, P. Brzózka, S. Krukowski, and C. Van Alsenoy, "Investigation of Spectroscopic, Reactive, Transport and Docking Properties of 1-(3, 4-Dichlorophenyl)-3-[3-(Trifluoromethyl) Phenyl] Thiourea (ANF-6): Combined Experimental and Computational Study," *Journal of Molecular Structure* 1134 (2017): 668–680. doi:10.1016/j.molstruc.2017.01.016

34. Y. Li, Y. Liu, H. Wang, X. Xiong, P. Wei, and F. Li, "Synthesis, Crystal Structure, Vibration Spectral, and DFT Studies of 4-Aminoantipyrine and Its Derivatives," *Molecules* 18, no. 1 (2013): 877–893. doi:10.3390/molecules18010877

35. S. B. Radder, R. Melavanki, U. Radder, S. M. Hiremath, R. Kusanur, and S. S. Khemalapure, "Synthesis, Spectroscopic (FT-IR, FT-Raman, NMR), Reactivity (ELF, LOL and Fukui) and Docking Studies on 3-(2-Hydroxy-3-Methoxy-Phenyl)-1-(3-Nitro-Phenyl)-Propenone by Experimental and DFT Methods," *Journal of Molecular Structure* 1255 (2022): 132443. doi:10.1016/j.molstruc.2022.132443

36. Ö. Tamer, D. Avcı, and Y. Atalay, "Quantum Chemical Characterization of N-(2-Hydroxybenzylidene) Acetohydrazide (HBAH): a Detailed Vibrational and NLO Analysis," *Spectrochimica Acta. Part A, Molecular and Biomolecular Spectroscopy* 117 (2014): 78–86. doi:10.1016/j.saa.2013.07.112

37. G. Socrates, (2004). Infrared and Raman Characteristic Group Frequencies: Tables and Charts. *Colloid Polym Sci* 283 (2004): 235.

38. H. Suwito, K. U. Haq, N. N. D. Rahmah, A. N. Kristanti, and N. N. T. Puspaningsih, "4-({4-[(2 E)-3-(2, 5-Dimethoxyphenyl) Prop-2-Enoyl] Phenyl} Amino)-4-Oxobutanoic Acid," *Molbank* 2017, no. 2 (2017): M938. doi:10.3390/M938

39. J. S. P. P. Leela, R. Hemamalini, S. Muthu, and A. A. Al-Saadi, "Spectroscopic Investigation (FTIR Spectrum), NBO, HOMO–LUMO Energies, NLO and Thermodynamic Properties of 8-Methyl-N-Vanillyl-6-Nonenamideby DFT Methods," *Spectrochimica Acta. Part A, Molecular and Biomolecular Spectroscopy* 146 (2015): 177–186. doi:10.1016/j.saa.2015.03.027

40. R. S. Saji, J. C. Prasana, S. Muthu, J. George, T. K. Kuruvilla, and B. R. Raajaraman, "Spectroscopic and Quantum Computational Study on Naproxen Sodium," *Spectrochimica Acta. Part A, Molecular and Biomolecular Spectroscopy* 226 (2020): 117614. doi:10.1016/j.saa.2019.117614

41. C. Arunagiri, M. Arivazhagan, A. Subashini, and N. Maruthaiveeran, "Theoretical and Experimental Calculations, Mulliken Charges and Thermodynamic Properties of 4-Chloro-2-Nitroanisole," *Spectrochimica Acta. Part A, Molecular and Biomolecular Spectroscopy* 131 (2014): 647–656. doi:10.1016/j.saa.2014.03.116

42. J. George, J. C. Prasana, S. Muthu, T. K. Kuruvilla, S. Sevanthi, and R. S. Saji, "Spectroscopic (FT-IR, FT Raman) and Quantum Mechanical Study on N-(2, 6-Dimethylphenyl)-2-{4-[2-Hydroxy-3-(2-Methoxyphenoxy) Propyl] Piperazin-1-yl} Acetamide," *Journal of Molecular Structure* 1171 (2018): 268–278. doi:10.1016/j.molstruc.2018.05.106

43. A. Esme, "Quantum Chemical Calculations on the Geometrical, Conformational, Spectroscopic (FTIR, FT-Raman) Analysis and NLO Activity of Milrinone [5-Cyano-2-Methyl-(3, 4'-Bipyridin)-6 (1h)-One] by Using Hartree-Fock and Density Functional Methods," *Indian Journal of Pure & Applied Physics (IJPAP)* 55, no. 7 (2017): 478–489.

44. S. Muthu, and G. Ramachandran, "Spectroscopic Studies (FTIR, FT-Raman and UV–Visible), Normal Coordinate Analysis, NBO Analysis, First Order Hyper Polarizability, HOMO and LUMO Analysis of (1R)-N-(Prop-2-yn-1-yl)-2, 3-Dihydro-1H-Inden-1-Amine Molecule by ab Initio HF and Density Functional Methods," *Spectrochimica Acta. Part A, Molecular and Biomolecular Spectroscopy* 121 (2014): 394–403. doi: 10.1016/j.saa.2013.10.093

45. M. Arivazhagan, and S. S. P. Kamala, Vibrational Spectroscopic Studies, NMR and NBO Calculations of 3-Hydroxy BenzylidyneTrifluoride (2013).

46. S. Muthu, J. C. Prasana, C. S. Abraham, and M. Raja, "Spectroscopic (FT-IR, FT-Raman) Investigation, Topology (ESP, ELF, LOL) Analyses, Charge Transfer Excitation and Molecular Docking (Dengue, HCV) Studies on Ribavirin," *Chemical Data Collections* 17 (2018): 236–250.

47. R. N. S. Santiago, P. T. C. Freire, A. M. R. Teixeira, P. N. Bandeira, H. S. Santos, T. L. Lemos, and C. A. N. Ferraz, "FT-Raman and FT-IR Spectra and DFT Calculations of Chalcone (2E)-1-(4-Aminophenyl)-3-Phenyl-Prop-2-en-1-One," *Vibrational Spectroscopy* 97 (2018): 1–7. doi:10.1016/j.vibspec.2018.04.007

48. P. Jayaprakash, P. Sangeetha, M. P. Mohamed, G. Vinitha, S. Muthu, M. Prakash, and M. L. Caroline, "Growth and Characterization of DL-Mandelic Acid (C6H5CH (OH) CO2H) Single Crystal for Third-Order Nonlinear Optical Applications," *Journal of Molecular Structure* 1148 (2017): 314–321. doi:10.1016/j.molstruc.2017.07.049

49. P. Manjusha, J. C. Prasana, S. Muthu, and B. F. Rizwana, "Spectroscopic Elucidation (FT-IR, FT-Raman and UV-Visible) with NBO, NLO, ELF, LOL, Drug Likeness and Molecular Docking Analysis on 1-(2-Ethylsulfonylethyl)-2-Methyl-5-Nitro-Imidazole: An Antiprotozoal Agent," *Computational Biology and Chemistry* 88 (2020): 107330. doi:10.1016/j.compbiolchem.2020.107330

50. S. Muthu, and J. U. Maheswari, "Quantum Mechanical Study and Spectroscopic (FT-IR, FT-Raman, 13C, 1H, UV) Study, First Order Hyperpolarizability, NBO Analysis, HOMO and LUMO Analysis of 4-[(4-Aminobenzene) Sulfonyl] Aniline by ab Initio HF and Density Functional Method," *Spectrochimica Acta Part A: Molecular and Biomolecular Spectroscopy* 92 (2012): 154–163. doi:10.1016/j.saa.2012.02.056

51. K. Jagannathan, S. Kalainathan, and G. Bhagavannarayana, "Growth and Characterization of Organic Non-Linear Optical Crystal 4-Hydoroxy benzaldehyde-N-Methyl 4-Stilbazolium Tosylate (HBST)," *Spectrochimica Acta. Part A, Molecular and Biomolecular Spectroscopy* 73, no. 1 (2009): 79–83. doi:10.1016/j.saa.2009.01.025

52. Ö. Tamer, M. Şimşek, D. Avcı, and Y. Atalay, "Static/Dynamic First and Second Order Hyperpolarizabilities, Optimized Structures, IR, UV–Vis, 1H and 13C NMR Spectra for Effective Charge Transfer Compounds: A DFT Study," *Spectrochimica Acta. Part A, Molecular and Biomolecular Spectroscopy* 286 (2023): 122005. doi: 10.1016/j.saa.2022.122005

53. A. Ramalingam, A. R. Guerroudj, S. Sambandam, A Kumar, R. Krishnamoorthy, N. Boukabcha, A. Chouaih, and M. Elayaperumal, "Synthesis, Vibrational Spectra, Hirshfeld Surface Analysis, DFT Calculations, and in Silico ADMET Study of 3-(2-Chloroethyl)-2, 6-Bis (4-Fluorophenyl) Piperidin-4-One: A Potent anti-Alzheimer Agent," *Journal of Molecular Structure* 1269 (2022): 133845. doi:10.1016/j.molstruc.2022.133845

54. M. H. Jamroz, (2004). Vibrational energy distribution analysis VEDA 4.

55. A. Pekparlak, Ö. Tamer, S. D. Kanmazalp, N. Berber, M. Arslan, D. Avcı, N. Dege, E. Tarcan, and Y. Atalay, "Synthesis, Crystal Structure, Spectroscopic (FT-IR, 1H and 13C NMR) and Nonlinear Optical Properties of a Novel Potential HIV-1 Protease Inhibitor," *Chemical Physics Letters* 742 (2020): 137171. doi: 10.1016/j.cplett.2020.137171

56. F. E. Inscore, S. Z. Knottenbelt, N. D. Rubie, H. K. Joshi, M. L. Kirk, and J. H. Enemark, "Understanding the Origin of Metal − Sulfur Vibrations in an Oxo-Molybdenum Dithiolene Complex: Relevance to Sulfite Oxidase," *Inorganic Chemistry* 45, no. 3 (2006): 967–976. doi:10.1016/j.saa.2012.02.056

57. S. Nithyanandan, and P. Kannan, "Photo Switchable Pendant Furyl and Thienyl Fulgimides Containing Polypyrroles," *Polymer Degradation and Stability* 98, no. 11 (2013): 2224–2231. doi:10.1016/j.polymdegrad-stab.2013.08.020

58. G. Gece, "The Use of Quantum Chemical Methods in Corrosion Inhibitor Studies," *Corrosion Science* 50, no. 11 (2008): 2981–2992. doi:10.1016/j.corsci.2008.08.043

59. Z. Zhou, and R. G. Parr, "Activation Hardness: New Index for Describing the Orientation of Electrophilic Aromatic Substitution," *Journal of the American Chemical Society* 112, no. 15 (1990): 5720–5724. doi:10.1021/ja00171a007

60. S. Altürk, D. Avcı, Ö. Tamer, and Y. Atalay, "1H–Pyrazole–3–Carboxylic Acid: Experimental and Computational Study," *Journal of Molecular Structure* 1164 (2018): 28–36. doi:10.1016/j.molstruc.2018.03.032

61. N. Khelloul, K. Toubal, N. Boukabcha, N. Dege, Ahmed Djafri, Nour El Houda Belkafouf, Nadia Benhalima, Ayada Djafri, Abdelkader Chouaih, and Yusuf Atalay, "2-thioxo-3N-(2-Ethoxyphenyl)-5 [4′-Methyl-3′ N-(2′-Ethoxyphenyl) Thiazol-2′(3′ H)-Ylidene] Thiazolidin-4-One: Growth, Spectroscopic Behavior, Single-Crystal Investigation, Hirshfeld Surface Analysis, DFT/TD-DFT Computational Studies and NLO Evaluation," *Phosphorus, Sulfur, and Silicon and the Related Elements* 198, no. 3 (2023): 199–214. doi:10.1080/10426507.2022.2134373

62. J. A. Pople, and D. L. Beveridge, "The Electrostatic Potential and Its Application to Molecular Structure," *Advances in Chemical Physics* 15 (1969): 1–57.

63. K. R. Liedl, and P. J. Hore, "The Molecular Electrostatic Potential and Its Applications," *Annual Review of Physical Chemistry* 64, no. 1 (2013): 703–726.

64. RW. Boyd, *Nonlinear Optics*. (New York: Academic press, 2020).

65. Ch Bosshard, . *Organic Nonlinear Optical Materials*. (London: CRC press, 2020).

66. K Fukui, "Role of Frontier Orbitals in Chemical Reactions," *Science* 218, no. 4574 (1982): 747–754. doi:10.1126/science.218.4574.747

67. L. T. Cheng, W. Tam, S. H. Stevenson, G. R. Meredith, G. Rikken, and S. R. Marder, "Experimental Investigations of Organic Molecular Nonlinear Optical Polarizabilities. 1. Methods and Results on Benzene and Stilbene Derivatives," *The Journal of Physical Chemistry* 95, no. 26 (1991): 10631–10643. doi:10.1021/j100179a026

68. TWG. Solomons, and CB. Fryhle, *Organic Chemistry* (Hoboken, NJ: John Wiley & Sons, 2008).

69. G. F. Jasmine, M. Amalanathan, and S. D. D. Roy, "Molecular Structure and Charge Transfer Contributions to Nonlinear Optical Property of 2-Methyl-4-Nitroaniline: A DFT Study," *Journal of Molecular Structure* 1112 (2016): 63–70. doi:10.1016/j.molstruc.2016.02.013

70. M. Faizan, M. Mehkoom, Z. Afroz, V. H. N. Rodrigues, S. M. Afzal, and S. Ahmad, "Experimental and Computational Investigation of Novel Dihydrated Organic Single Crystal of 2, 4, 6-Triaminopyrimidine and 3, 5-Dintrobenzoic Acid: Linear and Nonlinear Optical Response with Limiting Performance," *Journal of Solid State Chemistry* 300 (2021): 122255. doi:10.1016/j.jssc.2021.122255

71. S. Armaković, S. J. Armaković, J. P. Šetrajčić, and V. Holodkov, "Aromaticity, Response, and Nonlinear Optical Properties of Sumanene Modified with Boron and Nitrogen Atoms," *Journal of Molecular Modeling* 20, no. 12 (2014): 2538. doi:10.1007/s00894-014-2538-4

72. T. Lu, and Q. Chen, "Shermo: A General Code for Calculating Molecular Thermochemistry Properties," *Computational and Theoretical Chemistry* 1200 (2021): 113249. doi:10.1016/j.comptc.2021.113249

73. M. Suhasini, E. Sailatha, S. Gunasekaran, and G. R. Ramkumaar, "Vibrational and Electronic Investigations, Thermodynamic Parameters, HOMO and LUMO Analysis on Lornoxicam by Density Functional Theory," *Journal of Molecular Structure* 1100 (2015): 116–128. doi:10.1016/j.molstruc.2015.07.003

74. S. Kaya, H. Gökce, T. Arslan, and G. Alpaslan, "Synthesis, Spectroscopic Characterization, DFT Computations, Nonlinear Optical Profile and Molecular Docking Study of a Novel Chalcone Derivative," *Journal of Molecular Structure* 1202 (2020): 127270. doi:10.1016/j.molstruc.2019.127270